

**CHARACTERIZATION OF POST-YIELD BEHAVIOR OF A WARSHIP
GRILLAGE SUBJECT TO REPEATED IMPACTS**

by

©Lt(N) Matthew Lee Robbins, BA, B.Eng.

A thesis submitted to the
School of Graduate Studies
in partial fulfillment of the requirements
for the degree of

Master of Engineering

Department of Ocean & Naval Architectural Engineering
Faculty of Engineering & Applied Science
Memorial University of Newfoundland

October 2020

St. John's

Newfoundland & Labrador

Canada

Abstract

This thesis investigates the progressive accumulation of plastic strain in the response of a uniaxially-stiffened warship grillage repeatedly impacted by a smooth, rigid, spherical indenter. An explicit, nonlinear numerical model was developed, and five distinct indentation patterns were applied over an ultra-low cycle frequency range (<50 impacts) across a range of impact velocities to characterize the grillage response. The results were analyzed to assess whether a ship structure exhibits shakedown behaviors associated with small strain plasticity and fatigue behaviors, or whether sufficient evidence exists to suggest considerations for progressive plastic accumulation (ratcheting) be made when assessing damage capacity in ship structural analysis. Impact experimentation was conducted at full-scale using a double-pendulum style impact apparatus to validate the numerical model. The experimental observations show fair agreement with the numerical simulations. It was found that at increasing levels of impact energy, the grillage response transitioned from elastic shakedown to pseudo-shakedown or ratcheting responses.

Acknowledgments

The research presented hereafter was not a sole effort. It was only made possible through the extraordinary contributions and support of a select few people and organizations. I would like to express my deepest thanks and appreciation to the following:

Dr. Bruce Quinton, Assistant Professor—my graduate supervisor, for his unending patience, enthusiasm, and consistently excellent direction and advice. For several years you have been in my corner, and I would not have begun, nor completed this undertaking without your unparalleled support.

Cmdre Christopher Earl, Cdr Robyn Locke, and LCdr Paul Collier, who passionately championed for me to attend Memorial to undertake this research program.

Mr. Matt Curtis, a MUN technologist, for his expertise and willingness to share his knowledge and great sense of humor throughout a challenging experimental test program.

The Royal Canadian Navy (RCN) and Canadian Armed Forces (CAF) who provided the opportunity and financial resources necessary for me to attend the program, as well as Defence Research & Development Canada (DRDC), VARD Marine Inc., and the American Bureau of Shipping (ABS) for their keen interest in the research material, and the financial support that helped make this project possible.

It would be remiss of me not to also thank Dr. Claude Daley, for many enlightening conversations (enlightening for me, probably less so for him) and his helpful counsel.

I would also like to acknowledge Dr. Ahmed Elruby and fellow graduate students, Mr. Andrew Greenham, and Mr. Jordan Norman. These gentlemen were most excellent friends and colleagues as we traversed the research landscape. Many of my most salient discussion points arose from our protracted discussions about the experimental program.

Mr. Adam Lewis, Mr. Alexander Dawe, Mr. Patrick Eveleigh, and Dr. Jillian Kaulbach—who have never wavered in their encouragement.

My deep and sincere gratitude to my family, Barbara, Keith, and Nicholas, for their continuous help and support. I am forever indebted to you for helping me follow the opportunities and experiences that brought me to this point.

Lastly, my spouse, Kirsten—who has patiently supported and defended me at every step along the way, enthusiastically listened to far too many research arguments and tolerated years of my eccentricity as I pored (and continue to pore) through mountains of engineering research. This thesis would not be possible without you. Thank you for everything.

Table of Contents

Abstract	ii
Acknowledgments.....	iii
Table of Contents	iv
List of Tables	x
List of Figures	xi
List of Appendices	xvii
Nomenclature and Abbreviations	xviii
Chapter 1 INTRODUCTION.....	1
1.1 Introduction	1
1.2 Problem Definition.....	3
1.2.1 Study Significance.....	5
1.3 Scope and Objectives	6
1.4 Research presentation and limitations.....	8
1.5 Beneficiaries.....	9
1.5.1 IROQUOIS Class	9
1.6 Research propositions	11
1.6.1 Experimental hypothesis.....	12
Chapter 2 LITERATURE REVIEW.....	14

2.1 Introduction	14
2.2 Structure and deformation in isotropic, ductile materials	15
2.3 Plasticity modeling.....	15
2.3.1 Yield condition	16
2.3.2 Hardening rules.....	23
2.3.3 Flow rule.....	26
2.4 Deformation models.....	27
2.4.1 Elastic deformation models	28
2.4.2 Inelastic (Plastic) deformation models	29
2.5 Creep deformation models	37
2.6 3-Dimensional stress states	38
2.7 Cyclic loading and unloading.....	39
2.8 Stress-strain summary	40
2.9 Overview of ratcheting mechanism and phenomena	41
2.9.1 Introduction to ratcheting	41
2.9.2 Defining ratcheting	43
2.9.3 Delineating between ratcheting behavior and other fatigue behaviors.....	45
2.9.4 Factors affecting ratcheting	50
2.10 Gravity-based impact & indentation theory	51

2.10.1 Impact testing rationale	52
2.10.2 Energy and impact force relationships	52
2.10.3 Common variations on impact tests.....	53
2.10.4 Application of linear pendulum theory to nonlinear pendulums	57
2.11 State of the current literature	58
2.11.1 Ratcheting.....	59
2.11.2 Response of stiffened plates to repeated impacts	61
2.12 Research questions arising from literature review	62
Chapter 3 EXPERIMENTAL METHODOLOGY	65
3.1 Introduction	65
3.2 Large pendulum apparatus	65
3.3 Grillage model.....	68
3.3.1 Structural components	70
3.4 Boundary conditions	71
3.5 Rigid indenter	74
3.6 Instrumentation.....	75
3.6.1 Faro System	76
3.6.2 Calibration	78
3.7 Loading scenario	78

3.8 Experimental procedure	80
3.9 Results	82
3.9.1 First impact	85
3.9.2 Second impact.....	86
3.9.3 Third impact	87
3.9.4 Fourth impact.....	90
3.9.5 Subsequent impacts	93
3.10 Material Tensile Tests	98
3.10.1 Tensile Specimen Specifications	99
3.10.2 Instrumentation and apparatus.....	100
3.10.3 Results	101
3.11 Numerical model	105
3.11.1 Methodology.....	106
3.11.2 Structural model	107
3.11.3 Finite element mesh definition	109
3.11.4 Element selection.....	110
3.11.5 Element formulation	112
3.11.6 Element thickness	114
3.11.7 Model mesh	115

3.11.8 Load scenario.....	119
3.11.9 Material model.....	130
3.11.10 Utilizing uniaxial tensile test data for numerical simulation.....	133
3.11.11 Boundary conditions.....	133
3.11.12 Contact.....	136
3.11.13 Damping	137
3.11.14 Time steps for explicit simulations.....	138
3.11.15 Numerical model validation	139
Chapter 4 EXPERIMENTAL AND NUMERICAL FINDINGS	148
4.1 Experimental observations	149
4.1.1 Experimental stress-strain data.....	149
4.1.2 Strain accumulation	150
4.1.3 Load case 1	150
4.1.4 Load case 2	154
4.1.5 Load case 3	159
4.1.6 Load case 4	162
4.1.7 Load case 5	166
Chapter 5 DISCUSSION AND ANALYSIS	172
5.1 Individual load case analysis.....	172

5.1.1 Load case 1	172
5.1.2 Load case 2	173
5.1.3 Load case 3	175
5.1.4 Load case 4	177
5.1.5 Load case 5	180
5.2 Similarities across load cases (performance trends)	182
5.3 Experimental uncertainties	184
5.3.1 Physical experimental uncertainties	185
5.3.2 Numerical experimental uncertainties	191
Chapter 6 CONCLUSION	197
6.1 Summary of Findings	197
6.2 Conclusions	198
6.3 Acceptance or refutation of hypothesis	199
6.4 Implications for research	200
6.5 Limitations	201
6.6 Recommendations and future work	202
References	205
Appendix A – Material test report	215

List of Tables

Table 3-1. Resultant contact velocities from pendulum arm inclination angles	81
Table 3-2. Impact number (N) versus resultant experimental deflection (d) [cm]	82
Table 3-3. Material coupon dimensions.....	99
Table 3-4. Material properties for uniaxial tensile test coupon #1	102
Table 3-5. Material properties for uniaxial tensile test coupon #2	103
Table 3-6. Material properties for uniaxial tensile test coupon #3	104
Table 3-7. Material property summary for uniaxial tensile test coupons	105
Table 3-8. Model mesh quality assessment	116
Table 3-9. Mesh convergence details.....	119
Table 3-10. Material model parameters for grillage structure	132
Table 3-11. Numerical model deflection resulting from a range of material models.....	142
Table 4-1. Material summary for true stress and true strain data derived from uniaxial..	149

List of Figures

Figure 1-1. HMCS IROQUOIS post-TRUMP.....	11
Figure 2-1. Bi-axial yield surface	16
Figure 2-2. Multi-axial yield surface	17
Figure 2-3. Representative stress-strain diagram depicting engineering and true stress-..	18
Figure 2-4. Illustration of monotonic strain described as a function of stress	19
Figure 2-5. Multi-axial yield stress surface (Tresca criteria).....	20
Figure 2-6. Multi-axial yield stress surface (von Mises criteria).....	21
Figure 2-7. Multi-axial yield stress surface (Drucker-Prager criteria)	22
Figure 2-8. Bauschinger effect describes early yield on the opposing stress axis as a.....	23
Figure 2-9. Kinematic and isotropic hardening models' unloading behavior	25
Figure 2-10. True stress-strain curves in tension at room temperature for various metals	28
Figure 2-11. Elastic-perfectly plastic rheological model.....	29
Figure 2-12. Elastic-perfectly plastic material model (graphical representation).....	30
Figure 2-13. Elastic, linear-hardening material model (graphical representation)	32
Figure 2-14. Elastic, linear-hardening rheological model	32
Figure 2-15. Elastic, multi-linear hardening rheological model	33
Figure 2-16. Elastic, multi-linear hardening material model (graphical representation)..	34
Figure 2-17. Ramberg-Osgood relationship	36
Figure 2-18. Strain-time history for cyclic loading: unloading remains elastic (left)	39
Figure 2-19. Corresponding stress-strain hysteresis plots for Figure 2-18.....	39

Figure 2-20. Open hysteresis behavior illustrating ratcheting mechanism.....	43
Figure 2-21. Stress-time plot illustrating conditions for ratcheting.....	43
Figure 2-22. A selected taxonomy of loading behaviors	45
Figure 2-23. Nominal cycle frequency ranges	46
Figure 2-24. Hysteresis loops illustrating low cycle fatigue (symmetric stress cycling) .	47
Figure 2-25. Stress-time plot illustrating conditions for symmetric stress cycling	47
Figure 2-26. Strain-time plot illustrating asymmetric strain cycling (mean stress	48
Figure 2-27. Hysteresis loops illustrating asymmetric strain cycling (mean stress.....	48
Figure 2-28. Elastic shakedown.....	49
Figure 2-29. Plastic shakedown (alternating plasticity).....	50
Figure 2-30. A simple gravity pendulum.....	54
Figure 3-1. Schematic of the dual-pendulum impact apparatus	65
Figure 3-2. Photograph depicting a partial view of the dual-pendulum apparatus with...	66
Figure 3-3. Experimental test grillage as fabricated	68
Figure 3-4. CAD grillage model as designed for numerical experimentation.....	68
Figure 3-5. HMCS IROQUOIS Tee-stiffener design (left) versus test grillage built-Tee..	70
Figure 3-6. Plate and stiffener boundary configuration	71
Figure 3-7. Boundary condition installation in a pendulum frame	72
Figure 3-8. Ring frame panel restraint (left) depicts the method of restricting degrees of	73
Figure 3-9. Spherical, rigid indenter in its mounted configuration.....	74

Figure 3-10. FARO arm coordinate management representative level of detail. Note the	76
Figure 3-11. A composite image displays the Faro arm scanning process surface profile.	77
Figure 3-12. Pendulum arms raised to 50° and primed for experimental impact	80
Figure 3-13. Grillage pre-impact depicting a mostly planar surface	82
Figure 3-14. Profile view of FARO scans showing the qualitative scale of progressive .	83
Figure 3-15. Normal view of FARO scans showing the qualitative scale of progressive	83
Figure 3-16. Impact crater post-impact #1	85
Figure 3-17. Impact crater post-impact #2.....	86
Figure 3-18. An alternative view post-impact #3 illustrating impact depth	88
Figure 3-19. Impact crater post-impact #3 (left) with shadow indenter pattern indicated	89
Figure 3-20. Grillage deflection post-impact #4. Circled regions denote a change in the	90
Figure 3-21. Plate inner side depicting the evolution of the impact crater between.....	91
Figure 3-22. Profile view depicting stiffener plasticity effects post-impact #4.....	92
Figure 3-23. Panel condition post-impact #7	94
Figure 3-24. Corresponding galling material adhered to indenter surface (left) and.....	95
Figure 3-25. Galling on bulk plate material (left) and magnified view of galled section..	96
Figure 3-26. Boundary condition plasticity. Note the bowing/wave developed in the.....	97

Figure 3-27. Tensile test coupons	99
Figure 3-28. Instron 5585-H tensile test apparatus	100
Figure 3-29. Externally-mounted extensometer	101
Figure 3-30. Stress-strain plot for uniaxial tensile test coupon #1	102
Figure 3-31. Stress-strain plot for uniaxial tensile test coupon #2	103
Figure 3-32. Stress-strain plot for uniaxial tensile test coupon #3	104
Figure 3-33. Grillage model geometry depicting surface areas	107
Figure 3-34. Grillage model geometry depicting design curves	108
Figure 3-35. Indenter model geometry	108
Figure 3-36. A stiffened panel structure meshed with quadrilateral elements	109
Figure 3-37. 4-node shell element geometry	110
Figure 3-38. 8-node solid (brick) element geometry	111
Figure 3-39. Quadrilateral mesh of a stiffened panel structure	115
Figure 3-40. Smooth, spherical rigid indenter mesh	115
Figure 3-41. Mesh convergence analysis indicating convergence at 15 mm	117
Figure 3-42. Side-by-side mesh density comparison	118
Figure 3-43. Load case #1: Co-incident indenter strike	121
Figure 3-44. Load case #1: Impact pattern	122
Figure 3-45. Load case #2: Clock-pattern strike	123
Figure 3-46. Load case #2: Impact pattern	123
Figure 3-47. Load case #3: Expanded centralized damage area	124
Figure 3-48. Load case #3: Impact pattern	125

Figure 3-49. Load case #4: Wave pattern	126
Figure 3-50. Load case #4: Impact pattern	126
Figure 3-51. Load case #5: Expanded damage area--variation #1.....	127
Figure 3-52. Load case #5: Impact pattern	128
Figure 3-53. Load case impact pattern summary.....	129
Figure 3-54. Plasticity curve for a MAT_024 multi-linear plasticity model of a mild steel	132
Figure 3-55. Constrained nodal rigid bodies (cyan markers) used to model the grillage	134
Figure 3-56. An enlarged view of the nodal rigid body markers (cyan) to model grillage	135
Figure 3-57. Experimental boundary condition placement.....	135
Figure 3-58. Deflection versus number of impacts for a rigid, smooth, spherical indenter	143
Figure 3-59. Profile comparison of the experimental FARO scans versus the simulated	147
Figure 4-1. True stress-strain data for experimental panel specimen	149
Figure 4-2. Load case #1: Effective plastic strain versus impact number	151
Figure 4-3. Load case #1: Accumulated damage pattern (following 50 impacts or at ...	152
Figure 4-4. Load case #1: Accumulated damage pattern (following 50 impacts or at ...	153
Figure 4-5. Load case #2: Effective plastic strain versus impact number	154
Figure 4-6. Load case #2: Accumulated damage pattern (following 50 impacts or at ...	156

Figure 4-7. Load case #2: Accumulated damage pattern (following 50 impacts or at ...	157
Figure 4-8. Load case #3: Effective plastic strain versus impact number	159
Figure 4-9. Load case #3: Accumulated damage pattern (following 50 impacts or at ...	160
Figure 4-10. Load case #3: Accumulated damage pattern (following 50 impacts or at .	161
Figure 4-11. Load case #4: Effective plastic strain versus impact number	162
Figure 4-12. Load case #4: Accumulated damage pattern (following 50 impacts or at .	164
Figure 4-13. Load case #4: Accumulated damage pattern (following 50 impacts or at .	165
Figure 4-14. Load case #5: Effective plastic strain versus impact number	166
Figure 4-15. Load case #5: Accumulated damage pattern (following 50 impacts or at .	168
Figure 4-16. Load case #5: Accumulated damage pattern (following 50 impacts or at .	170
Figure 5-1. Numerical versus experimental indentation pattern after five impacts.....	173
Figure 5-2. Grillage deformation leading to a pseudo-shakedown state (left); plasticity.	177
Figure 5-3. Increased stiffener plasticity following a pseudo-shakedown state	178
Figure 5-4. Load case #4 rupture located at the plate-stiffener connection.....	179
Figure 5-5. Load case #5 rupture located at both plate-stiffener connections	181

List of Appendices

Appendix A – Material test report	215
---	-----

Nomenclature and Abbreviations

1-D	One-dimensional
2-D	Two-dimensional
3-D	Three-dimensional
ABS	American Bureau of Shipping
ASTM	American Society for Testing & Materials
BT	Belytschko-Tsay Element
CMM	Coordinate Measuring Machine
DOF	Degree of Freedom
DRDC	Defence Research & Development Canada
FE	Finite Element
FEA	Finite Element Analysis
FEM	Finite Element Method
HL	Hughes-Liu Element

HMCS	Her Majesty's Canadian Ship
MAT#	Material Formulation
NATO	North Atlantic Treaty Organization
NLFEA	Non-linear Finite Element Analysis
NLKH	Non-linear Kinematic Hardening
TRUMP	TRIBAL-Class Update & Modernization Period
RCN	Royal Canadian Navy
SAE	Society of American Engineers
SOTA	State-of-the-art
UTS	Ultimate Tensile Strength

Chapter 1 INTRODUCTION

1.1 Introduction

Navies around the globe are staring down a proverbial barrel, increasingly being tasked to operate, as Canadian Prime Minister Justin Trudeau quipped in 2015, “with more teeth and less tail” (The Canadian Press, 2015). The competing constraints of budget reductions and steadily rising costs posed against ever-widening mission demands have created a condition in which fewer warships are being replaced at the end of their service lives. These same warships are being asked to operate in environments that represent a departure from their original design intent and for extended intervals between maintenance cycles. As these demands create increased pressure on Navies, one of the avenues of operation with heightened scrutiny is the increased use of ships previously designated low- and non-ice class designs for use in ice-infested waters. The expansion of ships’ design intent is not a surprising development. Arctic traffic patterns show that there has been a progressively growing application of these vessel types over the past four decades.

Given the unprecedented rates of ice dissolution, international interest in the development and exploitation of untapped natural resources and more direct North American transit routes via the Northern Sea Route and Northwest Passage will continue to generate a need for increasingly unique Naval mission demands. Power projection needs ranging from sovereignty and defensive duties through to anti-piracy and coastal safety will continue to dominate the defense posture in the North. As a result, the inevitable demand for increased marine support will lead to longer operational cycles with less time

for maintenance and a reduced budget and appetite for any repairs construed as not operationally imperative.

The increase in missions in non-traditional operating environments may require an equally non-traditional application of engineering thinking. Engineers and designers are asked to define the performance characteristics of materials and designs when exposed to ice environments—and amplify our understanding of the consequences of violating these definitions. One of the aspects of design poised to be most affected is how a ship’s failure criteria are conferred. Traditional design was dominated by yield-stress designs (Paik & Thayamballi, 2009; Quinton, 2008). However, engineers and ship classification societies are recognizing the untapped value of the plastic reserve inherent in structures. Subsequently, designs are beginning to consider using ultimate limit states to maximize a material’s lifetime potential while optimizing the structure for other constraining factors such as weight or cost (Paik et al., 2003; Quinton, 2008). Many behaviors associated with plastic deformation are still under development. While the theory of elasticity is relatively robust and has been well-developed analytically, the realm of plasticity continues to show active research and development (Barkey, 2018). As the problem space continues to be defined, questions remain regarding how materials, such as steel, respond to accumulated deformation and repeated multi-axial loads. At present, one of the leading resources for exploring the problem space is the numerical simulation of problem types using the Finite Element Method (FEM).

The research presented herein comprises a thesis sub-divided into six chapters. The introductory chapter places the research into context by defining the problem and

describing the significance of the study. It also outlines the scope and study objectives placing the research in context as a sub-study within a broader research program. Chapter 2 describes the literature review for this thesis, christening the current landscape of the research map of stiffened panel response under repeated impacts. Moreover, Chapter 2 outlines the fundamental tenets of plasticity and orients all further discussion of accumulated plastic deformation by defining a standard working definition on which to base the discussion. The chapter concludes by reviewing gravity-based impact and indentation theory to introduce the concepts on which the full-scale grillage impact experiment was built. Chapter 3 introduces a numerical model for the simulation of repeated impact accumulated damage scenarios, as well as, the full-scale laboratory grillage experiments used to validate the numerical model. Chapter 4 presents observations from the experimental tests and details the findings of several impact scenarios applied to the numerical model. Chapter 5 discusses the impact scenarios from Chapter 4 and examines sources of error and model adaptations that might improve fidelity. Chapter 6 summarizes the findings of this research, presents the conclusions of this thesis, and identifies recommendations for future work.

1.2 Problem Definition

While it is well-accepted that a ship's structural fatigue strength is critically important to its long-term viability and safety, this initial acceptance fails to qualify the issue's significance sufficiently. Researchers have demonstrated that numerous ship hull fractures and ruptures are attributable to a combination of low cycle fatigue and accumulated plastic deformation (Hu & Chen, 1995). As early as 1965, investigators

debated the role of accumulated plastic deformation (ratcheting) as a detriment to ship structure (Murray, 1965), and by 1990 the experimental evidence suggested the ratcheting influence was significant enough to necessitate inclusion in a ship's inelastic damage calculations (Mansour et al., 1990). However, despite these early studies, there remains a paucity of literature regarding the nature of fundamental ship structures' response(s) to repeated impacts. The gap in the literature is exacerbated by the fact that repeated impacts are either not, or only marginally, addressed by current design rules (Zhu et al., 2018). Paik (2018) has rightly suggested that neglecting accumulated inelastic deformation is unrealistic with a ship's lifetime structural behavior. By inspection, an aged ship straight out of re-fit shows the scars of a lifetime at sea. Even a new ship, once floated, presents evidence of locked-in stress releases, micro-structural cracks, and small deflections in plate and stiffener material instantiated during construction.

The link between ratcheting and reduced specimen or component life has been established experimentally, but debate exists about its relevance to full-scale ship structures. Much of this uncertainty comes from the fact that most of these experimental observations have been conducted parochially on small-scale, or component-level specimens under highly constrained loads. In other words, the problem space is still in its infancy regarding the exploration of its boundaries. From a naval engineering perspective, one of the critical territories to be illuminated within this landscape can be postulated as follows:

Is an accumulation of incremental inelastic deformation experienced as a mode of non-performance in a warship grillage exposed to coincident, unsymmetrical cyclic impact loads? Alternatively, this may be phrased as follows: will exposing a grillage structure to a repeating load such that a non-zero mean stress, which at

some point in its cycle history is in excess of that required for initial yielding, develop and lead to continued incremental plasticity?

1.2.1 Study Significance

There are myriad real-world instances and cases of ships or other ocean and marine structures subjected to repeated impacts ranging from hydrodynamic and hydrostatic phenomena such as wave-induced slamming behavior and cyclic tank pressure loads to collisions, allisions, and other accidental loads. Any of these behaviors may lead to severe structural damage as these loads accumulate (Zhu et al., 2018). Accumulated plastic deformation may severely impact a ship's life. Combined with the fact that marine vehicle operators continue to presume small obstacles may only present a minor risk of dents, or will simply "work harden the hull," the perceptions in concert with the actual realities of the costs and risk of accumulated damage may create a severe hazard to a ship's lifespan and capacity to resist plastic flow.

The research undertaken in this study seeks to ascertain whether the resultant behavior of a ship grillage under repeated impact warrants inclusion in life estimations or is indicative that there is indeed a need for revision to current design rules to reflect the contribution of accumulated damage to a ship's structural health. Moreover, the study seeks to confirm (or dispel) some common beliefs about the nature of repeated impacts and how they exacerbate or relieve the stress developed in a strike location based on the propagation of the impact site. In summary, the study examines the veracity of some long-held beliefs of the hull surveying and ship design community regarding the relative risks or benefits of foregoing immediate repair when a section of ship structure is inelastically strained.

1.3 Scope and Objectives

Despite an uptick in the pulse of research veins pertaining to repeated impact experimentation and accumulated damage research over the last two decades (Paul, 2019), there is a widely-acknowledged open area for experimental research concerning post-yield plastic responses of structures under cyclic (repeated) 3D stress states. Hübel (1996) articulates that more experimentation is required to understand real-life plasticity phenomena. Furthermore, numerous researchers (Dong et al., 2019; Quinton et al., 2016; Ringsberg et al., 2018; Sun & Zhang, 2015) propose that simplified inelastic analysis is a fundamental evaluation method to validate numerical approximations of behavior while simultaneously advocating that the development of appropriate simulation capacity will contribute to the fidelity and veracity of detailed inelastic analysis efforts. A necessary first step to build a research foundation for advanced analytical descriptions of complex post-yield structural response is the simplified characterization of behavior under 3-dimensional loads.

This thesis investigates the structural response of a representative design of a stiffened warship grillage concerning its response to accumulated plasticity due to repeated impacts. The investigation is completed through the creation of an explicit non-linear numerical model that is validated against full-scale experiments using a fabricated steel grillage structure that is nominally consistent with the grillage structure employed by Canada's IROQUOIS-class destroyers. Once validated, several load scenarios were imposed on the numerical model. These load scenarios are an effort to address contemporaneous issues being considered as traditionally low- and non-ice class vessels

are increasingly used in operational environments that may see them subjected to repeated impact loads from wave and ice interactions. Chief among these questions: is the structure capable of withstanding accumulated damage due to a load? Over what range of impact speeds does the structure respond inelastically? How does repeated coincident damage accumulate in the structure? How does this damage compare when similar load applications are applied across a span of the domain? What are the structural failure mechanisms associated with accumulated damage? Are there characteristic behaviors observable such as elastic shakedown, plastic shakedown, progressive plastic accumulation, or instantaneous plastic collapse? Finally, is it possible to identify what impact energy/collision impact velocities are associated with the different structural responses?

Five accumulated plastic damage scenarios were investigated within the confines of a known limit for ultra-low cycle behavior (50 cycles/50 impacts):

1. a coincident repeating impact centralized between two transverse stiffeners;
2. repeating impacts translationally varied across the horizontal and vertical axis of the impact plane at a distance of a one-half radius of the indenter dimension;
3. repeating impacts translationally varied across the horizontal and vertical axis of the impact plane originating at center-span of one inner transverse stiffener and progressing one-half indenter radius horizontally and vertically with each impact until a second inner transverse stiffener is reached;

4. repeating impacts along a wave-like (sinusoidal) pattern originating center-span of one inner transverse stiffener and progressing horizontally across the panel to a second inner stiffener before applying the inverse pattern; and,
5. applying a repeating impact pattern originating at center-span of one inner transverse stiffener and proceeding horizontally to a second inner transverse stiffener (simulating a cyclic load with a sliding action, e.g., scraping off a jetty point).

The simplified characterization of the structural response of repeated multi-axial loads in 3-D space is a necessary first step to more complex multi-source stress analyses (Hübel, 1996). It is intended that this research and the experimentation and numerical development provide benchmark efforts from which further academic study may springboard. Thus, this thesis seeks to provide preliminary answers to the questions identified above to focus on both development and criticism regarding how best to characterize grillage structure response to repeated impacts.

1.4 Research presentation and limitations

The results of this research are presented in a variety of forms, including graphical representations of strain accumulation-impact cycle relationships, force-displacement curves, and rhetoric commenting on structural failure observations. Accumulated plasticity is, by its nature, cyclic and dynamic processes that progress by intervals, which have an associated rate. However, the plastic accumulated damage scenarios presented here were modeled without strain-rate effects or kinematic friction effects given that at the time of

experimentation, the research team did not have access to resources to permit the evaluation of and validation of such effects.

1.5 Beneficiaries

The outcomes of this research benefit myriad personnel, including:

- Designers addressing hull life estimates, damage capacity, and structural hull response;
- Senior Naval staff engaged in generating Design Intent and Concept of Employment for a given hull form;
- Industry partners involved in the design, re-fit, assessment, and repair of vessels;
- Classification societies seeking to amplify codification of behavior beyond the simple elastic-plastic regimes, or blanket applications of IACS which may be less suitable for low- and non-ice-class vessels; and,
- Research engineers and academics developing plasticity understanding at the component and structural level in 3D.

1.5.1 IROQUOIS Class

The research conducted in this investigation uses a built-for-purpose grillage that was based on the structural design of a mid-ship section of the Royal Canadian Navy's (RCN) IROQUOIS-class destroyers, specifically HMCS IROQUOIS. Also known as the Tribal-class, and officially designated the DDH 280 series, IROQUOIS was a guided-missile destroyer initially launched in the 1970s, undergoing a significant programme upgrade—the Tribal class update and modernization programme (TRUMP) in 1991. The post-TRUMP vessel featured displacement changes due to main propulsion machinery and

weapon & sensor system updates, as well as a significant overhaul to the weatherdeck and superstructure. The modernized vessel is shown in Figure 1-1. The class is notable due to its extended surface life (more than 40 years) among North Atlantic Treaty Organization (NATO) warships. This extended service life exposed IROQUOIS to a multitude of different operational roles in a diverse set of wave conditions, including the Adriatic, Arabian, and Caribbean seas, as well as, the Atlantic and Indian oceans.

The longevity of the hull presents enormous potential for research derived from various aspects of the hull's behavior over the course of its lifetime. As a non-ice class vessel constructed from steel similar to standard commercial shipbuilding steel CS G40.21 260 WT, the ship's service history may provide an atlas of indicative behaviors mirrored in similar builds throughout both NATO and commercial ships now being asked to sail in extended operational windows surpassing their initial intended lifespan. Consequently, characterizing a range of behaviors of similar builds with steels of mixed-media, e.g., new, fatigued, aged, a combination of new-aged, etc. is an essential first step in producing a robust plot of predictive structural behavior under a range of adverse conditions.



Figure 1-1. HMCS IROQUOIS post-TRUMP

1.6 Research propositions

The propositions of this research connect the idea that there exist underlying mechanisms when a structure is exposed to repeated damage that are markedly different from the material behavior when a component or structure is subjected to a single incidence of impact. Consequently, damage accumulation may present with any number of different behaviors depending on the load history or may respond in a highly-regularized manner consistent with structural definitions already codified in structural literature. Structural behavior is well-understood at the specimen level throughout the elastic limit, and even into rudimentary plasticity. However, when considering component and structural level effects, a limit-state approach and understanding of the resultant holistic structural

behaviors of these components at these limits cannot be well-articulated without first robustly testing and challenging previously held beliefs regarding structural response.

1.6.1 Experimental hypothesis

Beliefs in these propositions have been commonly accepted and are only recently being aggressively challenged through the added capabilities for testing provided by numerical simulation. Subsequently, these propositions can be assessed in a scientific context by framing the research conducted throughout this investigation with the three cascading components of an assumption, a thesis, and a hypothesis.

1.6.1.1 Assumption

It was assumed that ship structures exposed to repeated impacts of constant energy (or less) exhibit work hardening behaviors throughout their impact region.

1.6.1.2 Thesis

From this assumption, it was posited that as a structure experiences work-hardening conditions, the ability of the structure to withstand repeated impacts improves as the degree of plasticity (in the plastic range) strain hardens the material and increases the elasticity response of the region of interest.

1.6.1.3 Null hypothesis

As a result of the assumptions and thesis, the following hypothesis was proposed:

When a region of interest within a ship structure is exposed to repeated, cyclic impacts, the structure will exhibit a shakedown response.

1.6.1.4 Alternate hypothesis

The associated alternate hypothesis theorizes:

When a region of interest within a ship structure is exposed to repeated, cyclic impacts, a non-shakedown response will characterize the structure's performance.

Chapter 2 LITERATURE REVIEW

2.1 Introduction

A variety of concepts and engineering frameworks underpins investigations concerning the structural capacity of ship structures. Some of the necessary theory includes fundamental concepts of infinitesimal stress-strain theory and its expansion to more advanced three-dimensional behaviors governed by theories of elasticity and plasticity. The relationship between monotonic experimental data and cyclic loading patterns governs the interpretation of repeated impact patterns and phenomena observable in experiments regarding accumulated plastic deformation. Moreover, laboratory experiments were conducted using a large double pendulum apparatus governed by well-established energy conservation models and indentation/impact testing principles. Innumerable researchers have conducted a range of investigation that has advanced each of these realms separately, while a considerable body of research is growing to define how these various bodies of knowledge can be used to identify the behavior of structures exposed to repeated impact. However, this field of study is still largely in its infancy, and many concurrent directions of research are being pursued.

This chapter introduces a broad overview of essential theory contributing to the accumulated plastic deformation research discussed in later chapters. Furthermore, it reviews extant branches of repeated impact theory as applied to ship structures, as well as, the broad scope of ratcheting literature. In so doing, it was possible to expose gaps in the literature, determine essential phenomenon and factors to account for in experimentation, and articulate many suitable research questions, as identified in section 1.3, to address.

2.2 Structure and deformation in isotropic, ductile materials

Isotropic, ductile materials such as steel are subject to three primary modes of deformation, which can be sub-categorized as elastic, plastic, and creep deformation (Dowling, 2007). Advanced experimental, analytical, or numerical analysis of the behavior associated with a specimen under some type of load-displacement scenario necessitates constitutive equations describing the stress-strain behavior underpinning the specimen's mechanical behavior. Many of these constitutive relationships have been well-developed for relatively simple components such as beams, shells, and primitive solids (Chen & Han, 1988). These same equations can be applied using finite element (FE) techniques to discern results for more complex three-dimensional applications given a more complex geometry or multi-axial load scenario (Wu & Gu, 2012). Regardless of the complexity or scenario developed, governing mechanical behaviors represented with stress-strain relationships undergird the engineering.

2.3 Plasticity modeling

Briefly, plasticity modeling is a solid mechanics theory used to describe the plastic behavior of materials. Plasticity theories are broadly explained using variants of three basic elements, a yield condition, a flow rule, and a hardening rule. Depending on the behaviors observed and investigated, alternative descriptions exist for each of these elements to best fit the observed material behavior. The selection of a set of conditions is vital to framing the context and applicability of an analytical or numerical model's capability to explain experimental behavior.

2.3.1 Yield condition

Flow plasticity theories assume that the total strain in a body can be decomposed additively into an elastic part and a plastic portion. The elastic portion of the strain can be determined using a yield condition determined by a linear elastic constitutive model. The yield condition is a mathematical description identifying which combination of stresses will cause a material to yield (Chen & Han, 1988).

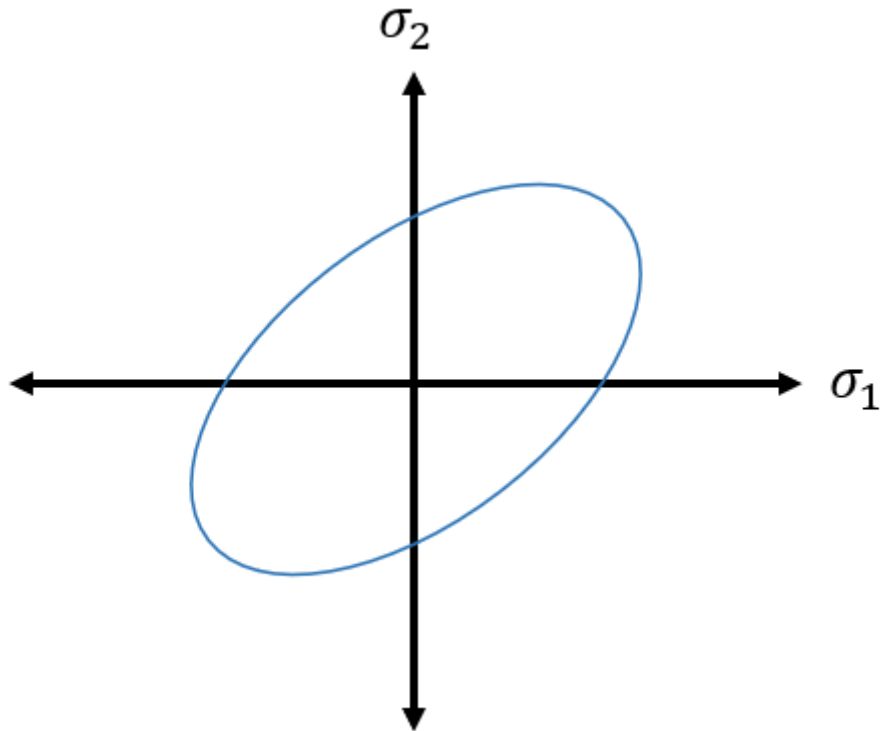


Figure 2-1. Bi-axial yield surface

$$f(\sigma) = k \quad [1]$$

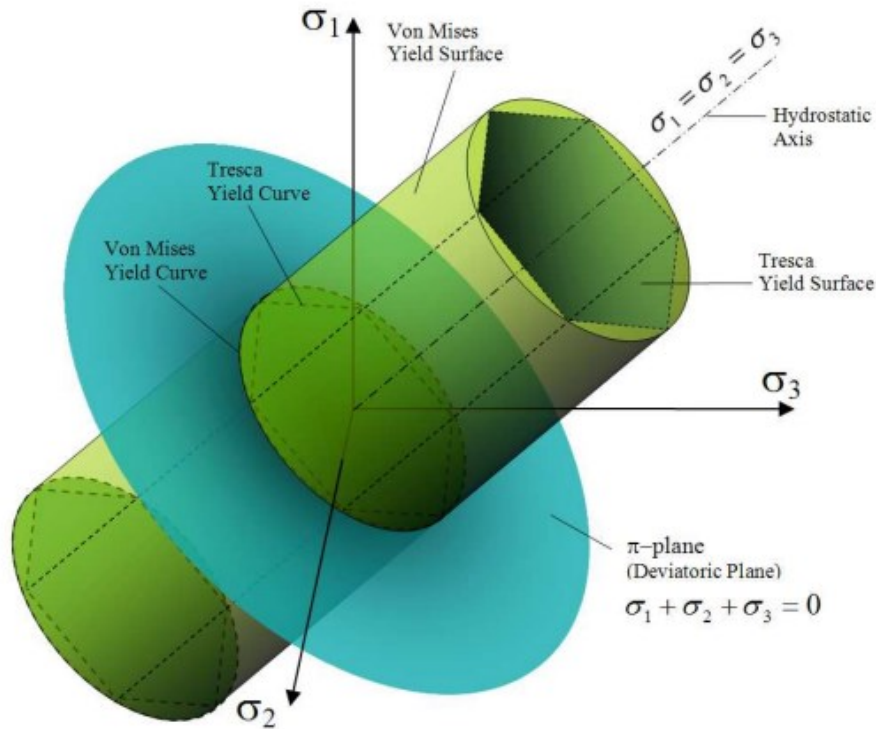


Figure 2-2. Multi-axial yield surface¹

In an investigation, such as the axially-loaded stress-strain coupon, the yield criteria are simply defined as the normal stress and corresponding strain observed in testing. As the stress-strain relationship becomes bi-axial, the yield condition can be described as a 2-dimensional surface enclosing a locus of yield points that can be represented by Figure 2-1 or mathematically described by equation (1) (Lubliner & Moran, 1992). In states of multi-axial loading, the surface is described by a 3-dimensional surface (representatively illustrated in Figure 2-2), which assumes numerous characteristic shapes depending on the yield condition being applied (Johnson, 1989).

¹ Adapted from https://en.wikipedia.org/wiki/Yield_surface

2.3.1.1 Monotonically loaded stress-strain curves

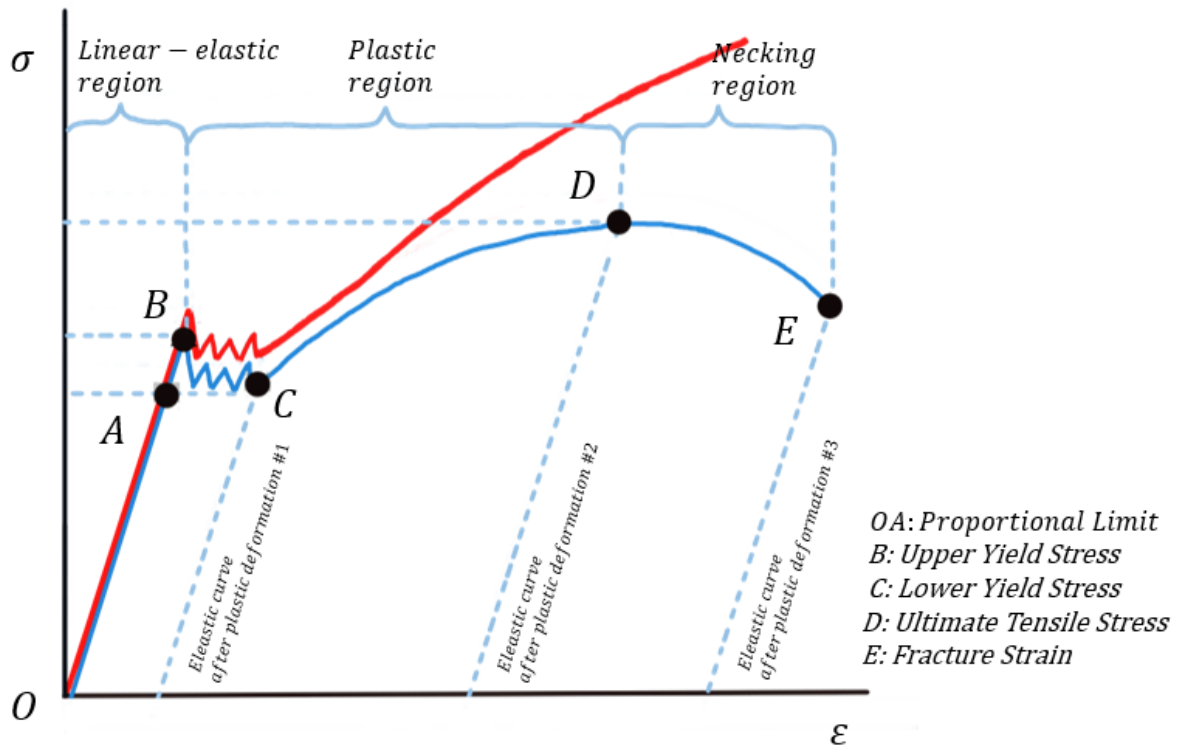


Figure 2-3. Representative stress-strain diagram depicting engineering and true stress-strain curves

An established origin or baseline reference point characterizes the post-yield deformation behavior of mild steel to describe the material in reference to a stress-strain curve under monotonic loading (Dowling, 2007). Graphically, the nominal curve describing an isotropic, ductile material, and its salient reference features is depicted in Figure 2-3 (Hibbeler, 2001). The use of such an origin facilitates finite element analysis of components comprised of a material that can be defined by these descriptions, as they are represented mathematically by a constitutive equation relating strain as a function of stress as illustrated by Figure 2-4 and described by Equation 2.

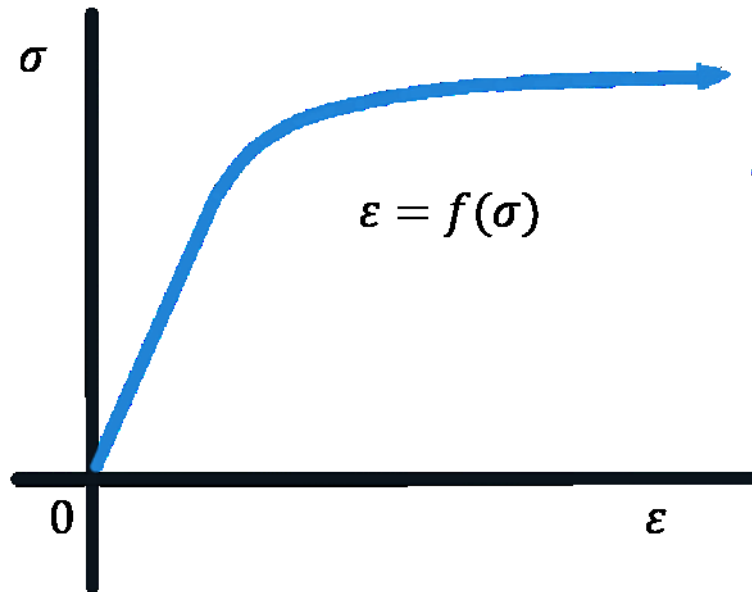


Figure 2-4. Illustration of monotonic strain described as a function of stress

$$\epsilon = f(\sigma)$$

[2]

2.3.1.2 Tresca-Guest

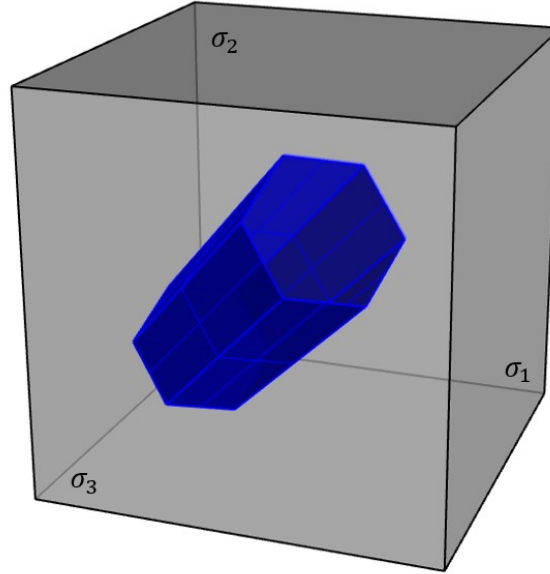


Figure 2-5. Multi-axial yield stress surface (Tresca criteria)

$$\tau_{max} = \tau_y \quad [3]$$

$$\text{where: } \tau_{max} = \frac{\sigma_{max} - \sigma_{min}}{2} \quad [4]$$

The Tresca criterion (Maximum Shear Stress criterion), presented in Figure 2-5, identifies the onset of yield when the maximum shear stress in the material, τ_{max} equals the maximum shear stress at yielding in the uniaxial tension test τ_y according to equations (3) and (4), respectively.

2.3.1.3 von Mises

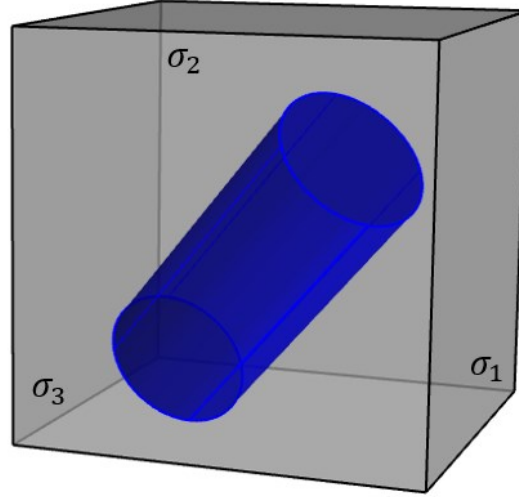


Figure 2-6. Multi-axial yield stress surface (von Mises criteria)

$$\tau_{max} = \tau_y = \tau_{h0} ; \text{at yielding} \quad [5]$$

$$\frac{1}{\sqrt{2}} \sqrt{(\sigma_{xx} - \sigma_{yy})^2 + (\sigma_{yy} - \sigma_{zz})^2 + (\sigma_{zz} - \sigma_{xx})^2 + 6(\tau_{xy}^2 + \tau_{yz}^2 + \tau_{zx}^2)} = \sigma_y \quad [6]$$

The von Mises criterion (Maximum Distortion/Shear Energy criterion), presented in Figure 2-6, identifies the onset of yield when the shear stress on an octahedral plane exceeds the value necessary to cause yielding. The resulting condition can be expressed according to equation (5) such that the failure criteria can substitute a uniaxial stress state into the octahedral criterion to provide effective stress taking the form given in equation (6).

2.3.1.4 Drucker-Prager

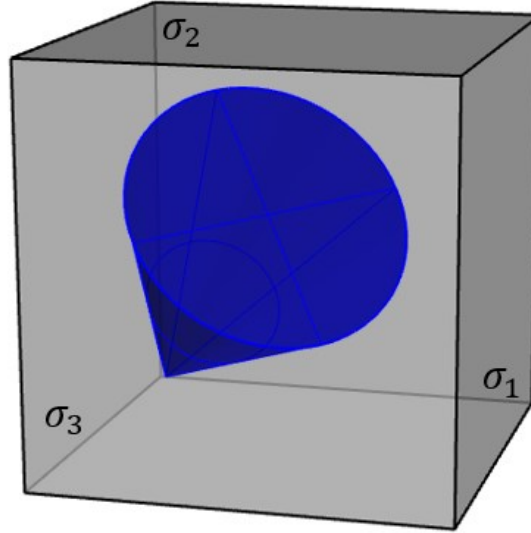


Figure 2-7. Multi-axial yield stress surface (Drucker-Prager criteria)

$$\left(\frac{m-1}{2}\right)(\sigma_1 + \sigma_2 + \sigma_3) + \left(\frac{m+1}{2}\right)\sqrt{\frac{(\sigma_1 - \sigma_2)^2 + (\sigma_2 - \sigma_3)^2 + (\sigma_3 - \sigma_1)^2}{2}} = S_{yc} \quad [7]$$

$$\text{with: } m = \frac{S_{yc}}{S_{yt}} \text{ such that [7] reduces to [6] when } S_{yc} = S_{yt} \quad [8]$$

The Drucker-Prager yield criterion, presented in Figure 2-7, is a modification of the von Mises criterion. In this modification, the yield surface remains circular but introduces a change of radius depending on the degree of deviatoric stress. The inclusion of a hydrostatic-dependent invariant allows the yield criteria to vary depending on whether a material has failed or undergone plastic yielding under tensile or compressive forces. The criterion is expressed by equation (7) and reduces to the von Mises variant of equation (6) when the material has equivalent values in tension and compression, as described by equation (8).

2.3.2 Hardening rules

The hardening rule describes the evolution of a yield surface, and other associated internal variables, with plastic strain through a functional relationship as described by equation (9). The two most common governing models repeatedly used in the literature in concert with the other plasticity elements differ in their treatment of the yield surface as a growth surface, or a translational surface, depending on their inclusion of the experimentally-observed Bauschinger effect (Lubliner & Moran, 1992).

$$f(\sigma) = k(\varepsilon^p) \quad [9]$$

2.3.2.1 Bauschinger effect

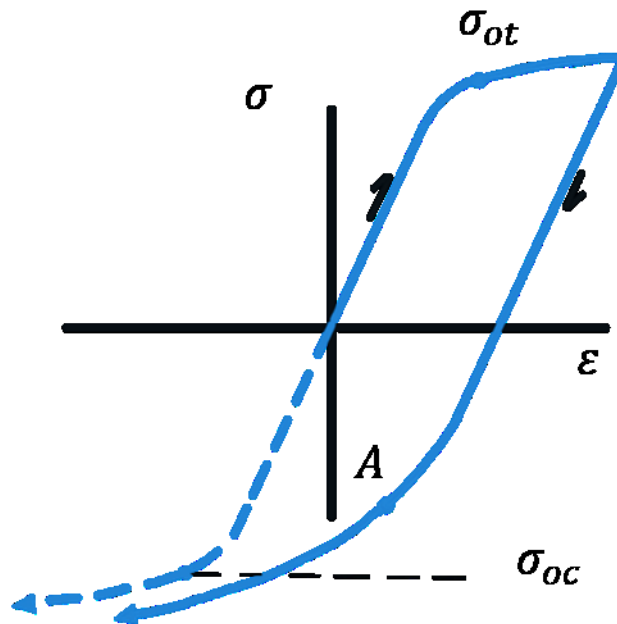


Figure 2-8. Bauschinger effect describes early yield on the opposing stress axis as a result of yield surface growth

When the direction of stress is reversed after yielding has occurred, the stress-strain loading path will no longer coincide with the monotonic path. Such a behavior is observable whether the stimulus is a removal of the impetus force, or a complete reversal of stress such as in a perfectly cyclic loading condition. Instead, as depicted in Figure 2-8, an early yielding is observable as compared with the monotonic compression path as well as in subsequent loads, which put the specimen back into a tension state. This so-named Bauschinger effect is not merely a theoretical construct, but has been observed in many real-world materials (Chen & Han, 1988; Frederick & Armstrong, 2007). Consistent with these observations, when a material is subjected to severe cyclic loads, the stress-strain path and subsequent yield point become shorter with each half-cycle. The added complexity of this behavior necessitates the selection of an appropriate mathematical model rigorous enough to capture such trends to predict behavior in components subjected to successive severe loads (Frederick & Armstrong, 2007).

2.3.2.2 Kinematic and isotropic hardening behavior

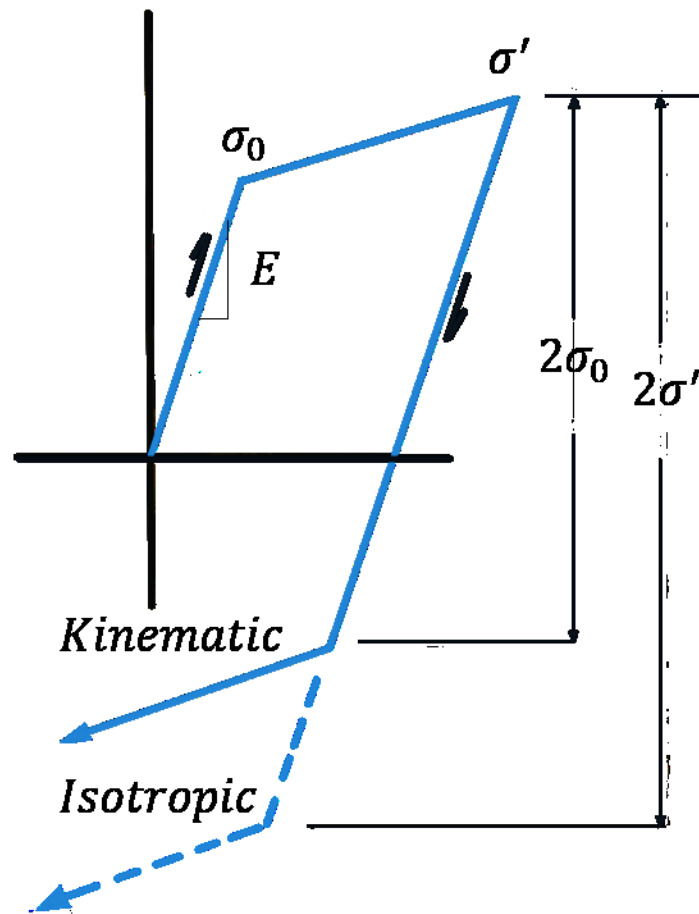


Figure 2-9. Kinematic and isotropic hardening models' unloading behavior

The total strain theory of plasticity uses a hardening rule to predict and describe how hardening (or softening) occurs in a material when that material is exposed to stress reversals. Although many researchers in the field of plasticity continue to develop permutations and augmentations to the classical approaches, the two prevailing theories that currently see broad application across finite element material models are isotropic and kinematic hardening rules (Abdel-Karim, 2009; Chen et al., 2005; Frederick & Armstrong,

2007). The two rules are illustrated in Figure 2-9. It is important to note that isotropic hardening is consistent with an overall expansion of the yield surface of a material. Isotropic hardening implies that stress-induced hardening of the material through either tensile or compressive loading serves to extend the yield strength of the material in its opposing stress state as well. Alternatively, kinematic hardening represents a translation of the yield surface. Consequently, a material experiencing a gain in yield strength through exposure to tensile stress loses an equivalent capability on the compression axis. A Bauschinger effect is well-documented in cyclic steel loading, suggesting that it is prudent to account for this behavior in any numerical applications of material behavior for predicting post-yield effects on steel if the steel may be expected to experience significant contra-stress to the mean stress direction (Chaboche, 2008).

2.3.3 Flow rule

In metal plasticity, a flow rule is an underlying assumption concerning how a plastic strain increment and the deviatoric stress tensor are oriented (Chen & Han, 1988). A common flow rule sets the principal directions of the two variables as co-linear. Thus, the flow rule provides a mathematical description of how material flows beyond its initial yield. It is roughly a relationship between plastic strain and stress. The flow rule can take various forms including a direct form, ϵ^p , an incremental form $d\epsilon^p$, or a rate form, $\dot{\epsilon}^p$.

Under multi-axial loading, the direct form relates the principal components of strain during plastic loading to the principal stresses. In other words, the direct form relies on the key tenet of deformation theory, namely, that a single curve relates the effective stress, $\bar{\sigma}$, and the effective strain, $\bar{\epsilon}$, for all states of stress. Conversely, the incremental form of strain

theory specifies the relationship between a small increment of plastic strain, $d\epsilon_{ij}^p$, in terms of the strain, stress, and stress increment, $d\sigma_{ij}$. Numerous experimental results have provided a wealth of evidence indicating that plastic strains show dependence on both stress magnitude and stress loading history. This so-called load path dependence gives rise to proportional loading, in which the loading path is a straight line through the origin, and non-proportional loading, which displays a non-linear load path. The result of load path dependence is the development of situations in which the plastic strains in a material undergoing a history of loading differ despite the final stresses being the same.

Analysis of such path-dependent behavior necessitates an incremental plasticity theory. The equations governing incremental theories are similar to those of deformation theory. However, used in FE applications, incremental theories replace all plastic strains with a corresponding differential quantity, $d\epsilon^p$, or a rate form, $\dot{\epsilon}^p$ (depending on the use of rate-independent constitutive relationships) when performing numerical integration of stress-strain relationships across the timesteps of the simulation. For a more comprehensive discussion of the mathematics undergirding flow rules, the reader is referred to any of the treatises on plasticity identified within this text's references.

2.4 Deformation models

Many FE programs employ pre-programmed deformation models featuring underlying mathematical treatment that applies the combined attributes of a yield condition, flow rule, and hardening rule to user-customized material inputs (such as those taken from uniaxial test data) to reflect behaviors that differ between individual materials. Across the literature, similar phenomena and impact behavior have been observed and

reported through the lens' of seven common models. The most-reported models are summarized below to familiarize the reader with the commonalities of material assumptions made in multi-impact experimentation.

2.4.1 Elastic deformation models

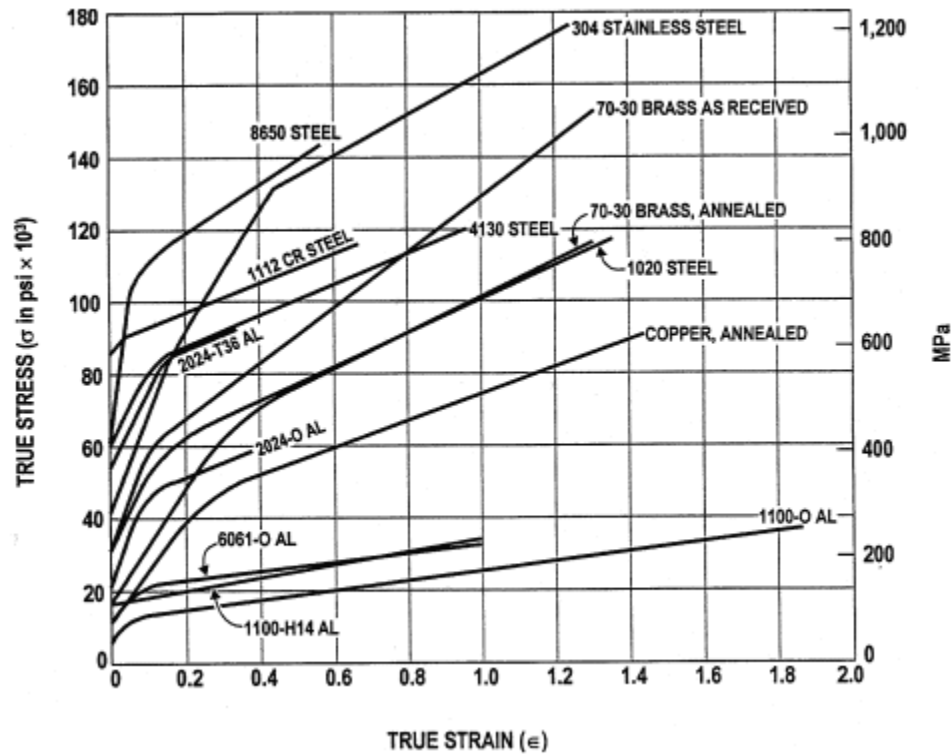


Figure 2-10. True stress-strain curves in tension at room temperature for various metals²

$$\sigma = E\varepsilon \quad [10]$$

Mild steel demonstrates linear elasticity over a narrow elastic range, as illustrated by Figure 2-10. When a steel specimen is subjected to small strains, where σ is the experienced stress, the resulting strain, $\varepsilon_{elastic}$, can be described via the relationship the

²Adapted from <http://totalmateria.com>

stress and strain have with Young's modulus, E , for the material (Hibbeler, 2001). Within the elastic range of the material, this is a relationship of proportionality governed by Hooke's law, as described in equation (10). Given the strong linearity of steel specimens, elastic deformation models are comprehensively explained by the infinitesimal strain theory (Chen & Han, 1988).

2.4.2 Inelastic (Plastic) deformation models

Plastic deformation, in which a permanent dislocation of material occurs as a result of experiencing tensile, compressive, bending or torsion stresses in excess of the material's yield strength are commonly described using one of five constitutive models: elastic, perfectly plastic (bi-linear); elastic, linear hardening (bi-linear hardening); elastic, multi-linear hardening; elastic, power hardening; and, the Ramberg-Osgood model (Chen & Han, 1988; Johnson, 1989). Each model presents advantages and disadvantages which make them well- or ill-suited to different applications of structural investigation.

2.4.2.1 Elastic, perfectly plastic relationship

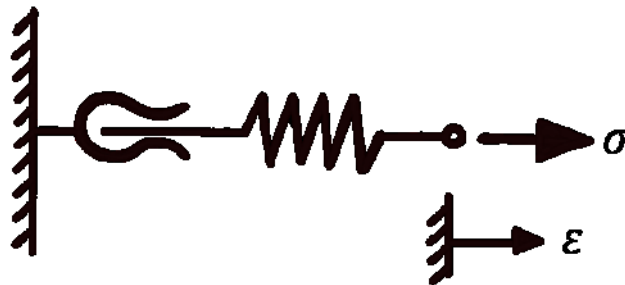


Figure 2-11. Elastic-perfectly plastic rheological model

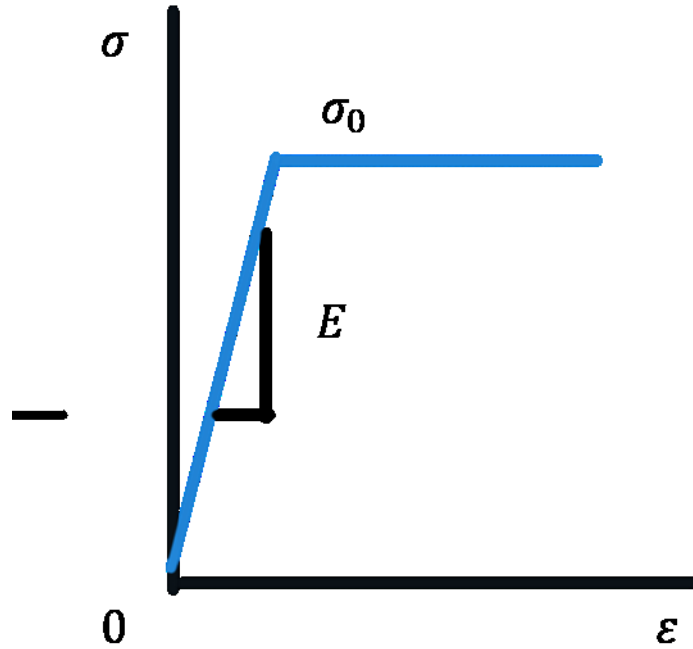


Figure 2-12. Elastic-perfectly plastic material model (graphical representation)

$$\sigma = E\varepsilon ; \text{ for } (\sigma \leq \sigma_0) \quad [11]$$

$$\sigma = \sigma_0 ; \text{ for } (\varepsilon \geq \frac{\sigma_0}{E}) \quad [12]$$

$$\varepsilon = \varepsilon_e + \varepsilon_p = \frac{\sigma}{E} + \varepsilon_p ; \text{ for } (\varepsilon > \frac{\sigma_0}{E}) \quad [13]$$

Stress-strain relationships that display flat behavior post-yielding are classified by two common naming structures, elastic, perfectly plastic or elastoplastic. Behavioral models, such as these, can be easily visualized using an analogous rheological model, as illustrated in Figure 2-11. In the rheological model, the deflection of the linear spring is representative of the elastic strain of known stiffness, while the frictional slider represents the plastic strain induced after overcoming the material elasticity (Dowling, 2007). An elastic, perfectly plastic model can be graphically depicted, as shown in Figure 2-12 and

described mathematically by equation (11) for the elastic portion of the response and by equation (12) for the plastic response. When a material specimen is subjected to testing beyond the yield point, the total strain can be represented by the sum of the constituents, as described by equation (13).

The elastoplastic model of material behavior is a sufficient approximation for research concerning elastic, and initial yield behavior of steel in force-displacement contexts (Daley & Hermanski, 2009). As a simple idealization, it generally shows good agreement for rough estimates of behavior even in cases where the material behavior demonstrated in a stress-strain test assumes a more complicated geometry (Barkey, 2018; Paik, 2018).

2.4.2.2 Elastic, linear-hardening relationship

In cases where the stress-strain curve shows significant hardening after yielding, an elastic, linear-hardening relationship can be a useful first approximation for the stress-strain behavior of the material. To apply this relationship, a tangent modulus, E_{tan} , must be applied to define the slope of the stress-strain curve after yielding. In this context, smaller values of E_{tan} give flatter post-yield behavior, so much so that an E_{tan} of zero results in the elastoplastic case (Paik, 2007).

$$E_{tan} = \frac{\sigma - \sigma_0}{\varepsilon - \varepsilon_0} \quad [14]$$

A traditional equation for the post-yield portion of the stress-strain curve can be defined by taking the slope between any point on the post-yield curve and the material yield point, as described by equation (14). Recognizing that the traditional stress-strain

curve is primarily limited in its accuracy to behavior that occurs before a material's ultimate tensile strength (UTS), Quinton (2015) proposed selecting the E_{tan} by defining a consistent particular endpoint. The endpoint governs a curve that correlates to the theoretical intersection of an extension of the post-yield curve with a graph point mapped at the material failure strain and the UTS.

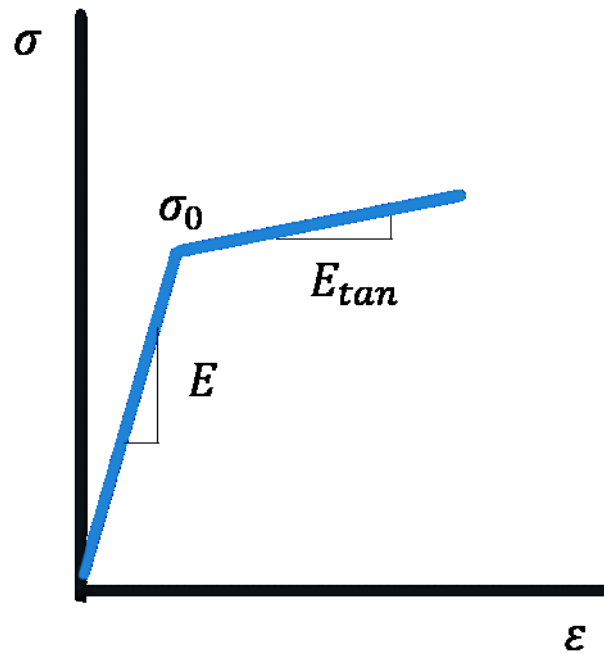


Figure 2-13. Elastic, linear-hardening material model (graphical representation)

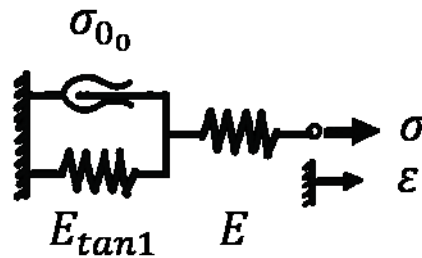


Figure 2-14. Elastic, linear-hardening rheological model

While the proposed E_{\tan} can be described graphically by Figure 2-13, by applying this modification to the total strain model, the total strain for an elastic, linear-hardening material in the post-yield region can be fully described mathematically by equation (15).

$$\varepsilon = \frac{\sigma_0}{E} + \frac{(\sigma - \sigma_0)}{(\varepsilon_f - \varepsilon_0)} \quad [15]$$

From a rheological perspective, the model may be viewed as a sum of strain energies absorbed by the two-spring, one-slider system depicted in Figure 2-14. In this instance, the elastic strain energy is applied to spring E_1 . The parallel combination of the frictional slider and spring E_2 comprises the plastic component of the decomposed strain. When the stress exceeds the slider yield strength σ_0 , plastic strain can accumulate. Beyond this point, the deflection of spring E_2 also describes the plastic strain (Dowling, 2007).

2.4.2.3 Elastic, multi-linear hardening relationship



Figure 2-15. Elastic, multi-linear hardening rheological model

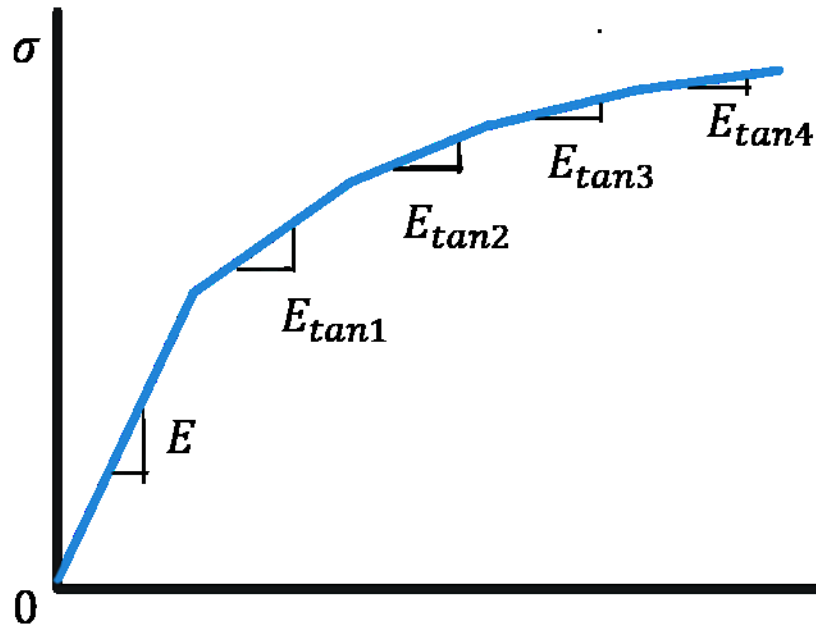


Figure 2-16. Elastic, multi-linear hardening material model (graphical representation)

An alternative method of approximating non-linear behavior presented in a stress-strain curve can be made using a series of line segments. The first segment corresponds with the elastic limit (yield strength) for the portion of stress-strain behavior obeying Hooke's law. Subsequent portions in the post-yield range comprise several varying slopes fit to represent the stress versus plastic strain behavior across a region of the post-yield space. A rheological model for visualizing this can be made using a linear spring as an initial elastic slope, followed by a series of spring and slider combinations configured in a parallel circuit. Each progressive spring is associated with an increasingly stiffer spring constant, analogous to a higher yield strength in each stress-strain segment (Dowling, 2007). The rheological visualization of a multi-linear hardening model and its

characteristic graphical representation are depicted in Figure 2-15 and Figure 2-16, respectively.

2.4.2.4 Elastic, power-hardening relationship

While the previous two sections have discussed simplified, linear representations of stress-strain behavior, various models exist on the basis that beyond a yield strength, the material experiences some stress which is proportional to strain raised to some power (a strain hardening exponent) and augmented by a hardening coefficient. This proposition is described in the elastic region by equation (16) and the in post-yield space by equation (17). Values of exponents and hardening parameters have been determined for a range of metals providing good fit for these equations. The power-hardening relationship can be expressed in strain terms according to equation (18).

$$\sigma = E\varepsilon \quad (\sigma \leq \sigma_0) \quad [16]$$

$$\sigma = H_1 \varepsilon^{n_1} \quad [17]$$

$$\varepsilon = \left(\frac{\sigma}{H_1} \right)^{\frac{1}{n_1}} \quad (\sigma \geq \sigma_0) \quad [18]$$

2.4.2.5 Ramberg-Osgood relationship

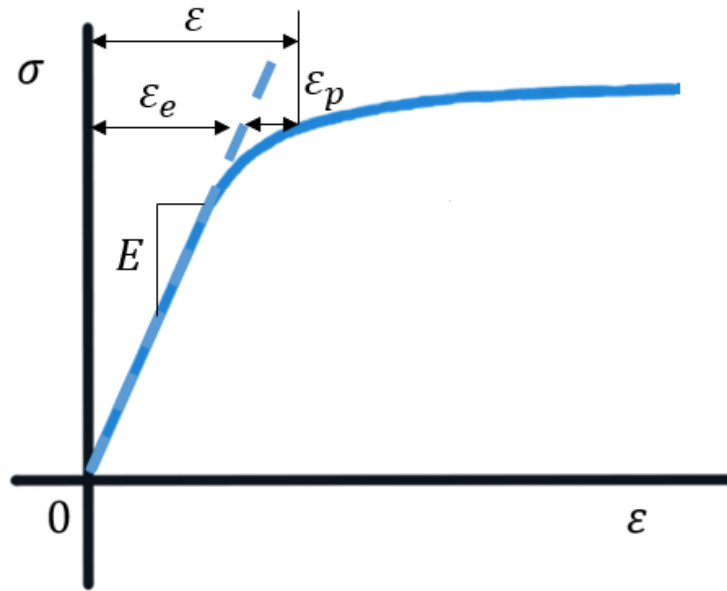


Figure 2-17. Ramberg-Osgood relationship

Ramberg & Osgood (1943) proposed a popular variant to the power-hardening behavior described in section 2.4.2.4. The Ramberg-Osgood (RO) variation is frequently used to describe non-linear behavior in stress-strain material data. In this variant, the total strain decomposes to its constituents, and each is treated separately and summed. The exponential relationship is applied only to the plastic strain as per equation (19), as opposed to the total strain application expressed by equation (18).

When using the Ramberg-Osgood relationship, the continuous nature of the curve results in an immediate and progressive deviation of the curve from the known elastic strain curve. However, given that elastic material response is reasonably well understood, one possible method of application of the Ramberg-Osgood relationship can use the elastic strain as identified by the deviation from the elastic slope, E , with the total strain

represented by the summation of the plastic and elastic components. Such an application is defined by equation (20), where the elastic component is provided by applying known material parameters consistent with the elastic proportionality constant.

$$\sigma = H\varepsilon_p^n \quad [19]$$

$$\varepsilon_{total} = \frac{\sigma}{E} + \left(\frac{\sigma}{H}\right)^{\frac{1}{n}} \quad [20]$$

The Ramberg-Osgood equation provides a single continuous curve for all values of σ but is not explicitly solvable. As a result, a stress-strain representation built using Ramberg-Osgood equations does not identify a distinct yield point (Figure 2-17) and must define a yield strength using a stress value which corresponds to a plastic strain offset, i.e., the 0.2% percent offset yield strength (Ramberg & Osgood, 1943).

2.5 Creep deformation models

A large body of the early theoretical work (Bree, 1967) on progressive plastic accumulation, ratcheting, and cyclic strain behaviors concerns itself with material performance at elevated temperatures such as high-heat pressure vessels, nuclear fuel cans, and steam pipe networks. Given that creep in engineering metals has a strong dependence on time-dependent behavior and material temperatures in the upper echelon of a material's performance envelope, the effects of creep deformation are mostly negligible and likely not a governing factor for examination of grillage performance at a moderate, steady-state temperature over a short-duration transient timeframe. Subsequently, creep effects have been excluded from the scope of the research outlined herein.

2.6 3-Dimensional stress states

Much of the accumulated plasticity literature to date has considered uniaxial tension test data, or limited applications of bi-axial tension states (Hübel, 1996; Paul, 2019). However, in indenter and impact testing, the presence of stress components in more than one direction will introduce effects to both a material's stiffness and yield strength (Xu & Yue, 2006). During plastic deformation, the discrete and equivalent stress states continue to affect a structure's behavior. Thus, any deformation plasticity previously introduced must be expanded to include the nature of the stress state and how it is applied. For example, experimental results suggest that plastic strains that accumulate in a material depend not only on the value of stress developed, but also on the stress history (Dong et al., 2019). Dong et al. (2019) found that a sample loaded to particular axial or torsion values, each capable of inducing plastic strains on their own, produced different resultant plastic strains depending on which load was first applied. This load path dependence—in particular, the instance of an unloading portion—necessitates an incremental plasticity theory to appropriately express the differential strain quantities throughout the loading cycle(s) of the experiment (Chen & Han, 1988).

2.7 Cyclic loading and unloading



Figure 2-18. Strain-time history for cyclic loading: unloading remains elastic (left), unloading into compressive strain range before reloading (center), and cyclic reverse plasticity (right)

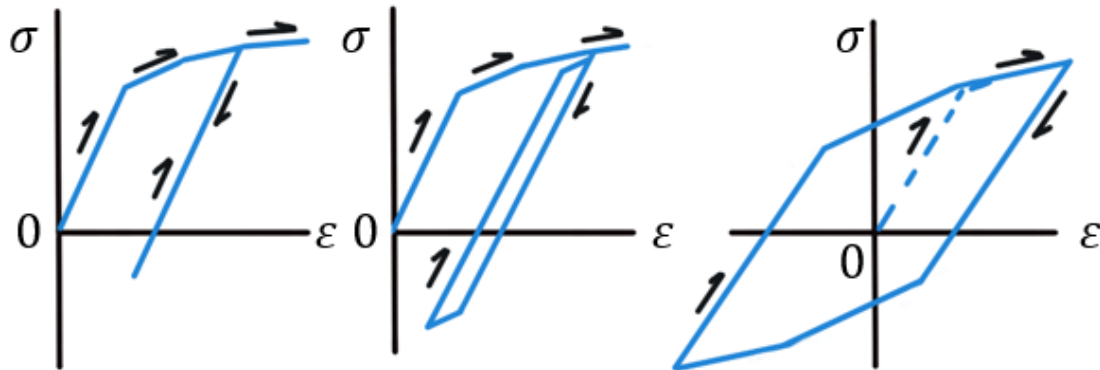


Figure 2-19. Corresponding stress-strain hysteresis plots for Figure 2-18

Consider a structure that has been loaded in a state of tension passed yielding into the plastic regime. If a structure is unloaded, or the direction of loading is reversed, the structure unloads following the slope of the elastic path until the structure is fully unloaded. As the structural response reversal of loading continues passed this point, the compressive response is elastic following this same curve until such a point that yielding occurs in this opposite stress direction. If the stress response is sufficiently large, a reversed strain occurs.

For a wholly reversed loading, the behavior is symmetrical about the origin for each cycle of the loading. The strain history of the loading can be mapped as a series of loops on a stress-strain plot. These hysteresis loops exhibit a variety of behaviors depending on the load history, structural geometry, and material behavior of the component or structure, as illustrated for an elastic, non-linear hardening model by Figure 2-18 and Figure 2-19.

2.8 Stress-strain summary

The majority of commonly employed relationships used to fit experimental stress-strain curves for mild steels feature a linear-elastic behavior until a unique yield point is reached. Relationships that are bi-linear with the second linearity having a slope of zero are elastic, perfectly plastic. Elastic, linear hardening relationships feature a similar bilinear curvature; however, a tangent modulus of increasing slope is used to describe the hardening behavior. Alternatively, power relationships may define an elastic portion followed by an exponential curvature described by a strain hardening parameter and a hardening coefficient. Finally, the Ramberg-Osgood relationship approximates the entirety of an experimental stress-strain curve but requires an assumption of the value corresponding to the material's yield point. Regardless of the model selected, the aggregate of elastic and plastic strain at a given stress value can define the total strain of the material. A plot of these values along stress-strain axes provides a curve that can be used in FE analysis with incremental plasticity theory to describe three-dimensional states of stress using two-dimensional finite elements.

2.9 Overview of ratcheting mechanism and phenomena

Numerous synonyms have described progressive plastic accumulation, but one of the key underlying mechanism(s) of interest manifests as the phenomenon of ratcheting. Ratcheting, as observed in materials subject to cyclic loading, has received heightened interest in recent years. As shown by Paul (2019), the number of annual publications key-word coded to include ratchet effects has increased by an order of magnitude versus the state of the experimental field twenty years ago. Despite the increase in interest, there remain numerous discrepancies with the framework, terminology, and context used to describe work by researchers in the field. Moreover, while there are preferences, there is not yet a consensus as to which constitutive equations are best-suited for numerical experimentation of ratcheting behaviors. These issues are compounded by the fact that outside of dedicated investigators considering ratcheting behavior, the term is widely unknown or misapplied by commercial engineers working in steel structure (Hübel, 1996)). This section intends to provide an introduction and overview of the ratcheting phenomena, explicate a framework for discussion by defining key terms related to the observations recorded in this research, as well as describe the current research landscape and identify any gaps open to investigation.

2.9.1 Introduction to ratcheting

Interest in the ultra-low-cycle fatigue behavior in which plastic deformation accumulates due to a cyclic mechanical or thermal stress was first described in a seminal paper by Bree (1967). Since then, the phenomenon has not only been repeatedly observed in the fast-nuclear-reactor fuel elements initially discussed by Bree but myriad engineered

structures of varied cross-sectional design ranging from individual specimens to component-level complexity exposed to various thermal and mechanical applications (Hübel, 1996). The observed behavior, which can be characterized as the progressive accumulation of plastic deformation in a preferential direction when exposed to a cyclic load, is termed ratcheting or ratchetting (Hübel, 1996).

Paul (2019) comprehensively reviewed the aggregated trends in experimental ratcheting research to date, noting two important observations. First, there has been growing research interest in ratcheting behaviors in the past several decades. However, it is only recently that the introduction and validation of non-linear kinematic hardening (NLKH) models mathematically describing the phenomenon have been integrated into finite element codes in such a way as to permit significant modeling and experimentation of ratcheting behavior in complex 3-dimensional geometries. Secondly, a growing recognition that cyclic plastic deformation is an underlying mechanism that can severely limit fatigue life of engineered components to levels far beneath those proposed by current design standards emphasizes the importance of ratcheting as a high-profile topic of engineering research in mechanics.

2.9.2 Defining ratcheting

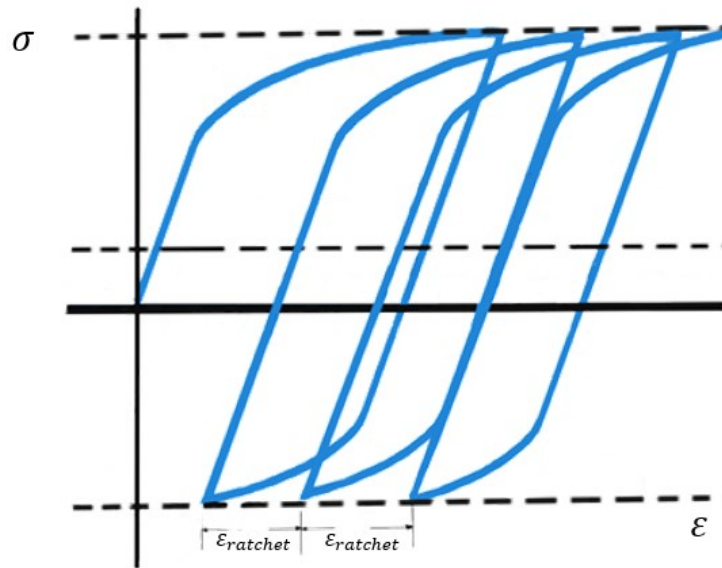


Figure 2-20. Open hysteresis behavior illustrating ratcheting mechanism

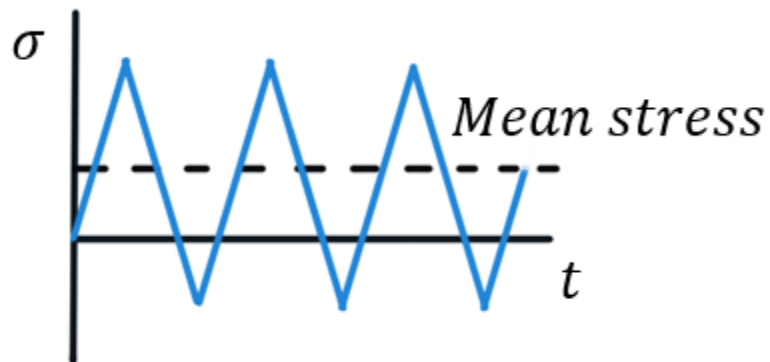


Figure 2-21. Stress-time plot illustrating conditions for ratcheting

Hübel (1996) notes that although there are many methods of analysis for ratcheting behavior, comparison across methods is made more difficult because there is currently no single definition of ratcheting broadly accepted across the extant branches of ratcheting research. In the following text, ratcheting will be defined by the criteria established by

Hübel (1996). Thus, ratcheting is viewed synonymously with progressive plastic accumulation, which occurs if:

when a structure is subjected to cyclic loading, the mean strain (arithmetic mean of maximum and minimum strain during one loading cycle) changes during any one loading cycle at at least one point of this structure with respect to the mean strain induced during the preceding cycle due to inelastic material behavior (p. 56).

In stress-strain space, the behavior can be plotted as a series of open hysteresis loops illustrated by Figure 2-20. As a cyclic response in stress-time, ratcheting can be viewed as non-symmetric mean stress shown in Figure 2-21.

2.9.3 Delineating between ratcheting behavior and other fatigue behaviors

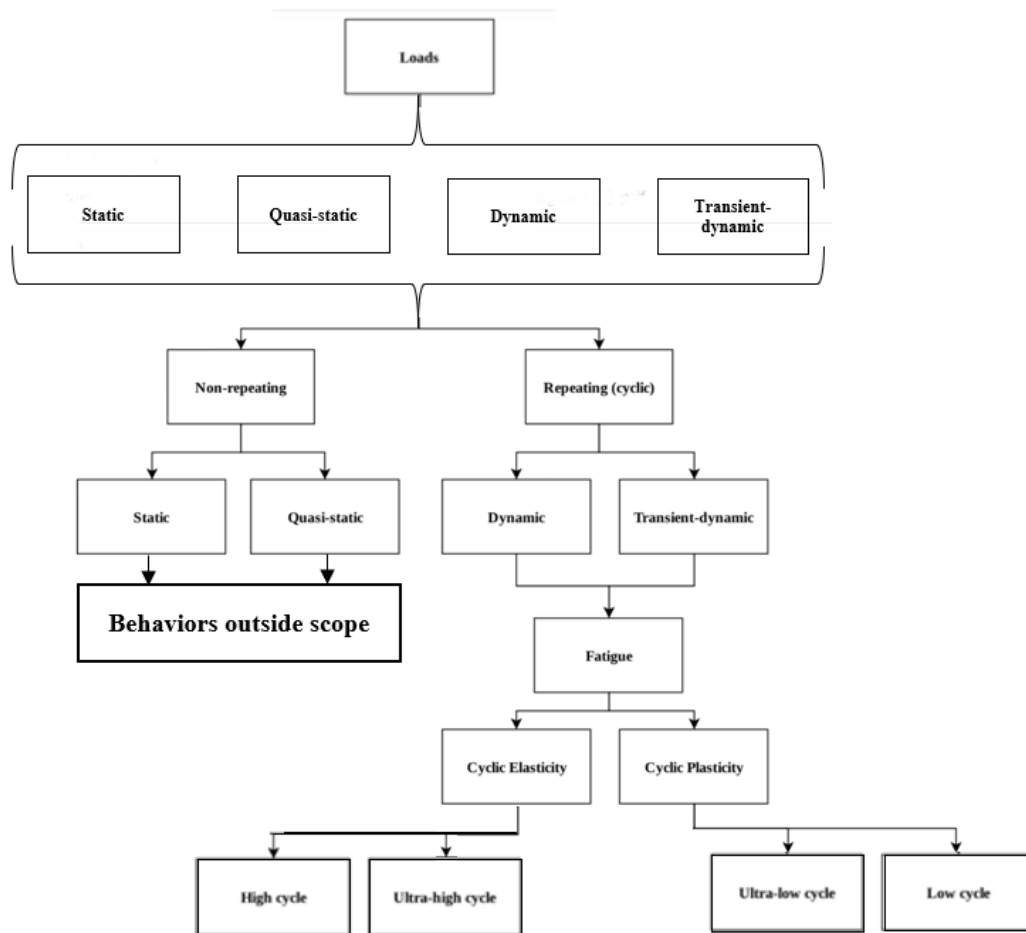


Figure 2-22. A selected taxonomy of loading behaviors

The problem space containing ratcheting behaviors can be defined beginning from a macroscopic overview of mechanical loads, and decomposing these loads into sub-categories until the material response is isolated. Broadly speaking, the loads may comprise static, quasi-static, dynamic, or transient-dynamic behaviors, each of which can be further decomposed into non-repeating loads and repeating (cyclic) loads. Each category can continue to be sub-divided into its constituent classes. However, as summarized in Figure

2-22, the scope of this discussion is truncated and refined to consider the nature of repeating cyclic loads. The loads in question lead to one of two fatigue behaviors, termed cyclic plasticity and cyclic elasticity.

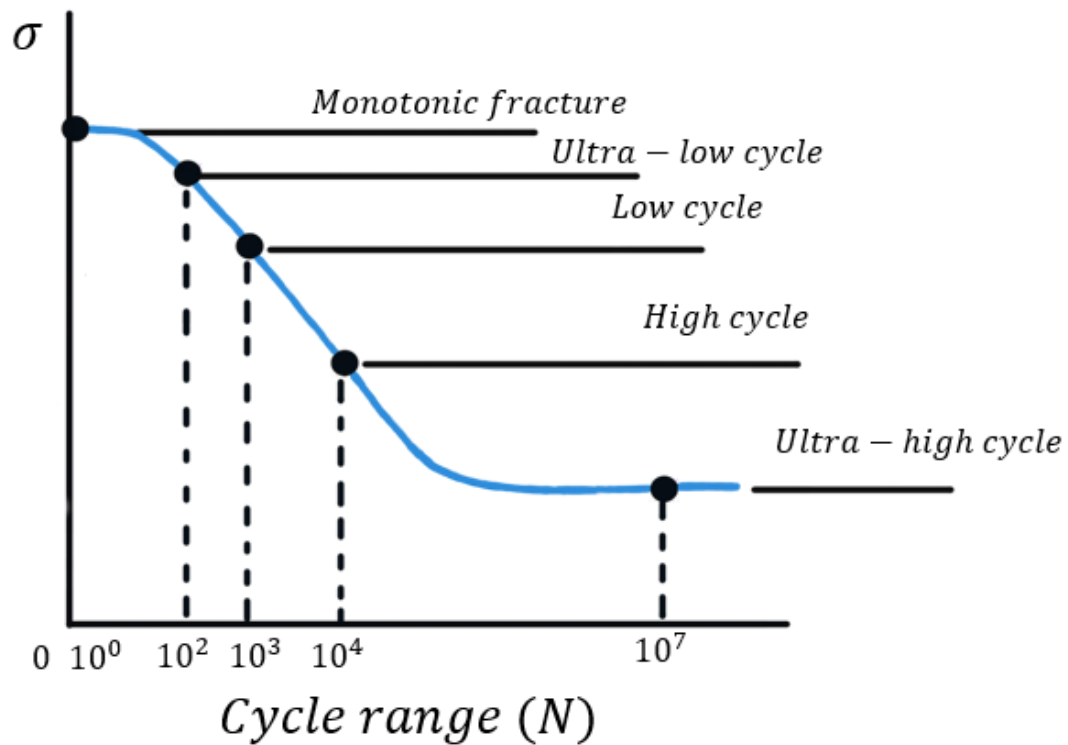


Figure 2-23. Nominal cycle frequency ranges

Cyclic elasticity encompasses material behavior when a specimen, component, or structure is exposed to stress-strain patterns within the material's elastic limit at high and ultra-high cycle frequencies. Conversely, cyclic plasticity is observable in low cycle, and ultra-low cycle frequency ranges when a material is exposed to stress-strain ranges inducing plasticity. The cycle range delineating these frequency ranges is depicted in Figure 2-23.

2.9.3.1 Low cycle fatigue

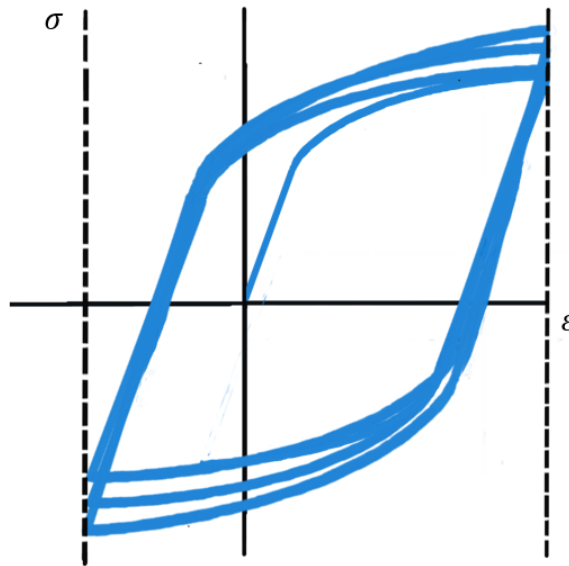


Figure 2-24. Hysteresis loops illustrating low cycle fatigue (symmetric stress cycling)

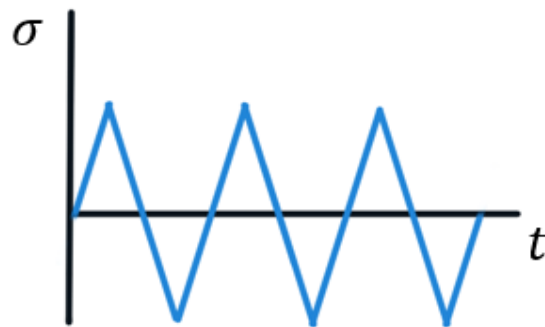


Figure 2-25. Stress-time plot illustrating conditions for symmetric stress cycling

The key distinguishing feature between low cycle fatigue and ratcheting actions can be explained by stress response versus time. Consider the low cycle fatigue hysteresis loop plotted in Figure 2-24 and the stress-time response in Figure 2-25 as compared with the response in section 2.9.2. The two responses demonstrate symmetric stress cycling and asymmetric stress cycling, respectively. The key takeaway from inspection of these figures is the understanding that the non-fully reversed nature of the stress in asymmetric cycling

permits persistent mean stress. Repeated mean stress creates the environment necessary for accumulated plastic strain and a distinct failure mode from that currently assessed by historical fatigue endurance analysis.

2.9.3.2 Mean stress relaxation

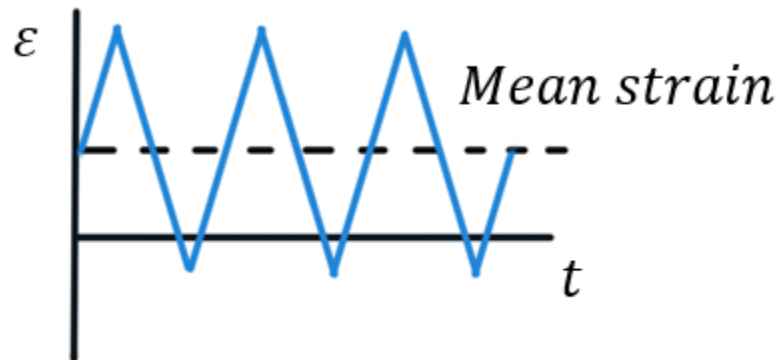


Figure 2-26. Strain-time plot illustrating asymmetric strain cycling (mean stress relaxation)

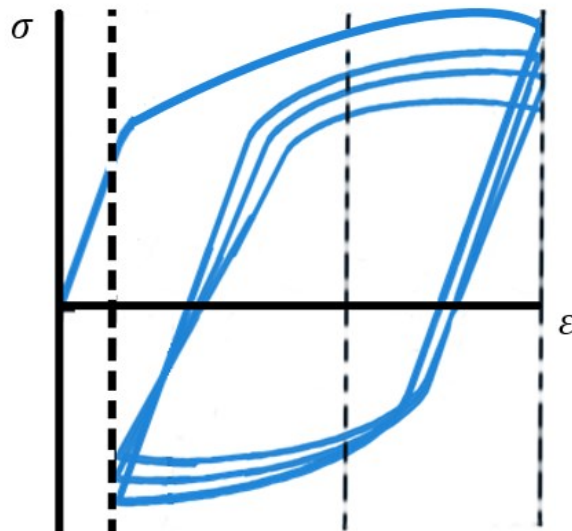


Figure 2-27. Hysteresis loops illustrating asymmetric strain cycling (mean stress relaxation)

Mean stress relaxation is a phenomenon occurring when a structure is exposed to an asymmetric strain cycle (Figure 2-26). While the strain remains constant over several cycles, the peak stress progressively dissipates with each cycle, as shown in Figure 2-27.

2.9.3.3 Elastic shakedown

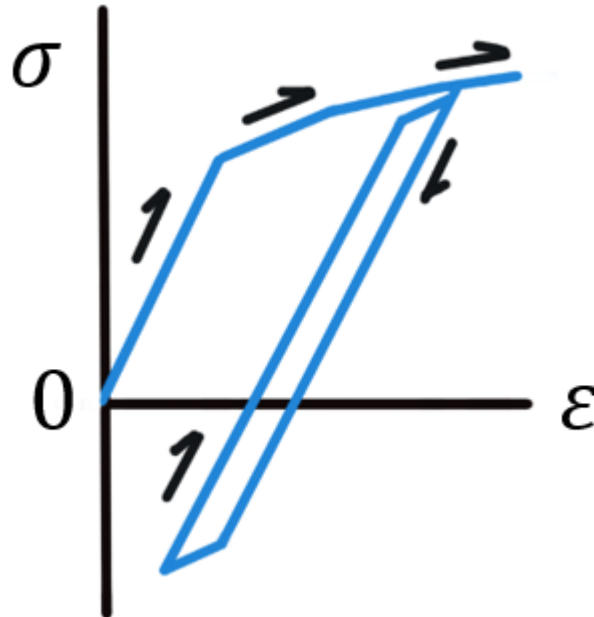


Figure 2-28. Elastic shakedown

In industry, elastic shakedown is commonly interpreted as a fatigue or ‘running-in’ effect of structures and components, but the mechanism or sequence of actions is not very well-defined. Formally, hereafter this research will align with the definition proposed by Bree (1967) and supported by Hübel (1996), in which elastic shakedown is a structural state in which a structure responds elastically under any number of cycles after some initial plastic straining during the first cycle. The stress-strain behavior can be visualized, as illustrated in Figure 2-28.

2.9.3.4 Plastic shakedown

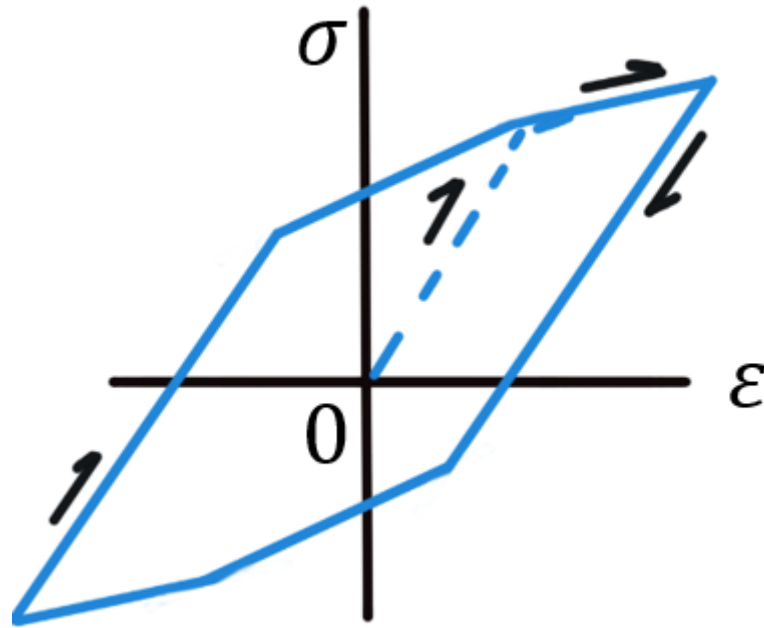


Figure 2-29. Plastic shakedown (alternating plasticity)

In contrast to elastic shakedown, plastic shakedown can be defined as a pseudo-elastic structural state via alternating plasticity (Paul, 2019). Structures that shakedown plastically exhibit behavior in which the plastic strain resulting from the tensile loading half-cycle is reversed during the structure's compressive loading half-cycle, creating a closed hysteresis loop. The alternating nature of the plasticity compounds low cycle fatigue damage to a structure (Lee & Barkey, 2012). The stress-strain behavior of a plastic shakedown event is illustrated in Figure 2-29.

2.9.4 Factors affecting ratcheting

Paul (2019) comprehensively reviews the state of ratcheting research. Among his

key findings are that several factors influence the extent of ratcheting, including the load condition; mean stress; stress amplitude; stress ratio; and, the load history. Additionally, Hübel (1996) emphasizes that the nature of the cyclic behavior, be it ratcheting, relaxation, or shakedown phenomena that will develop for a particular configuration or structure, is variable based on the contributions of the ratcheting factors summarized by Paul (2019).

2.10 Gravity-based impact & indentation theory

Within mechanics, a force applied to two or more bodies dynamically or transiently as opposed to a quasi-static or static force may be sub-categorized as an impact. More simply, an impact is a sudden change in force experienced over a short period by two colliding bodies. Consequently, the effect of a given impact is fundamentally governed by the relative velocity and relative stiffness' of the colliding bodies (Goldsmith & Frasier, 1961).

Even the most superficial examination of the body of knowledge in mechanics shows a rich and detailed history of experimentation involving the collision of objects and the subsequent observation and recording of various parameters of interest to discern the theoretical and practical effects of various impact scenarios. Gravity-based experimentation, in which the experimental apparatus relies on force(s) generated in total, or part, by gravitational acceleration, is a storied and continued trend in experimentation (Johnson, 1989). The frequency and application of such tests are innumerable. Even the current state of the art (SOTA) see well-regarded material testing establishments such as

*SAE*³, *ASTM*⁴, and *Instron*⁵, etc. producing tests, protocol, and equipment to support impact and drop testing applications. The long experimental history, and relatively well-known methods and constraints of such testing methodology combined with construction technology advances permitting the scalability of test solutions, makes gravity-based testing a standard, economic, and well-suited application for more substantial scale impact scenarios.

2.10.1 Impact testing rationale

The purpose of impact testing is to reliably, repeatedly perform a controlled energy application to determine the energy absorbed by, or the energy input required, to create a specified level of damage to a test sample. In a controlled laboratory setting, impact testing is an efficient and highly repeatable series of experiments to validate designs and hypotheses identified in a theoretical or numerical context (Hayward, 2004).

2.10.2 Energy and impact force relationships

Energy balances using the work-energy principle are the essential constituent of experimental validation for impact scenarios. Take, for instance, a fundamental work-energy principle in which the work performed on an object (that is the average impact force times the travel distance) is equal to the change in kinetic energy of the object. From this knowledge, an enormous amount of information can be extrapolated concerning the mathematical behavior of materials under a loading condition. The challenge for

³ SAE: https://www.sae.org/standards/content/j1727_201502/?id=j211/1_201403

⁴ ASTM: <https://www.astm.org/Standards/E2298.htm>

⁵ INSTRON: <https://www.instron.us/en-us/products/testing-systems/impact-systems/9400-series-drop-tower>

researchers is to obtain energy values via a physical test method. The most direct solution is to measure the impact force, relate this force to the displacement of the body, and then integrate the area comprising the boundaries of the force-displacement curve. The result of this calculation is an energy value.

2.10.3 Common variations on impact tests

2.10.3.1 Free-falling weight test

A common variation of impact testing is the falling-weight impact test. The test drops a projectile, which may or may not be independently instrumented, from a known and fixed height onto a test specimen. The effective speed at impact is calculated or observed and recorded in order to back-calculate forces, deflections, or energies as appropriate. Falling-weight impact tests generate effective impact speeds in a range of 1 to 4 ms⁻¹ (Plummer, 2014).

Consider the following questions of immediate concern to an experimentalist. What is the impact velocity of the indenter? Does the mass of the indenter matter? How does the growing indentation with each subsequent drop affect the acceleration or final velocity of the indenter? Is the indentation location relevant? Does a significant deformation mean that there was a high impact force or a low impact force? Just these few questions illustrate that even a simple set-up presents myriad issues in understanding the dynamics at work in the most fundamental impact. The depth of these questions is compounded by the fact that a number of the answers can appear counter-intuitive, even to those who have studied engineering and physics at an introductory level.

2.10.3.2 Pendulum impact test

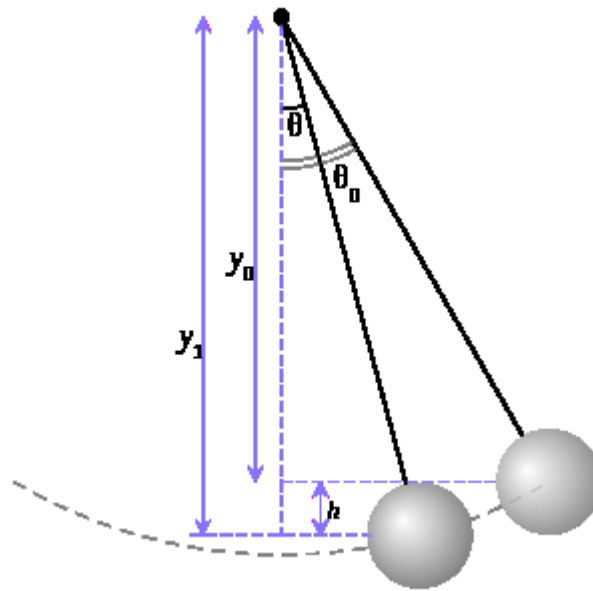


Figure 2-30. A simple gravity pendulum⁶

A pendulum is a suspended body free to oscillate along a trajectory described by the body's suspended length from fixed support as gravity acts on the body. When the body is subjected to a displacement from its equilibrium position, gravity exerts a restoring force to accelerate the mass back towards equilibrium. The physical model can be idealized as a simple gravity pendulum, as depicted in Figure 2-30, which is a mathematical model that makes several simplifying assumptions to develop an analytical relationship that correlates kinematics and energy theory. Fundamental to this mathematical derivation are the following five assumptions:

1. The pendulum arm on which the bob swings is massless and rigid.
2. The pendulum is treated as a point mass concentrated at the pendulum bob.

⁶ Adapted from: <https://en.wikipedia.org/wiki/Pendulum>

3. Motion is constrained to two dimensions, thereby tracing an arc.
4. The gravitational field is constant throughout the region of interrogation.
5. The support structure is frictionless and rigid.

In standard pendulum impact tests, a weighted pendulum arm is held at a given height, related to the angle of inclination of the impact arm. The inclination determines the potential energy of the pendulum. When released, the impact of the pendulum and the specimen may create deformation or fracture of the specimen, as well as the recoil of the pendulum bob. The data produced by this impact can be used to determine the impact energy of the specimen. Pendulum impact tests may often be instrumented with load transducers on the indenter, allowing load-displacement curves to be generated and permitting analysis by fracture mechanics theories (Polocoşer et al., 2017). Moreover, Polocoşer et al. (2017) also note that pendulum impact tests can serve as a rapid assessment of material behavior when used at an appropriate range of sub-ballistic effective test speeds.

For an impact test, a specific application of energy conservation is applied. The application equates the potential energy of the indenter before the drop and its subsequent kinetic energy at impact, as shown in equation (21).

$$U_{potential} = \Delta W_{kinetic} \quad [21]$$

The impact velocity of a pendulum indenter and its associated impact force can be obtained using principles of energy conservation. The energy balance, gravitational potential energy, and kinetic energy are described by equation (21), equation (22), and

equation (23), respectively. Subsequently, the velocity at impact can be found using equation (24), permitting the calculation of net work and impact force to become a trivial matter. With these descriptions, only the equivalent gravitational potential height is left as an unknown in the energy derivation.

Recognizing that the input energy in this instance is gravitational potential energy stored in the indenter as it is held above the plate, the potential energy in the system can be defined by equation (22). Likewise, the kinetic energy can be expressed mathematically according to equation (23).

$$U_{potential} = mgh \quad [22]$$

$$\Delta W_{kinetic} = \frac{1}{2}mv^2 \quad [23]$$

Substitution of equation (22) and equation (23) into equation (21) reveals that the mass term is redundant. A simple rearrangement of the terms to express the impact velocity as per equation (24) demonstrates that for impact scenarios employing gravitational acceleration as the sole motion constituent, and thus neglecting drag forces caused by bluff body resistance in air, the resulting impact velocity depends on the drop height.

$$v = \sqrt{2gh} \quad [24]$$

Considering the simple gravity pendulum depicted in Figure 2-30, if a pendulum is permitted to begin its swing from some initial angle θ_0 , then the mensuration becomes a trivial application of trigonometry. Given an initial angle of θ_0 , and an impact angle of θ_1 , the vertical distances from the pendulum bob to the fixed support can be defined as y_0 and y_1 described by equation (25) and equation (26). The effective height, h , represents the

difference between the two equations above, with L denoting the length of the pendulum arm. The calculation of the effective height is described by equation (27):

$$y_0 = L \cos \theta_0 \quad [25]$$

$$y_1 = L \cos \theta_1 \quad [26]$$

$$h = L(\cos \theta_1 - \cos \theta_0) \quad [27]$$

The substitution of equation (27) into equation (24), provides the impact velocity for the mass on a pendulum at any given lift angle as denoted by equation (28) such that the associated impact energy for two pendulums of approximately equal mass can be described as equation (29).

$$V = \sqrt{2gL(1 - \cos \theta)} \quad [28]$$

$$E = mV^2 \quad [29]$$

2.10.4 Application of linear pendulum theory to nonlinear pendulums

It is important to note that while both the simple (linear) pendulum and nonlinear pendulum consist of a mass, m ; an arm length, L ; and a fixed pivot point, O; there are significant differences in the development of their periodic motions. When dealing with small angles of inclination, the frequency and period of the pendulum is assumed to be independent of the initial angular displacement or amplitude of the pendulum. This approximation is encapsulated by the discussion provided in section 2.10.3.2. While the period for a simple pendulum is thus independent of the mass or initial angular displacement, a real nonlinear pendulum such as that used in the experimental test apparatus has an angular displacement large enough that the small-angle approximation no longer holds.

Consequently, the equation of motion for the pendulum at any given point in its motion is described by a nonlinear differential equation that must be solved numerically given that it has no closed-form solution, as detailed in equation (30).

$$\frac{d^2\theta}{dt^2} + \frac{g}{L}\sin\theta = 0 \quad [30]$$

The discrepancy between linear and nonlinear pendulum theory does not affect the proposed experimental set-up given that the speed of the pendulum throughout its motion is not of paramount significance to the study. Instead, the experimental set-up proposes to use the speed at two distinct, known points of consideration in the pendulum's motion, namely, the starting height and the speed at the bottommost portion of the pendulum's motion. Thus, regardless of the nature of the pendulum, the speed at these two locations is known with a high degree of confidence through the application of gravitational potential to kinetic energy balance.

2.11 State of the current literature

Many researchers and investigators (Alsos & Amdahl, 2007; Mansour et al., 1990; Murray, 1965; Zhu et al., 2018) have suggested that ratcheting may play a significant role in safety, survivability, and lifetime failure strength of ship structure. However, there was limited research directly linking the phenomenon to its response in ships subjected to repeated or cyclic impact behavior (Jones, 2006). Even the most recent literature frames much of this research in the context of lifetime effects to a ship's overall fatigue life versus examining the risk of ultra-low cycle plastic strain accumulation within, for instance, a single mission or operation of a ship (Hu & Chen, 1996). Ratcheting behaviors have been

largely confined to uniaxial or simple bi-axial examination under constrained tensile-test apparatus experiments, experimentation supporting high-heat flux applications, or the development of constitutive models to mathematically describe the phenomenon (Paul, 2019). Repeated impacts have been broadly relegated to small-scale experimentation using repeated mass impacts. Large, full-scale laboratory and numerical experimentation begin to appear more widely in the literature after 1990 (Zhu, 1990). A brief synopsis of seminal papers concerning the state of ratcheting research and repeated impact literature, which influenced the direction of this investigation, is presented as follows.

2.11.1 Ratcheting

As early as 1950, Murray and other researchers highlighted that most overall ship fracture was likely to result from a combined state of low cycle fatigue and ratcheting (Murray, 1965). Bree (1967) completed the first in-depth theoretical work on the analytical description and stress interaction boundaries of ratcheting and associated mechanisms. Bree's work was confined to a simplified elastic, perfectly-plastic analysis of high-heat nuclear fuel cans. From this work, research intensified mainly in high-heat applications and became prominent in design codes for nuclear power structures. Considerable interest in soil plasticity and ratcheting effects was also heavily researched, aided by the development of constitutive models to enhance yield criteria (Drucker & Prager, 1952). By 1970, the concept of ratcheting was proposed as a field for serious study in load conditions extending beyond cyclic heat applications and extending into all ductile metal structures subject to both cyclic and monotonic strains (Coffin, 2009). Mansour et al. (1990)

suggested that ratcheting influence was noticeably absent in the calculation of plastic damage rate for ship hull ultimate strength.

A body of work was conducted in the early 1980s and 1990s by a collection of Japanese researchers, with a direct correlation to ratcheting in ship hull structures (Fujita, Nomoto, Yuge, 1984; Fukumoto & Kusama 1985a, 1985b). Fujita et al. (1984), considered the ratcheting response of columns and stiffener type components, while Fukumoto and Kusama (1985a, 1985b), examined the effects of uniaxial cyclic loads applied to both plate elements and thin-wall box beams. Huang (1999), conducted similar investigations expanded to include these components in ship structural configurations and concluded that the plastic deformation induced by severe sea conditions was sufficient to allow accumulation of plastic deformation under cyclic loads to cause failure in ship structures even though the cyclic load was below the threshold for ultimate bending failure.

More recently, many publications have focused on low cycle fatigue and ratcheting of various types of shipbuilding steel under uniaxial, or simple bi-axial (tension-torsion) cyclic loading. Dong et al. (2019), concluded that there is a direct relationship between the mean stress and stress amplitudes with the degree of ratcheting strain. Moreover, they concluded there is an inverse relationship between the ratcheting strain and the resulting specimen fatigue life. Similarly, Paul et al. (2015), found that ratcheting results in permanent strain accumulation if either the conditions of increasing mean stress for a constant stress amplitude or an increasing stress amplitude for constant mean stress, are met. A combination of experimental and numerical work by Xu and Yue (2006, 2007), was used to study the correlation between traditional fatigue studies and fatigue studies using a

flat cylindrical indenter. The study's authors posit that indentation and impact responses can be used to evaluate ratcheting behaviors based on the authors' observations of strong similarities that exist between indentation fatigue behaviors as compared with traditional tensile test fatigue behavior.

Finally, Hübel (1996) provides an overview of aspects of ratcheting and cyclic loading. Hübel (1996) recognizes that ratcheting occurs both materially and structurally under many different conditions and is subject to wildly different applications of terminology depending on the dominant field of research within which it is being contextualized. Consequently, he explicates the phenomena, terminology, material configuration, stress states, structural geometry, and loading conditions that may introduce ratcheting concerns for structural analysts.

2.11.2 Response of stiffened plates to repeated impacts

Zhu and Faulkner (1996) amplified the work of Zhu (1990), conducting experimental research of repeated impacts to a fully clamped steel plate. The experimentation used a rail and carriage delivery system to repeatedly propel a rigid, knife-point wedge into a test plate, striking the center-of the plate. Zhu and Faulkner (2018) then developed simple formulae to guide the preliminary design of plates based on their findings. Zhu et al., (2018) expanded on the rigid-perfectly plastic method to evaluate the dynamic response of this same plate-indenter configuration with an impact location at any point across the plate. The results showed good agreement with their proposed numerical model, and the findings highlighted the influence of strain rate, strain hardening, and proper evaluation of material elasticity to provide predictive theoretical simulations.

Jones (2014) applied a theoretical treatment to the problem of repeated mass impacts with accumulated masses (the cargo loading problem), resulting in the proposition of a pseudo-shakedown condition, which may or may not, be seen in asymmetric stress loaded conditions depending on the structural configuration. Recently, increased interest in Arctic and cold region engineering has led to pronounced ice-class vessel research. Zhu et al. (2015) published ice load-response models to study ice-classed ship plating under repeated impacts from drift ice, while Cho et al. (2014), as well as, Truong et al. (2016), Truong et al. (2018a), and Truong et al. (2018b) performed experimental and numerical investigations concerning the role of repeated impacts on the response of steel beams, plates, and stiffened plate structures under room and sub-zero temperatures. Somewhat analogous to the research proposed herein, Huang et al. (2000) and Park et al. (2015) performed repeated impact tests on a clamped, square, mild steel plate using a hemispherical indenter on a Drop Hammer apparatus. A key finding from Huang et al. (2000) indicates that as transverse displacement grows for the axially-restrained plate, a discernible increase occurs in elastic strain energy.

2.12 Research questions arising from literature review

Ratcheting phenomena as they occur in cyclical hardening and softening materials have been widely considered experimentally under tension-compression or tension-torsion cyclic loading with standard fatigue coupons. Limited development has also been investigated using indentation-style testing. A review across the open literature reveals that while ratcheting results from both structural and material mechanisms, a vast majority of the research to date has focused on the material realm. In particular, much effort has been

devoted to the development of constitutive mathematical models that describe the material aspects of ratcheting. Hübel (1996) emphasizes that at present, a lack of analytical solutions for elastic-plastic indentation problems makes numerical simulation a useful tool for multiaxial deformation analyses. The often high computational and engineering costs associated with investigating the phenomena create a desire for simplified methods of analysis.

The emphasis on material behavior has led the work to predominantly employ variations of kinematic hardening behavior (Abdel-Karim, 2009; Chaboche, 1989; Chen et al., 2005; Frederick & Armstrong, 2007). However, Hübel (1996) advocates that one of the main difficulties in identifying ratcheting phenomena is that not all of them can be isolated in material tests or structural examinations in multi-axial loading. Experimentation to align the broad and competing veins of ratcheting research has been complicated by a relatively narrow application of loading configurations using specific geometries to reflect what is being used in the limited applications of current design codes. Consequently, to assess many of the structural considerations for plastic accumulation behaviors, the choice of material model and underlying hardening behavior can (and should) vary.

Cross-comparison of numerical results against perfectly-plastic, isotropic, and kinematic hardening models should permit consistent behaviors to be identified and aid the elimination of spurious behavior in numerical experimentation. Thus, Paul (2019) identifies a strong need to extend the breadth and scope of 3-D experimentation to build a repository of experimental results that use simplified inelastic analysis methods to rein in the geometry and loading conditions that result in different ratchet-like phenomena.

Among the many open areas for research, two essential questions waiting to be addressed concern the lack of experimental observation of other LCF effects and ratcheting interaction in structures, and the fact that real-space ratcheting phenomena are still not well-understood due to an insufficient volume of ratcheting responses under 3-D stress states.

The full-scale grillage impact experiments provide a bridge towards answers concerning outstanding ratcheting questions in a component/structural capacity, including:

- a) Is the structure capable of withstanding accumulated damage due to a load?
- b) Over what range of impact speeds does the grillage structure respond inelastically?
- c) How does repeated coincident damage accumulate in the grillages?
- d) How does this damage compare when similar load applications are applied across a span of the domain?
- e) What are the structural failure mechanisms associated with accumulated damage?
- f) Are there characteristic behaviors observable such as elastic shakedown, plastic shakedown, progressive plastic accumulation, or instantaneous plastic collapse?
- g) What impact energy/collision impact velocities bound these behaviors?

Chapter 3 EXPERIMENTAL METHODOLOGY

3.1 Introduction

The experiments described in this section were designed and carried out as part of an ongoing, comprehensive program examining myriad aspects of low- and non-ice classed vessels' structural response to impacts with ice. The project is partnered with Defence Research Development Canada (DRDC), the American Bureau of Shipping (ABS), as well as, Vard Marine Inc. The laboratory experiments were carried out throughout October and November 2019. The observations from that set of impacts form the basis for the validation of the numerical model developed, permitting exploration of impact scenarios in the numerical (FE) space.

3.2 Large pendulum apparatus

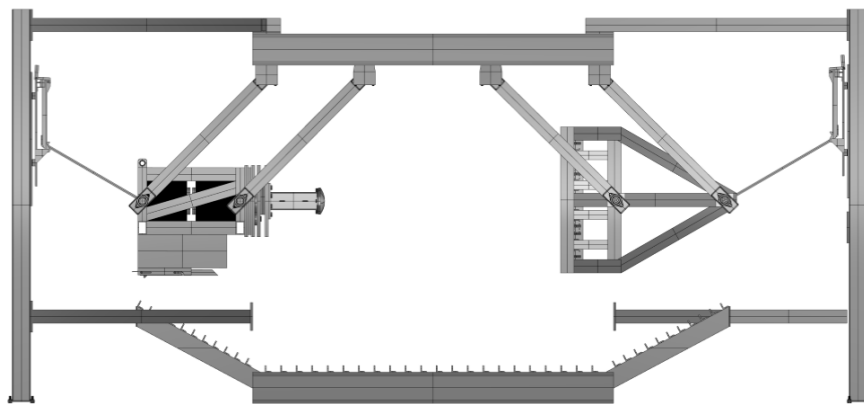


Figure 3-1. Schematic of the dual-pendulum impact apparatus



Figure 3-2. Photograph depicting a partial view of the dual-pendulum apparatus with smooth rigid indenter and grillage impact panel

The large pendulum apparatus, consisting of a dual pendulum design, was used for experimentation. A schematic of the intended design is illustrated in Figure 3-1, while a photograph showing the design as-fabricated is provided in Figure 3-2. The design is a more robust upgrade of the apparatus used in previous ice impact tests performed by Alam et al. (2012) as cited by Gagnon et al. (2015). Like the original design, the apparatus comprises two distinct mass groups set on arc paths of opposing sense. Each mass unit is supported by four rigid, parallel connections that act as swing arms for the mass or pendulum bob. Each swing arm is attached to the mass unit as well as the underside of the test frame top using a pillow-block bearing configuration. The connection method permits each mass unit to freely swing while maintaining its horizontal orientation relative to the other. The swing-arm connections reduce unwanted rotation out of the impact plane. Using the brake device and capture mechanism proposed by Gagnon et al. (2015), and observable as the saw-tooth configuration in the lower structure of the test frame of Figure 3-2 prevents

the pendulums from re-colliding. Consequently, measurements of the effect of individual impacts can be observed and recorded before being repeated using the same experimental test conditions.

Similar to the derivation discussed in section 2.10.3.2, when using a dual pendulum system, equation (21) through equation (29) can be re-arranged to express the impact velocity for each pendulum for any given angle of inclination as equation (28). For a dual pendulum, the two arms are lifted to equal angles of inclination from the vertical, with opposing senses. Thus, given that the impact velocity is independent of the mass of the pendulums, the relative impact velocity is twice the magnitude of that determined by equation (28). The corresponding impact energy, E , can be expressed as previously described by equation (29).

3.3 Grillage model



Figure 3-3. Experimental test grillage as fabricated

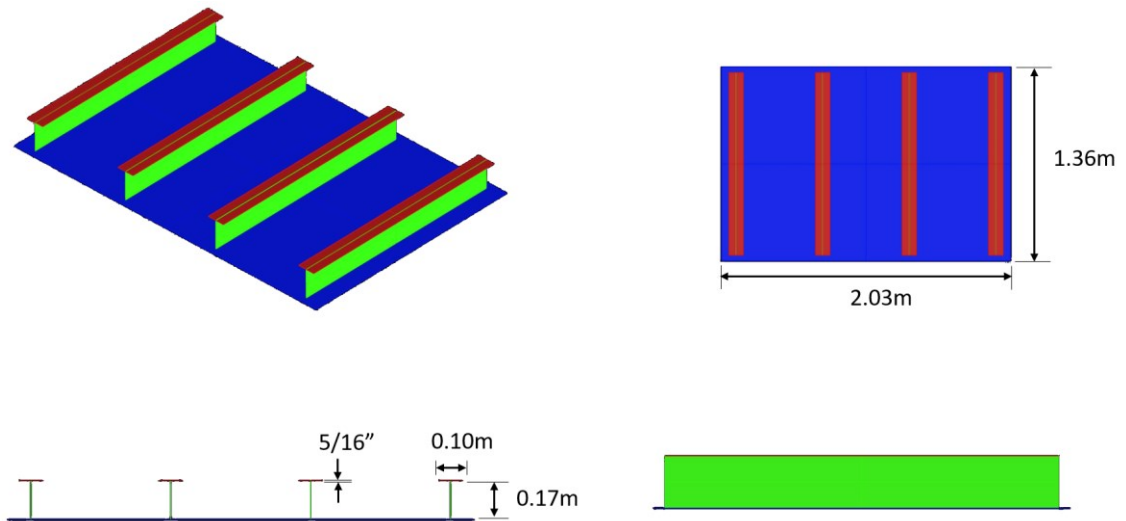


Figure 3-4. CAD grillage model as designed for numerical experimentation

The grillage model shown in Figure 3-3 is a representation of a pre-existing stiffened plate structure. The structure was built to resemble, but not necessarily subscribe to a sub-section of the side shell design taken from the port-side midship of HMCS IROQUOIS. The configuration shown in Figure 3-4 is a stiffened plate structure measuring 2.03 meters long and 1.36 meters wide. It is constructed entirely of a 5/16-inch mild steel plate with a nominal yield strength of 420 MPa and ultimate tensile strength of 510 MPa. The model as-built features four transverse T-shaped stiffeners that provide the primary stiffening for the side shell and are equally spaced across the longitudinal axis of the panel's aspect, at a spacing of 610 mm.

3.3.1 Structural components



Figure 3-5. HMCS IROQUOIS Tee-stiffener design (left) versus test grillage built-Tee stiffener (right)

The grillage model may be deconstructed into four primary components: the side shell, the transverse webs, the transverse flanges; and, the boundary conditions. While the original IROQUOIS-class panels that the specimen is modeled after featured a *British Standard* segmented I-Beam as the stiffening mechanism, the specimen undergoing experimentation was constructed using ‘built tees’ in which the frame and flange are separately cut and then fillet-welded together along their major axis to produce a notionally

similar T-stiffener. The distinguishing design differences are shown in Figure 3-5. The design facilitates the production of an experimental grillage and its associated numerical model by simplifying the number of material models and stock pieces necessary for reproduction.

3.4 Boundary conditions



Figure 3-6. Plate and stiffener boundary configuration

The boundary structure is not an authentic portion of the ship's structure. Instead, the boundary structure exists to provide extremely stiff boundary conditions for the plate edges, and the stiffener ends. The boundary conditions are designed as clamped boundary conditions, chosen to facilitate numerical modeling considerations as opposed to mimicking authentic shipside behavior. The boundary structure consists of a 24 mm thick steel plate welded to the edges of the side shell component with a 24 mm thick steel plate welded to longitudinal-axes ends of the stiffeners, as shown in Figure 3-6. Thus, the

grillages are not attached directly to the carriage tubing. The ring frame attaches to the tube (3/8" 4x6 tube along the top and bottom, and 5/16" 4x4 tube on the sides) such that when they are mated together, the plate perimeter bar and the ring frame form a steel ring.



Figure 3-7. Boundary condition installation in a pendulum frame

The boundary configurations are pre-drilled to permit attachment of the boundary frame to the 3/8-inch tubular steel frame of the pendulum arms via 1/4-inch, grade 8 bolts tensioned to a torque of approximately 150 lb-ft. as depicted in Figure 3-7. The bolt pattern restrains the plate against membrane forces.

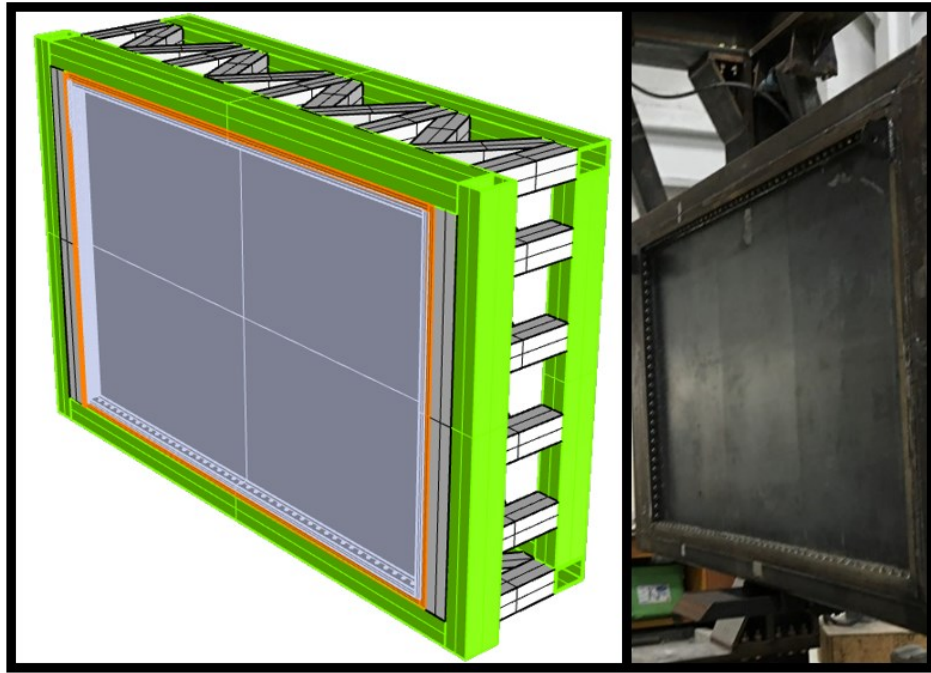


Figure 3-8. Ring frame panel restraint (left) depicts the method of restricting degrees of freedom upon impact. The panel installed with bolts is displayed for reference (right)

Transverse forces (impact forces) induced in the panel configuration are restrained directly by the ring frame around the panel periphery, as shown in Figure 3-8. Thus, the bolts are placed only in tension, while the ring frame restricts all other degrees of freedom (DOF)—surge (x -translation, heave (z -translation), roll (x -rotation), pitch (y -rotation), and yaw (z -rotation)). The steel test frame used to attach the grillage to the pendulum arms was sized and selected adequately, such that, it was not expected to experience plastic deformation during the impact experiments. Additionally, the plastic deformations anticipated in the model were expected to be so large that the elastic deformation of the test frame could be considered negligible. The panel is shown restrained by its boundaries in the pendulum frame in Figure 3-7.

3.5 Rigid indenter



Figure 3-9. Spherical, rigid indenter in its mounted configuration

The grillage impact full-scale experiment was completed using a spherical, rigid indenter as opposed to an ice cone or non-trivial rigid indenter. The rigid indenter was fabricated from HS-100 steel with a yield stress of 690 MPa and is shown in its mounted configuration in Figure 3-9. This design consideration renders the indenter adequately rigid compared to the panel-side indentation surface, ensuring maximum energy transference into the test specimen while simultaneously simplifying numerical modeling efforts, thereby reducing the sources of error in follow-on numerical experimentation.

3.6 Instrumentation

The instrumentation used for experimentation included digital inclinometers mounted to both pendulum arms, the FARO arm system for coordinate measurement, an HD video capture system operating at frame rates above 120 Hz, and standard hand measuring tools. It was initially envisioned to employ force transducers to validate data against, but the technology was not mounted and calibrated sufficiently within the absolute window of experimentation. Further repeated impact testing was planned across a number of test specimens with the inclusion of piezo-electric load washers to record impact forces. However, with the COVID-19 pandemic precluding the performance of these experiments, the primary data captured during experimentation was high-accuracy displacement data.

3.6.1 Faro System



Figure 3-10. FARO arm coordinate management representative level of detail. Note the capture of surface roughness due to pitting and distinction of paint layers

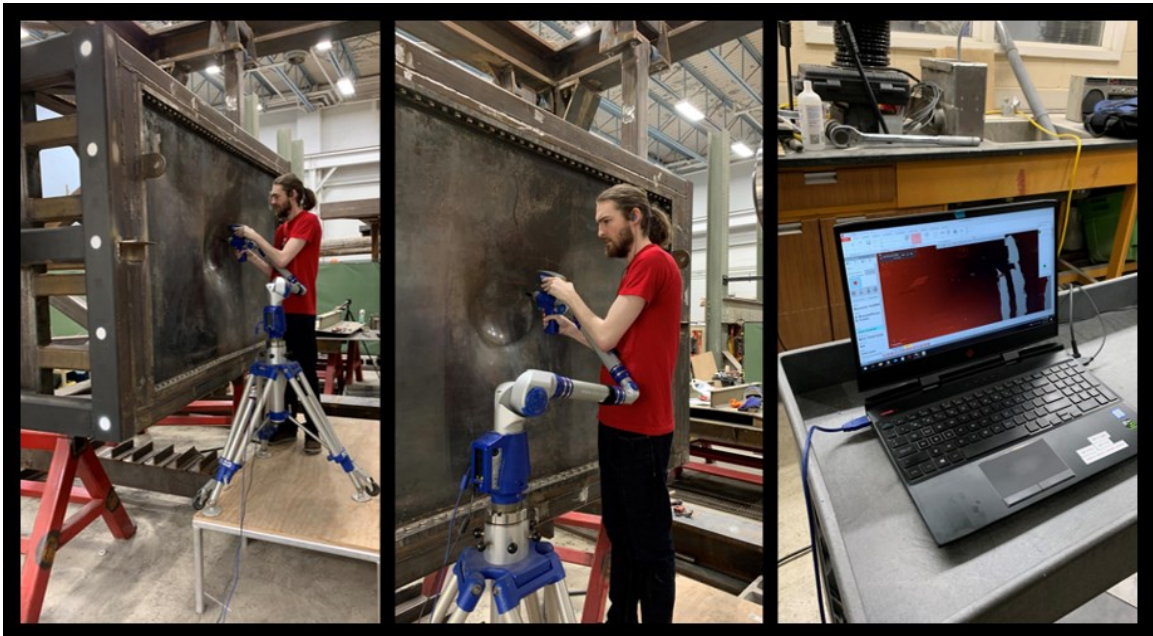


Figure 3-11. A composite image displays the Faro arm scanning process surface profile scanning (left), indentation crater capture (center), and digitized point cloud surface development (right)

The FARO Arm is a portable coordinate measuring machine (CMM). The device allows users to perform 3-D analysis and measurement using an optical laser for non-contact 3-D scanning. The level of fidelity is somewhat dependent on the surface refraction of the scanned item, but nominally permits distinctions on the order of thousandths of an inch. In pre-experimental testing, the device was routinely capable of identifying surface pits and paint flakes on the panel specimen. A representative scan of the panel, displaying the level of scan detail, is shown in Figure 3-10, while the in-situ scanning and transcription process is displayed in Figure 3-11.

3.6.2 Calibration

A platform for mounting the FARO scanner was constructed to create a consistent datum for measuring panel deformation with each impact. Markers were laid out in the laboratory denoting the position of the platform feet, and the position of the scanner and its orientation were scribed on the platform to ensure consistent placement. A structural feature featuring two orthogonal marks was scored in the lower-left corner of the pendulum frame. Given that the pendulum frame at this location was not anticipated to experience any permanent deformation, a common reference point across all scan data was established. Before each full-panel scan, this feature was scanned to set the orientation and coordinate system of the scan. Subsequently, consecutive scans could be overlaid by mapping this structural feature, permitting a detailed examination of the degree of deformation for any scanned region of interrogation.

3.7 Loading scenario

The grillage model was loaded on the outer side of its hull plating, i.e., the plate side vice the stiffener side of the panel. The effect was to load the panel as if the panel's outer side was the outside of a ship's hull experiencing an impact. The load was applied using the smooth, spherical indenter between the transverse frames at the vertical center of the panel. The spherical indenter was used because the rounded top softens stress concentrations that might arise with sharp-edged geometries (Zhu et al., 2018). The load was energy-based, established by using gravitational potential energy, consistently set by releasing the pendulums from a pre-determined impact angle of 50° . This angle was chosen for two reasons. First, in the newly upgraded pendulum frame, 50° was the maximum range

of the release mechanisms providing a valuable opportunity to run-in the pendulum. Second, the energy associated with a 50° strike was posited to be high enough to induce sufficient plasticity to prevent elastic shakedown within the first impacts without causing the instantaneous plastic collapse of the panel. Thus, multiple plasticity-inducing strikes would be observable in a single test sample.

Once the initial impact occurred, subsequent secondary impacts from rebound energy were prevented by the brake system. An interval of approximately 25 minutes minimum occurred between each strike. This interval was necessary for deformation scanning and recording, and system re-set. It had the secondary benefit of providing time for any residual vibration modes or heat energy developed in the collision to dissipate. The original load scenario intended to deliver impacts until any of the following results were delivered: 50 discrete impacts were imposed; shakedown in the structure was observed; or, the grillage ruptured. A deterioration of the test set-up, combined with unforeseen socio-political factors in the end months of 2019 and spring of 2020, prevented the test program from being completed, limiting the total panel loadings to four instances.

3.8 Experimental procedure



Figure 3-12. Pendulum arms raised to 50° and primed for experimental impact

The pendulum arms, previously adjusted via weight-block additions to have the same mass, were each drawn back to an angle of 50° from the vertical and locked into their respective release mechanisms, as shown in Figure 3-12. Once released, the two pendulum arms traced their arcs until intersecting at the bottom of their motion, allowing the smooth, spherical indenter to strike the plating at both a maximum speed as well as a horizontal orientation. After the initial impact, and once the rebound from the initial impact occurred, the brake system engaged, halting any further energy transfer into the panel. The scanner arm and its orientation platform were installed on the pendulum frame, and the indentation crater and surrounding panel structure were captured by CMM for later analysis. Photographs, video footage, and physical back-up measurements of the strike damage were taken, and the system was inspected for obvious visual cues indicating a catastrophic

failure of the structure. The test conditions were then re-set, and a subsequent round of testing commenced.

Table 3-1. Resultant contact velocities from pendulum arm inclination angles

Inclination angle [°]	Dual Pendulum closing speed [m/s]	Kinetic energy 1 carriage [kJ]	Kinetic energy 2 carriages [kJ]	Equivalent impact speed (1 moving carriage) [m/s]
5	0.386	0.235	.469	0.546
10	0.772	0.936	1.872	1.092
15	1.156	2.100	4.200	1.635
20	1.538	3.717	7.433	2.176
25	1.917	5.774	11.548	2.712
30	2.293	8.256	16.513	3.243
35	2.664	11.145	22.290	3.767
40	3.030	14.418	28.836	4.285
45	3.390	18.050	36.100	4.794
50	3.744	22.014	44.027	5.295

The resultant contact velocities associated with pendulum arm inclination angles are presented in Table 3-1. For any variety of inclination angles ranging from 0° to 50°, each pendulum may be independently set. The kinetic energy of each pendulum carriage at impact may be determined from energy methods previously described in section 2.10.3.2. The equivalent impact speed for a single moving carriage in a numerical environment is derived from a similar application of energy methods and is described in section 3.11.8.

3.9 Results

Four impacts were performed. The recorded deflections are presented in Table 3-2.

Table 3-2. Impact number (N) versus resultant experimental deflection (d) [cm]

Impact Number (-)	Incremental Permanent Deflection (cm)
1	9.01
2	2.76
3	1.09
4	1.01
Total Permanent Deflection	13.87



Figure 3-13. Grillage pre-impact depicting a mostly planar surface

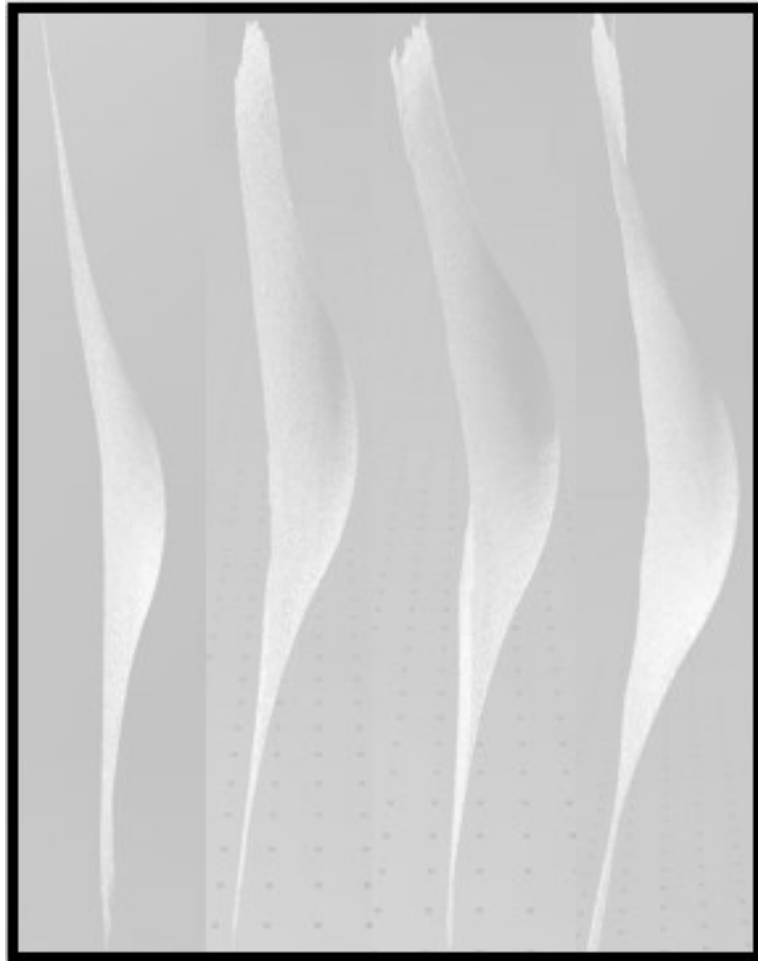


Figure 3-14. Profile view of FARO scans showing the qualitative scale of progressive deformation

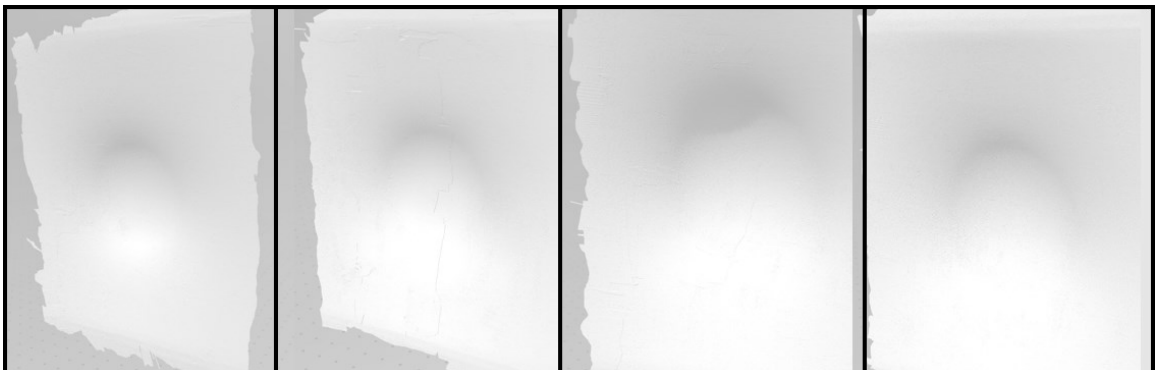


Figure 3-15. Normal view of FARO scans showing the qualitative scale of progressive deformation

The grillage, as was situated in the test frame, is displayed in Figure 3-13. Before impact, the grillage sat in a mostly planar configuration with no significant deformation discrepancies noticeable across the lateral face of the grillage. Following each impact, a progressive indentation crater, was observable with an increasing range of deformation radiating from a central contact point. The range of deformation is shown from a qualitative perspective depicting the FARO captures in both profile and normal views in Figure 3-14 and Figure 3-15, respectively.

3.9.1 First impact



Figure 3-16. Impact crater post-impact #1

After the initial impact, the maximum deflection recorded at the impact site was 9.01 cm. Through the examination of Figure 3-16, a characteristic spherical indentation emanating from the center of contact is apparent. Visual inspection of the surrounding plate

surface and stiffener configuration revealed that the impact was concentrated at the plate surface. There were no visual markers suggesting the elastic load capacity of the stiffeners was compromised.

3.9.2 Second impact



Figure 3-17. Impact crater post-impact #2

The recorded additional deflection after the second impact was 2.76 cm. The decrease in deflection was indicative that the grillage had experienced a hardening effect, and the range of elasticity of the plate was increased as a result of the initial impact. Visual indications of the impact included a deeper impact crater with the periphery of the crater expanded in all directions. The perimeter of the crater was slightly larger towards the stiffeners than in the vertical direction (i.e., the impact crater took on a very slight elliptical shape with the major axis oriented towards the stiffeners) as shown in Figure 3-17. There were still no visual indications that the plastic capacity of the stiffeners had been compromised.

3.9.3 Third impact

Immediately following the third impact, an additional 1.09 cm of deflection was noted in the deepest portion of the impact site. Moreover, the elliptical impact pattern became more pronounced. Bending was observed in the vertical and transverse axes of both stiffeners immediately adjacent to the impact site. By inspection, the bending was visually more significant to the left-hand inner stiffener than the right-hand inner stiffener when considered from a perspective oriented at the outer side of the plate as defined earlier.



Figure 3-18. An alternative view post-impact #3 illustrating impact depth

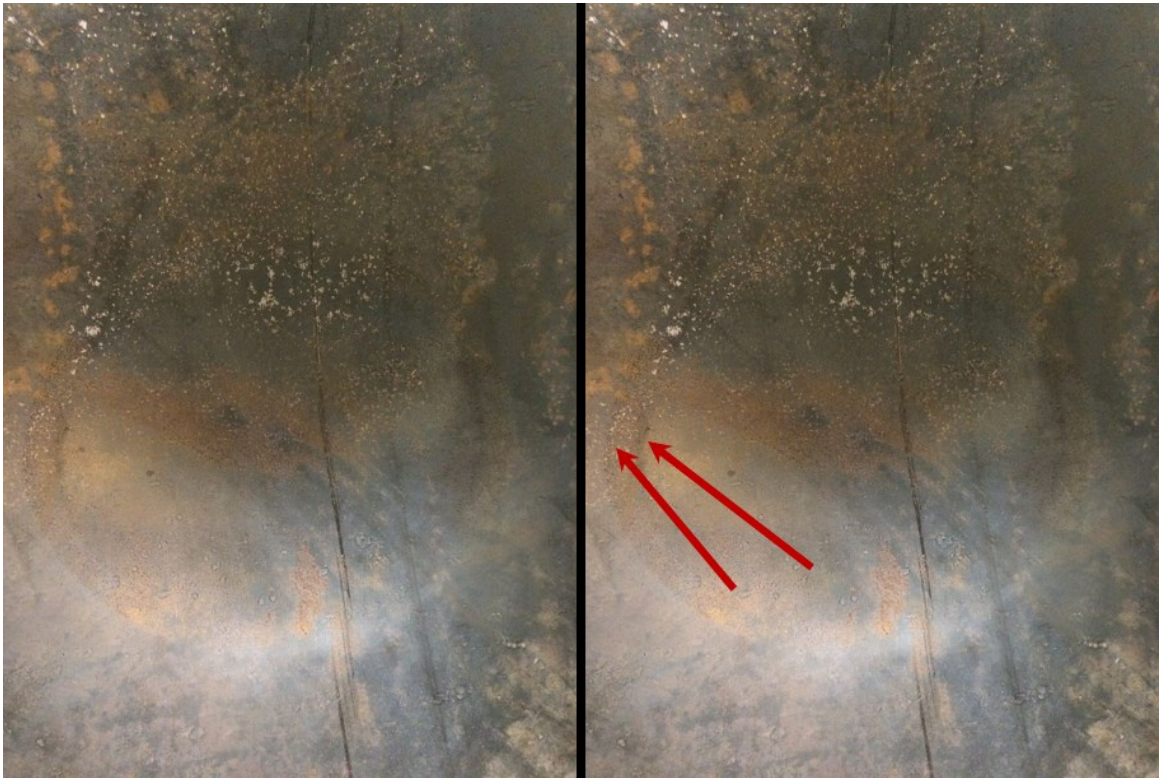


Figure 3-19. Impact crater post-impact #3 (left) with shadow indenter pattern indicated (right)

Viewed from the outer side of the grillage (Figure 3-18), stretching of the plate surface was visible such that the distinctly vertical orientation of the beam intersections with the plate were visible (i.e., an inspection of the outer side of the plate was sufficient for a lay-person to identify where the beams were installed behind the plate's surface). No visible signs of the plate, stiffener, or weld fracture were visible. Examination of the plate surface located between the inner and outer stiffeners showed no visible or tactile 'wave' effects, which would suggest the onset of plate buckling effects. Following the impact, the impact crater had preferentially drifted towards the left inner stiffener, as highlighted in Figure 3-19. It remains unclear whether the drift occurred due to idiosyncrasies of the

material and construction, or as a result of experimental error in the test set-up. The repercussions are discussed in detail in section 5.3.1.3.

3.9.4 Fourth impact



Figure 3-20. Grillage deflection post-impact #4. Circled regions denote a change in the curvature of the peripheral surface. Note the appearance of what appears to be shear buckling behavior



Figure 3-21. Plate inner side depicting the evolution of the impact crater between stiffeners and bowing of inner stiffeners



Figure 3-22. Profile view depicting stiffener plasticity effects post-impact #4

The fourth impact resulted in an additional 1.01 cm of deflection. Once again, the elliptical impact pattern became more pronounced as a third ‘edge’ to the crater was observed. Additional bending was noted in the vertical and transverse axes of both stiffeners immediately adjacent to the impact site, and the left-hand inner stiffener continued to experience more significant deflection than the right side. Plate stretching in the vicinity of the stiffeners became more pronounced. Additionally, a wave pattern began

to develop in the outer segments of the plate, viewable as the circled regions in the left-hand pane and top-right pane of the panel shown in Figure 3-20. At this point, no visible signs of the plate, stiffener, or weld fracture were visible. The degree of ingress of the indentation and the bowing of the stiffeners is shown in Figure 3-21, while the plasticity effects on the stiffeners are displayed in Figure 3-22.

3.9.5 Subsequent impacts

The four previously discussed impacts were applied to the panel in the Fall of 2019. Following the fourth impact, several cracked bearing housings were discovered in the test frame. The test program was put on hold while repairs were affected to the carriage. The potential influence of this discovery to the test program's observations is analyzed and discussed in section 5.3.1.3. In the Winter of 2020, five additional impacts were applied to the panel. After each impact, visual inspection alone provided evidence that the panel continued to exhibit increased deflection with each subsequent strike. Progressively increased plasticity was noted in the stiffeners, and the outer regions of the grillage continued to display the development of a wave-like effect across the plate with each impact. The pattern appears consistent with shear buckling behavior and is denoted by the circled regions of Figure 3-20. While the increased depth of the crater was not always evident by inspection, the overall crater dimensions continued to grow as the margins of the impact crater grew closer to the inner stiffeners.

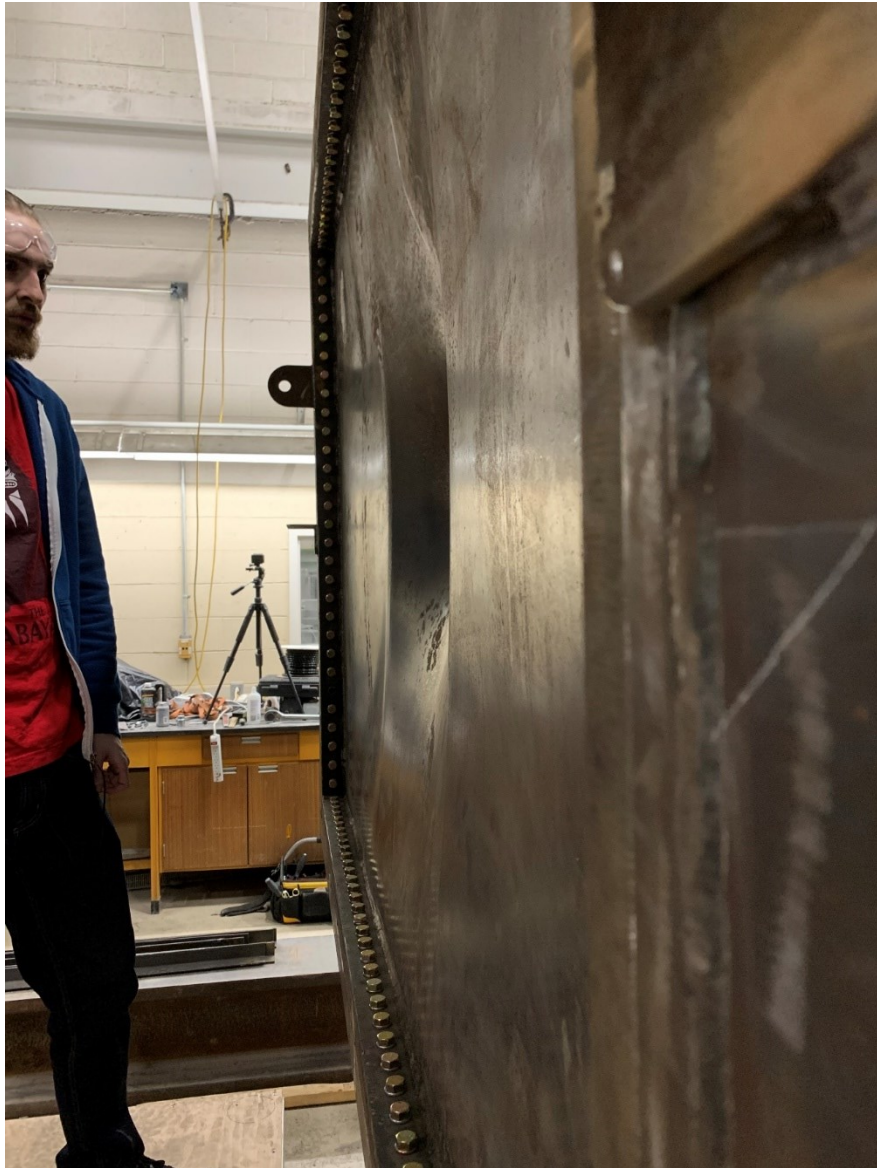


Figure 3-23. Panel condition post-impact #7



Figure 3-24. Corresponding galling material adhered to indenter surface (left) and magnified view (right)



Figure 3-25. Galling on bulk plate material (left) and magnified view of galled section (right)



Figure 3-26. Boundary condition plasticity. Note the bowing/wave developed in the lower plate boundary

In the central bay of the grillage, a sloped deflection extending from the test frame boundaries to the crater site became pronounced, as shown in Figure 3-23. Significantly, over this series of impacts, galling, a plate adhesion effect was noticed on the smooth, spherical indenter (Figure 3-24) as well as the plate (Figure 3-25). The transference behavior is indicative of plastic flow behavior in the plate (Johnson, 1989). While the post-impact data in this section provides a good qualitative description of the plate effects for comparison against numerical results, the plate deflection data was ultimately discarded when significant deformation was noted in the top and bottom of the test frame and boundary conditions as seen in the lower half of Figure 3-26.

3.10 Material Tensile Tests

A series of uniaxial material tests were performed to verify the material properties of the steel used in grillage construction. The tensile test coupons were created from scrap steel from the same plate used in construction. Using leftover steel from initial construction ensures that the test coupons are not unduly influenced by residual stresses that might remain if the coupons were cut from steel used in the experimental loading.

3.10.1 Tensile Specimen Specifications



Figure 3-27. Tensile test coupons

Table 3-3. Material coupon dimensions

Coupon	Gauge length (mm)	Gauge width (mm)	Gauge depth (mm)
1	62.99	12.42	7.97
2	63.44	12.41	7.97
3	60	12.42	7.96

Three coupons were machined and tested in accordance with ISO specifications 7500-1, 9513, and 6892-1:2019 for monotonic tensile testing of metallic materials. The actual physical specimens are shown in Figure 3-27. The overall dimensions of the coupons are given in Table 3-3.

3.10.2 Instrumentation and apparatus



Figure 3-28. Instron 5585-H tensile test apparatus

The tensile tests were carried out using the Instron 5585-H tensile test apparatus shown in Figure 3-28. Model 5585-H has a capacity of 250 kN, with a speed range of 0.001-500 mm/min, and a test area of 1256 mm by 575 mm.



Figure 3-29. Externally-mounted extensometer

The mechanical apparatus is computer-controlled while data is simultaneously collected using Instron's *Bluehill 2* software. Load data was collected using instrumentation incorporated into the Instron apparatus, while displacement and strain data were recorded using an externally mounted extensometer shown in Figure 3-29.

3.10.3 Results

The output of each uniaxial tensile test produces an engineering stress-strain plot, which provides, at minimum, the engineering yield stress ($\sigma_{0\text{eng}}$), the Young's modulus (E), the engineering ultimate tensile stress (UTS), and the engineering failure strain (ϵ_{fail}). The results of each tensile test are presented in section 3.10.3.1 through section 3.10.3.3 and summarized in section 3.10.3.4.

3.10.3.1 Specimen 1

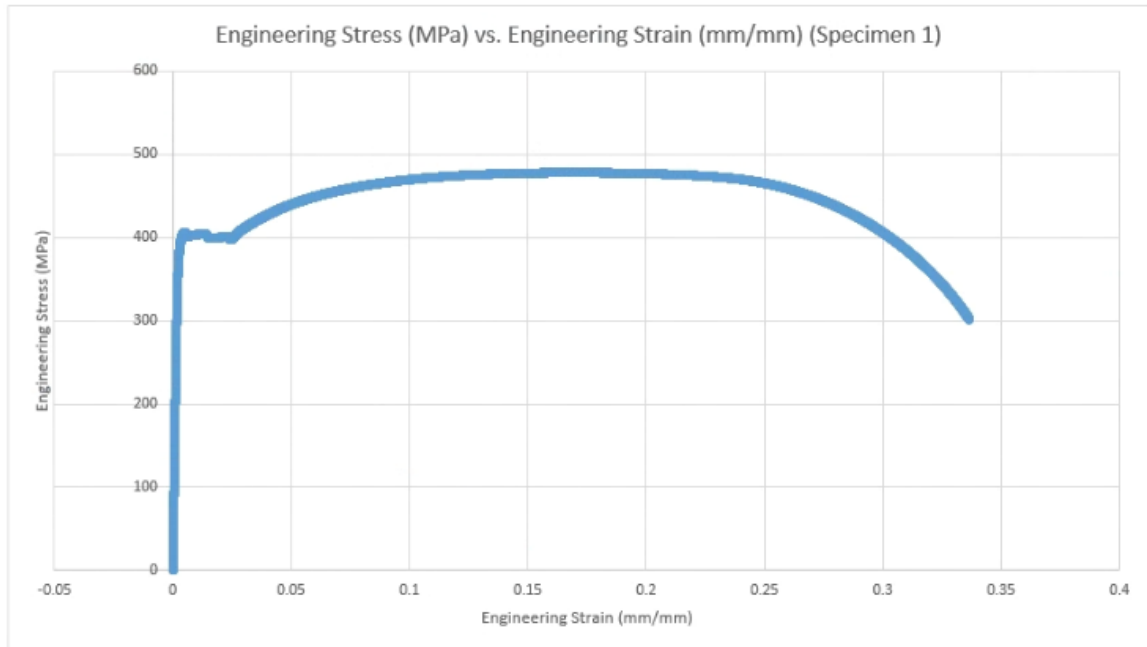


Figure 3-30. Stress-strain plot for uniaxial tensile test coupon #1

Table 3-4. Material properties for uniaxial tensile test coupon #1

Engineering Yield Stress (MPa)	Engineering Ultimate Tensile Stress (MPa)	Engineering Failure Strain (mm/mm)
406	478	0.34

The engineering stress-strain plot for this specimen is displayed in Figure 3-30. It was apparent from the initial analysis that the test specimen slipped in the grips of the test apparatus or was not mounted perfectly perpendicularly to the direction of the force application. ASM informs testers that uniaxial tensile tests are susceptible to coupon placement errors and the resultant force vectors during the elastic portion of extension (*ASM International*, 2020). The questionable data was discarded, and in subsequent analysis, an industry-validated Young's Modulus of 207 GPa will be used. The plastic material properties of note are tabulated in Table 3-4.

3.10.3.2 Specimen 2

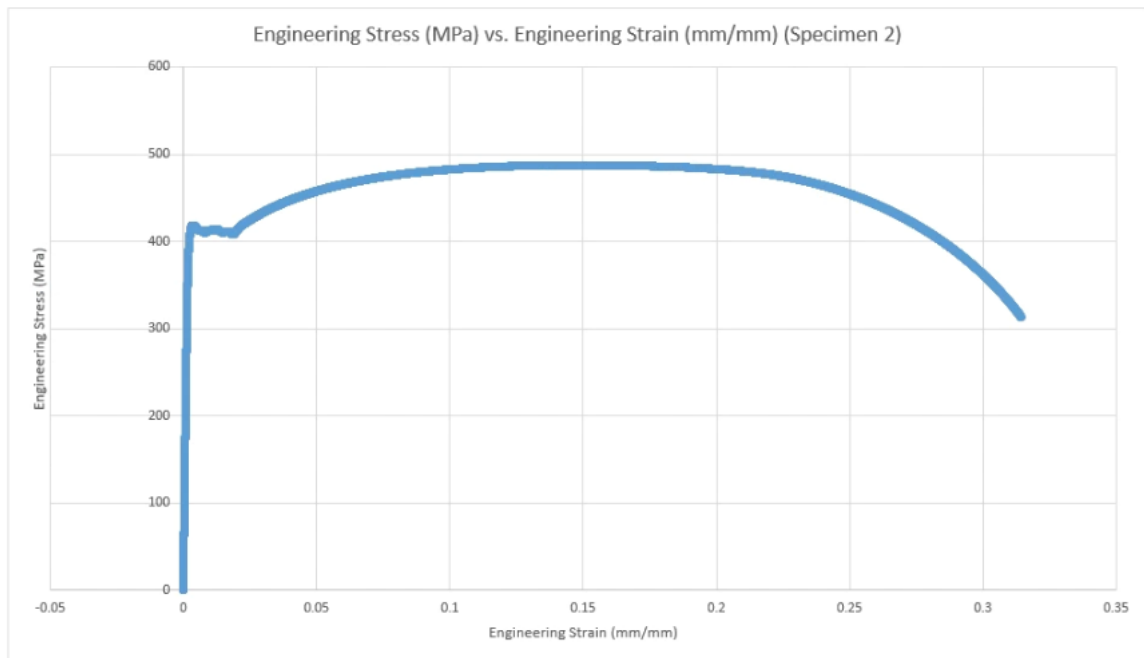


Figure 3-31. Stress-strain plot for uniaxial tensile test coupon #2

Table 3-5. Material properties for uniaxial tensile test coupon #2

Engineering Yield Stress (MPa)	Engineering Ultimate Tensile Stress (MPa)	Engineering Failure Strain (mm/mm)
418	488	0.31

The engineering stress-strain plot for this specimen is displayed in Figure 3-31. It was apparent from the initial analysis that the test specimen slipped in the grips of the test apparatus or was not mounted perfectly perpendicularly to the direction of the force application. As per specimen 1, the bad data was ignored, and in subsequent analysis, an industry-validated Young's Modulus of 207 GPa will be used. The plastic material properties of note are presented in Table 3-5.

3.10.3.3 Specimen 3

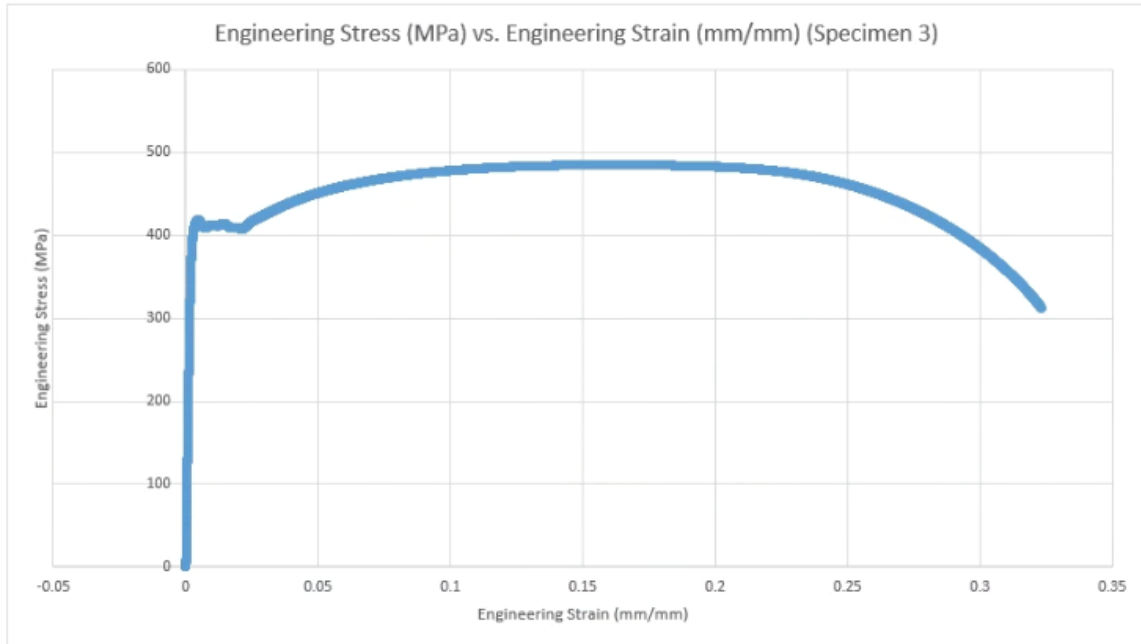


Figure 3-32. Stress-strain plot for uniaxial tensile test coupon #3

Table 3-6. Material properties for uniaxial tensile test coupon #3

Engineering Yield Stress (MPa)	Engineering Ultimate Tensile Stress (MPa)	Engineering Failure Strain (mm/mm)
418	485	0.32

The engineering stress-strain plot for this specimen is displayed in Figure 3-32. It was apparent from the initial analysis that the test specimen slipped in the grips of the test apparatus or was not mounted perfectly perpendicularly to the direction of the force application. In subsequent analysis, an industry-validated Young's Modulus of 207 GPa will be used. The plastic material properties of note are displayed in Table 3-6.

3.10.3.4 Material property tensile test summary

Table 3-7. Material property summary for uniaxial tensile test coupons

Specimen	Engineering Yield Stress (MPa)	Engineering Ultimate Tensile Stress (MPa)	Engineering Failure Strain (mm/mm)
1	406	478	0.34
2	418	488	0.31
3	418	485	0.32
Average	414	483.7	0.323

Table 3-7 summarizes the captured material properties for the uniaxial tensile test specimens of the material used in grillage fabrication. The procured material was identified as a 350MPa (44/500W) yield steel. Mill tensile tests reported 420 MPa as the actual yield value. The in-house tensile tests presented here suggest the material behaves at a much higher value than the steel grade itself. However, the results are nominally similar to but slightly softer than the value of 420MPa reported by the mill. The material certificate is provided in Appendix A.

3.11 Numerical model

The numerical model developed in this section is used for the multi-indenter experimental range of analyses presented in Chapter 4. The model is a confluence of best practices from literature, advice from more experienced modelers, acquired experience, and cyclic revision of the model. Several revisions were made based on growing knowledge derived from the discussed sources until the model provided a sufficiently reasonable presentation of impact behavior consistent with the real-space behavior observed in the full-scale laboratory validation experiment.

3.11.1 Methodology

The behavior of the physical phenomena in impact scenarios is highly dependent upon the domain of the system. For many types of impact involving a variety of simple indenter shapes and simplified contact scenarios, analytical solutions have been proposed and investigated beginning with Hertz (1882) through modern expansions and amplifications of the solutions by Johnson (1982). When the geometry or domain becomes increasingly complex and involves complicated initial conditions and boundary configurations, impact problems become extremely difficult to solve with an analytical approach (Johnson, 1989). As a result, in engineering practice, problems of this nature are often solved via numerical methods. Using a domain discretization scheme, such as explicit non-linear FEM, is an appropriate tool for simulating and studying the accumulation of plastic damage (Liu & Quek, 2013; Quinton et al., 2017).

Numerical simulation of the collision was conducted using LS-DYNA. LS DYNA is a well-known and highly regarded FEA code developed by Livermore Software Technology Corporation for general-purpose simulations of a wide variety of problems (LSTC, 2019). The decision was based on the author's experience with the software and access to the solver facilitated through a license provided by Memorial University of Newfoundland. LS DYNA is an explicit nonlinear finite element code which has the ability to model accumulated damage via the modeling of nonlinear geometry and nonlinear material. Moreover, the code has the capability to detect contact between bodies. Liu and Quek (2013) broadly summarize the procedure of FEM computational modeling as:

- Geometry modeling

- Domain discretization (meshing)
- Material property assignment
- Boundary, initial, and loading condition determination
- Solution control assignment
- Model validation and revision (as necessary)

3.11.2 Structural model

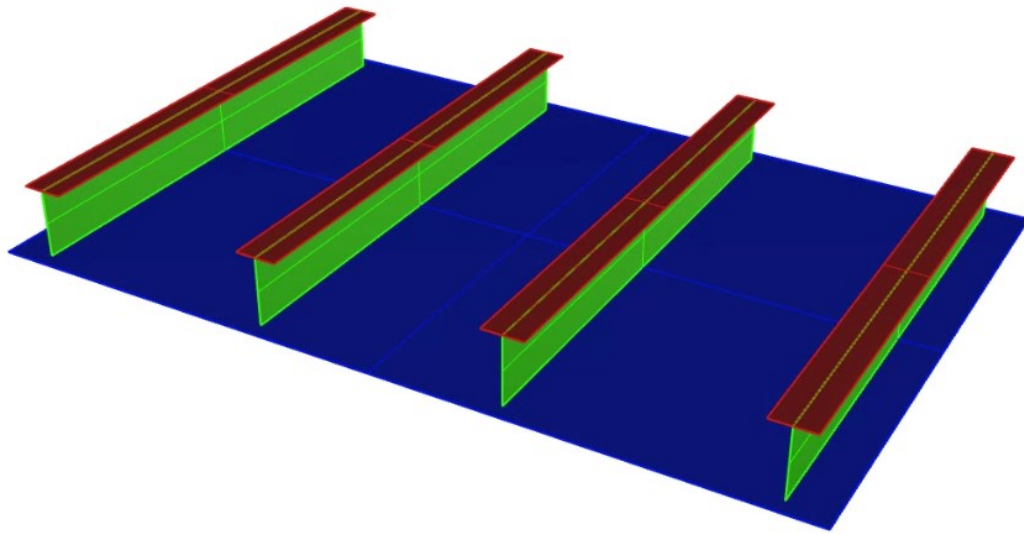


Figure 3-33. Grillage model geometry depicting surface areas

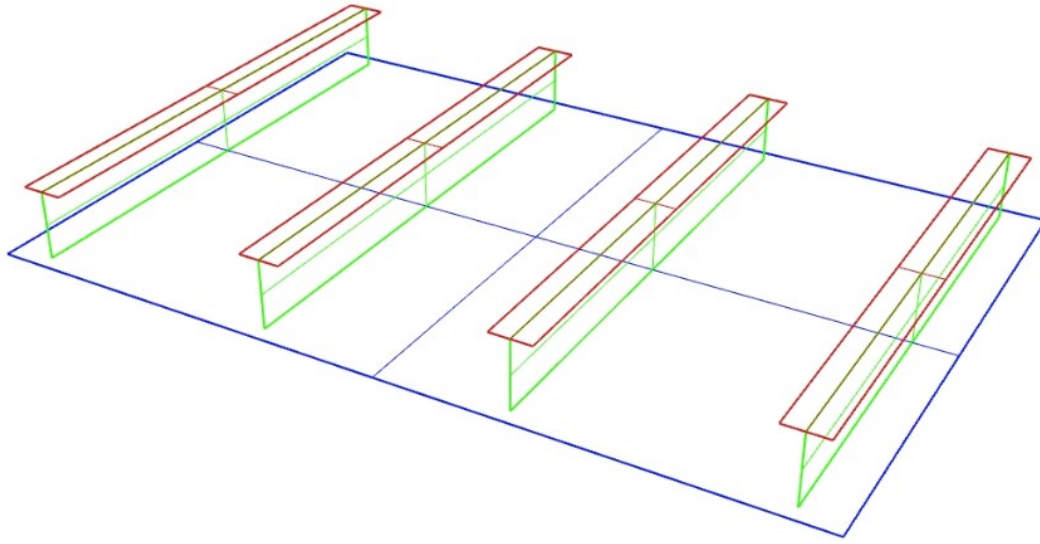


Figure 3-34. Grillage model geometry depicting design curves

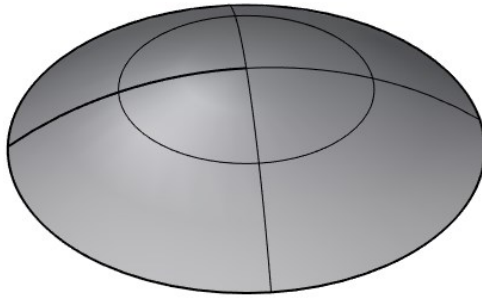


Figure 3-35. Indenter model geometry

The base geometry for all parts utilized in the FE model was developed by constructing a series of curves and converting the curves to planar surfaces in *Robert McNeel & Associates'* general-purpose CAD modeling software, *Rhinoceros 5*, as seen in Figure 3-33, Figure 3-34, and Figure 3-35 (McNeel, 2019). The resultant FE model comprises six sets of parts. The model dimensions mirror the real-space design of the stiffened grillage structure under investigation in the experimental laboratory set-up.

3.11.3 Finite element mesh definition

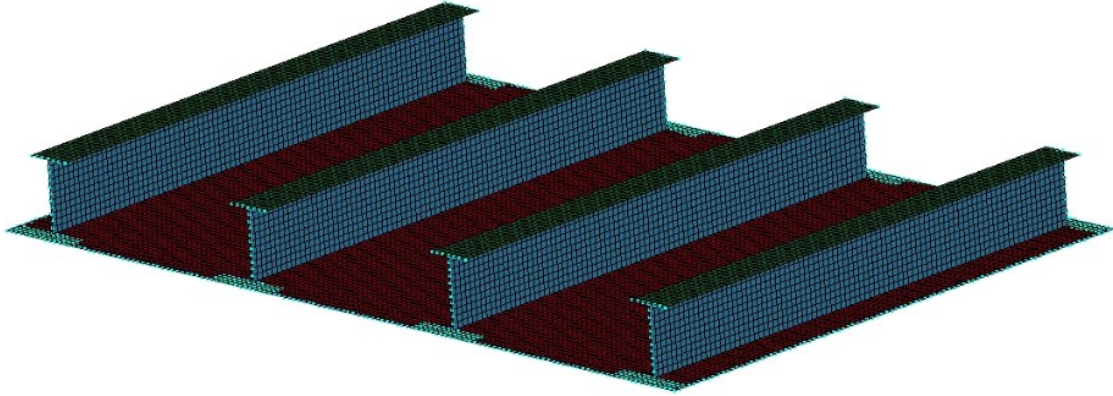


Figure 3-36. A stiffened panel structure meshed with quadrilateral elements

The geometric model is overlaid with appropriate finite elements creating a continuous mesh—a collection of nodes and elements which relate interactively based on the element parameters and mesh density, as seen in Figure 3-36. If the problem has been appropriately discretized, many of the 3-D elements in real-space can be approximated with a lower dimension, and the solution to each element can be approximated using more straightforward polynomial functions before the solutions are aggregated to form the solution of the entire domain (Liu & Quek, 2013). Several parameters are required to define an element, including: element type; element formulation; the number of through-thickness integration points; shear factor; and, element thickness.

3.11.4 Element selection

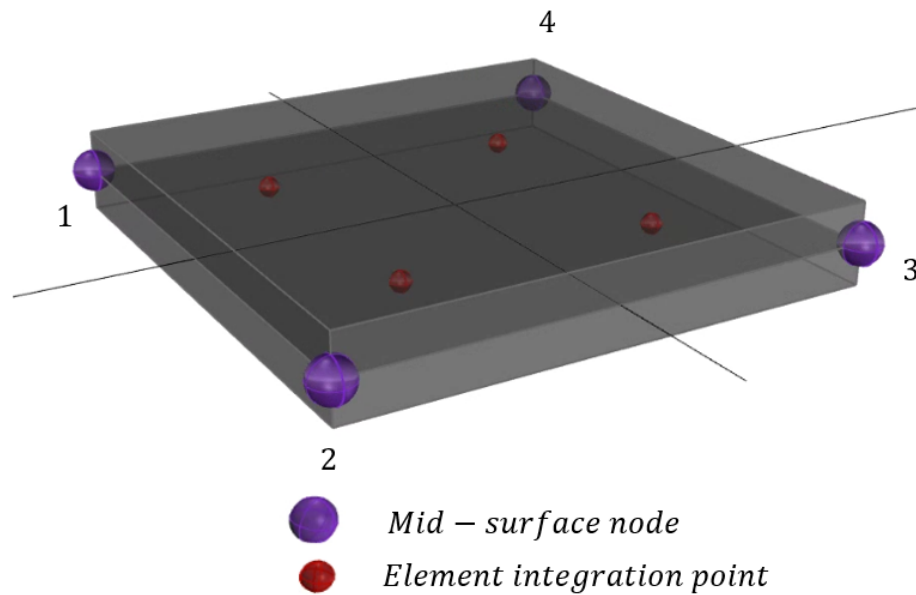


Figure 3-37. 4-node shell element geometry

The side shell, as well as the plate stiffeners—both flanges and webs—are appropriately modeled using shell elements. A representative graphic showing the orientation and constituents of a 4-node shell element is provided in Figure 3-37. Quinton et al. (2017) advise that when modeling geometry, which has one dimension that is significantly less than the other two dimensions, shell elements can be used to model the structure efficiently. LS Dyna’s default shell element, the Belytschko-Tsay element, is a 4-node planar element permitting six degrees of freedom in all four nodes. The element can model bending and membrane forces and may be loaded both in-plane and normal to its surface. While the aspect ratio of the element is discretely identified by user-defined geometry in an infinitely thin surface, the shell thickness uses parameterized space as a property of the element.

Quinton et al. (2017) assert that non-linear FEA hull modeling in combination with areas of interest which will exhibit highly non-linear behavior, avoid the use of solid or beam elements and use shell elements solely. The physics and design of this element lend itself easily to the shell plating and stiffener components. The shell element is the obvious model for such a design when compared with solid or beam elements provided that a sufficient number of shell elements are used so that geometric curvature or out-of-plane behavior can be captured.

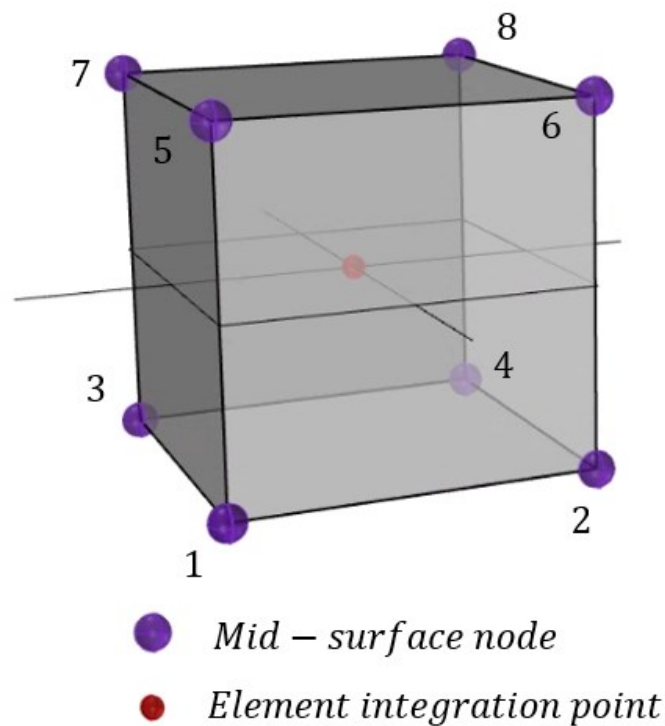


Figure 3-38. 8-node solid (brick) element geometry

The smooth, rigid indenter was modeled using 8-node solid (brick) elements. A representative graphic showing the orientation and constituents of an 8-node solid element is provided in Figure 3-38. Solid elements exhibit three translational degrees of freedom

and zero rotational degrees of freedom. The elements may be loaded normally to each face's surface or at each node. In this application, the solid elements were assigned a rigid property. Rigid solid elements do not have any nodal DOF and cannot respond to any load as a property of their rigidity. The experimental indenter was designed with robust dimensions and material properties such that it was not expected to experience plastic deformation. Moreover, the grillage structure was anticipated to experience significant plastic deformation relative to any elastic deformation of the indenter. Under this assumption, the elastic deformation of the indenter was considered negligible, and the decision was made to model the indenter as rigid.

3.11.5 Element formulation

As previously touched on in section 3.7, the grillage structure was anticipated to experience considerable multi-axial non-linear deformations composed of a combination of plate bending, membrane effects, material thinning, and possible shear effects. Consequently, the numerical model required element formulations capable of reflecting and capturing these behaviors. Hallquist, (2006) recommends the Belytschko-Tsay (BT) formulation for most structural applications in part due to its computational efficiency when compared to the Hughes-Liu (HL) element.

The plate and stiffener geometries mesh with 4-node BT shell elements. The BT element is computationally efficient and the default shell element formulation of LS-DYNA. Alsos & Amdahl (2007) propose an element length-to-thickness ratio between 5-10 to appropriately represent local stress and strain effects. The final mesh used for this analysis resulted in shell ratios that all fell within this recommended range. The rigid

indenter was modeled with default constant stress solid elements. The part was treated as a rigid body. The definition of rigid elements is made through the elements' material model, not the elements' formulation. The distinction makes the choice of element formulation trivial to the simulation results, but alternative formulations may have affected solution run times.

3.11.5.1 Number of through-thickness integration points

The effect of the induced force needs to be examined at various points through the thickness of the element to calculate the effect of moments or in-plane forces on elements. Quinton et al. (2017) propose that a best practice for non-linear materials is the use of four or five through-thickness integration points. Given that shell stress is calculated at the integration points, not the element surface, the use of a sufficient number of integration points ensures that the difference in stress between the surface and the outermost integration points is small enough to be considered equivalent. Five integration points were used to define the shell elements in this study. Hallquist (2006) supports the adoption of this practice noting that in choosing four or five integration points through the thickness, the common procedure is to ignore the difference (error) between the surface and outermost integration points. The location of the integration points through-thickness follows a distribution consistent with Gaussian quadrature.

3.11.5.2 Shear factor

A shear correction factor of 5/6ths was employed in the element definition. The shear correction factor is an attempt to correct for the shell formulation's incorrect assumption that transverse shear stress is constant through the element as opposed to

parabolically distributed. The shell formulation selected in LS-DYNA is based on a first-order shear deformation theory from the Reissner-Mindlin plate theory. Thus, the element yields constant transverse shear strains on the top and bottom surfaces of the shell. To compensate, LSTC recommends a correction factor of $5/6$ be applied to the element definition for isotropic materials such as steel (Hallquist, 2006). The correction's validity holds in this instance, but it is important to note that this shear correction factor is only appropriate to applications where the shell element has a rectangular cross-section.

3.11.6 Element thickness

The element thickness is a parameterized value assigned to individual parts composed of shell elements within the model. Subsequently, each part's shells have a thickness assigned consistent with the dimensional thickness of the stiffened panel constructed for laboratory experimentation, nominally $5/16$ -inch.

3.11.7 Model mesh

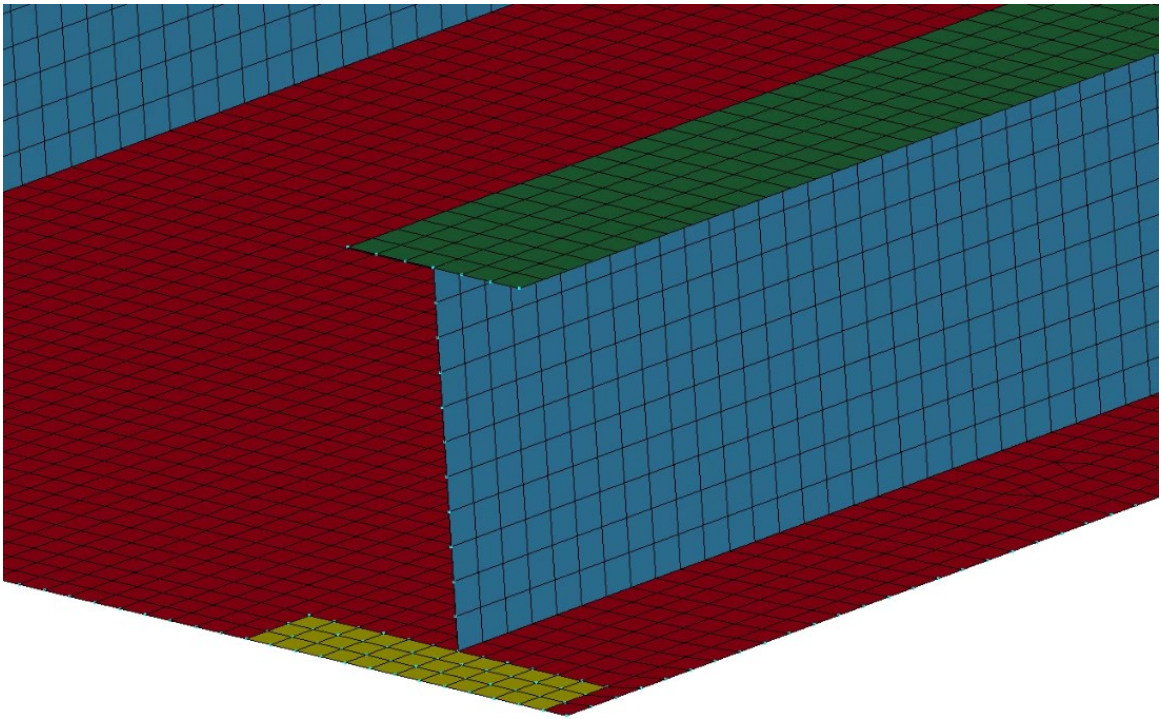


Figure 3-39. Quadrilateral mesh of a stiffened panel structure

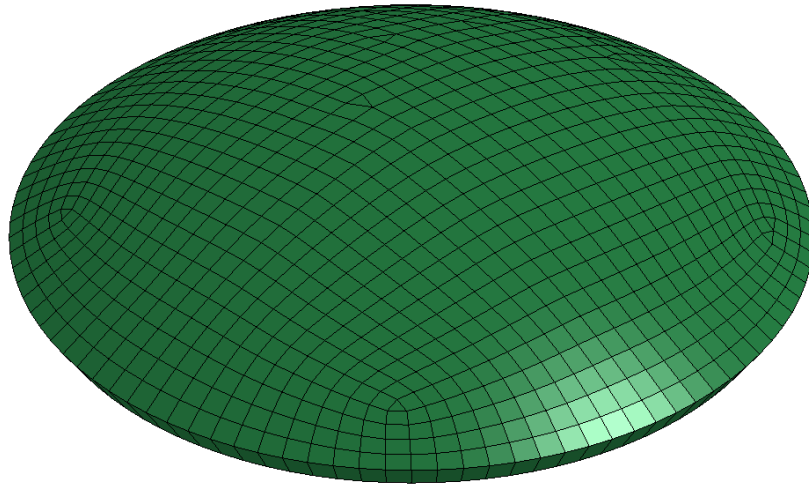


Figure 3-40. Smooth, spherical rigid indenter mesh

The geometric model (Figure 3-33) was meshed entirely with 4-node quadrilateral shell elements using *Altair HyperMesh*. Based on the discussion provided by Liu and Quek

(2013), and the best practices proposed by Quinton et al. (2017), the mesh was created exclusively from quadrilateral elements to avoid using degenerate triangular elements in nonlinear structural analysis of regions with a high-stress gradient. The resulting plate configuration mesh, as well as the indenter mesh, are depicted in Figure 3-39 and Figure 3-40, respectively.

3.11.7.1 Mesh quality

The basis CAD geometry used in this analysis was drafted precisely for the project. As such, preliminary housekeeping items such as the removal of unnecessary curves; a sufficiently low absolute tolerance; and, standard meter, kilogram, seconds (mks) units were used to facilitate a smooth transition and minimize potential parametric input errors into LS-DYNA. Applying these principles ensured little CAD repair or alteration was required to achieve a continuous and quality mesh. The mesh was trimmed using self-intersecting surfaces in *Hypermesh*, and duplicate nodes were investigated and removed as necessary. Visual inspection of the final model mesh shows a continuous mesh, with smooth transitions and quadrilateral elements.

Table 3-8. Model mesh quality assessment

Quality	Allowable	Min. value	Max. value	#Violated(%)
Aspect Ratio	5:1	1.01	1.46	0(0%)
Jacobian	0.6	0.7974	1	0(0%)
Skew	45	0	25.9	0(0%)
Warpage	10	0	0	0(0%)

In regions of geometry changes, some triangular elements were noted, but the overall contribution of triangular elements was low. Elemental aspect ratios, warpage value, Jacobian, and skew values were assessed against best practice values advised by Quinton (personal communication, 2018). Upon review of the results, no elements were found to have Aspect Ratios, Jacobian values, Skew, or Warpage outside of the desired parameters. LS-DYNA's model checking function was used to assess model quality; the numeric results of the quality assessment are presented in Table 3-8.

3.11.7.2 Mesh convergence study

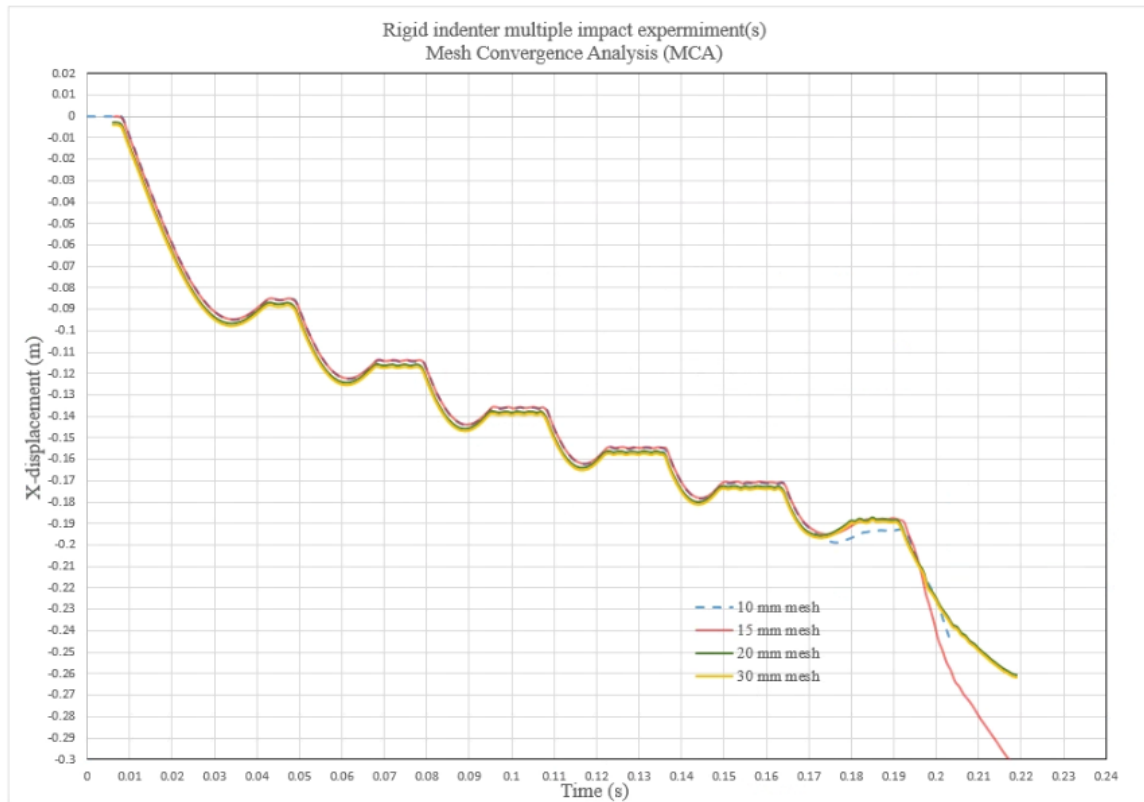


Figure 3-41. Mesh convergence analysis indicating convergence at 15 mm

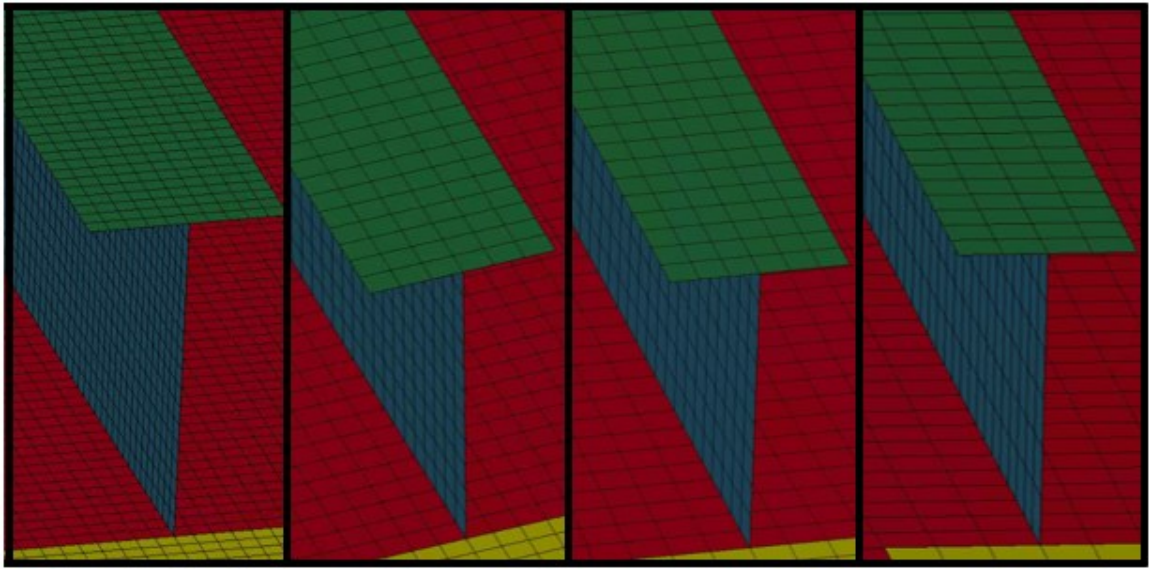


Figure 3-42. Side-by-side mesh density comparison

A mesh convergence study was conducted to ensure that the resultant stresses and displacements were independent of further refinements in the mesh size. The h-method (element size variation) was used to perform the analysis. As can be seen in Figure 3-41, mesh convergence (non-varying behavior with increasing mesh density) was achieved at an element size of 15 mm. The close (overlapping) correlation of the displacement pattern between the 10 mm and 15 mm plots as compared with the plots of the larger meshes is a classic indication of convergence behavior. Subsequently, for efficiency, the 15 mm mesh—which is less dense than that comprised of 10 mm elements—was selected because the convergence analysis demonstrates that mesh refinements beyond 15 mm were unnecessary and would serve to add increased computational costs to the analysis. A selection of the mesh densities is presented side-by-side for relative comparison in Figure 3-42. The mesh details used in the convergence study are summarized in Table 3-9.

Table 3-9. Mesh convergence details

Mesh	Element Size (mm)	Number of Shell Elements	Mesh Density (element/m ²)
1	10	41432	10000
2	15	18456	4444
3	20	10640	2500
4	30	4780	1111

A less dense mesh was selected for the indenter (slave surface) than the final mesh of the grillage (master surface) to align with Hallquist's (2006) recommended practice. Incorporating such a mesh-density relationship helps ensure that the contact algorithm does not allow master nodes to penetrate the slave surface. Within the scope of this study, the slave surface is assigned rigid material properties. Consequently, a mesh converge analysis for the slave surface is unnecessary as the indenter's stress behavior is not in consideration. When treated as a rigid material, the indenter's material behavior renders no interactive effect on the contact of the test grillage.

3.11.8 Load scenario

The initial load scenario applied to the grillage was analogous to the loads applied in section 3.7. The experimental load was used as a real-world validation against the design of the numerical model material parameters and boundaries. The scenario featured the indenter part and grillage parts contacting at equal velocities with opposing senses. The velocity of each component was set at 3.77 m/s, the same velocity observed in a free swing of each pendulum arm from a vertical inclination angle of 50° under controlled conditions. Once a level of confidence was achieved concerning the operation of the numerical model parameters, the process was repeated employing a simplified model that uses a stationary

grillage structure with a moving indenter assigned an equivalent closing velocity, and thus equivalent energy magnitude. The concept was informed by research initially conducted by Gagnon et al. (2015) and calculated preliminarily by Quinton (personal communication, 2020).

Beginning with a known pendulum inclination as determined using equation (28), the total kinetic energy of a two-body impact can be described by equation (29). The total kinetic energy in the experimental or real-world system can then be equated to the numerical system according to equation (31), where m_{sc1} , m_{sc2} , v_{sc1} , and v_{sc2} refer to the masses and velocities of the two simulated (numerical) carriage models, respectively.

$$KE_{Total} = \frac{1}{2}m_{sc1}v_{sc1}^2 + \frac{1}{2}m_{sc2}v_{sc2}^2 \quad [31]$$

Recognizing that the second carriage is constrained (fixed) in the numerical environment, the velocity associated with the second term in equation (31) is zero, and the equation may be reduced and re-written as equation (32).

$$2KE_{Total} = m_{sc1}v_{sc1}^2 \quad [32]$$

With this simplification, the equivalent velocity a single moving carriage would need to achieve to equal the energy state of two opposing non-stationary carriages can now be determined as a function of the total kinetic energy of a two-body collision, and the mass of the proposed carriage, as provided in equation (33).

$$v_{sc1} = \sqrt{\frac{2KE_{Total}}{m_{sc1}}} \quad [33]$$

The numerical model utilized a variety of identified, known inputs to yield a demonstrable outcome in the numerical environment consistent with the real-world observation of the response of the structure. With the initial design complete, several load scenarios were developed to explore the problem space and assess impact behavior. The scenarios were based on the common motif of a 50 impact (or less) run of discrete impacts with progressively more developed variations on the indenter behavior.

3.11.8.1 Load scenario 1

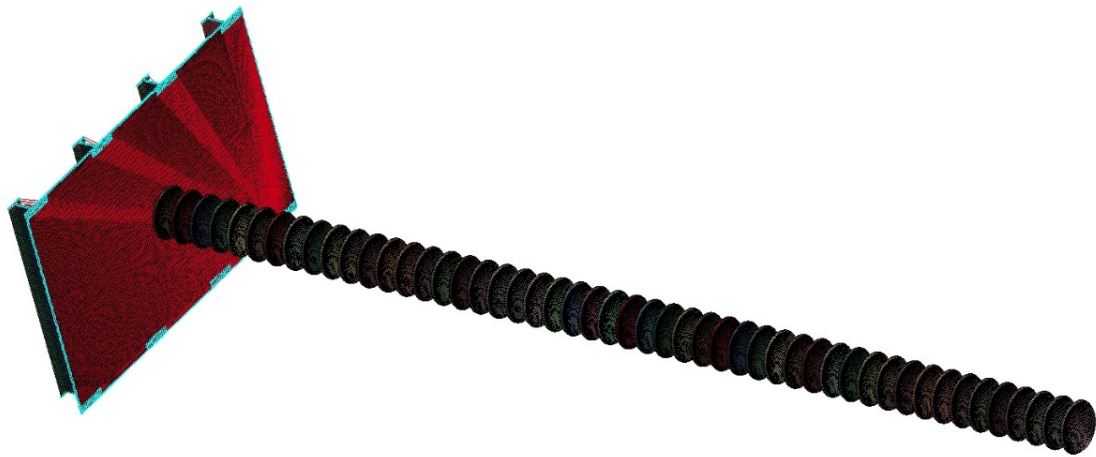


Figure 3-43. Load case #1: Co-incident indenter strike

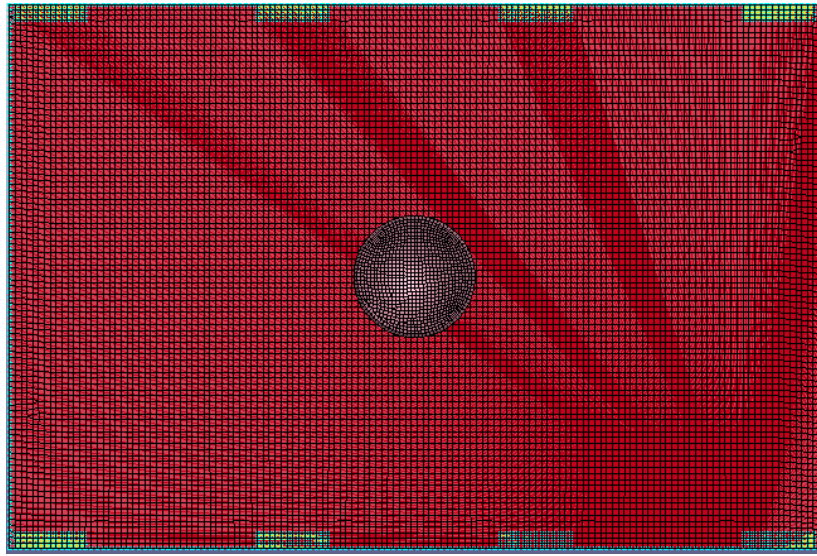


Figure 3-44. Load case #1: Impact pattern

The first load case considered investigates a coincident repeating impact centralized vertically and horizontally between transverse stiffeners, as illustrated in Figure 3-43. A total of 50 impacts are applied to the panel in each instance (excepting when less than 50 strikes may be required to induce rupture in the panel). The total strike energy of each impact ranges from ~ 0.469 kJ to ~ 44 kJ, corresponding to an associated relative velocity of 0.546 m/s to 5.295 m/s, depending on the simulated impact angle.

3.11.8.2 Load scenario 2



Figure 3-45. Load case #2: Clock-pattern strike

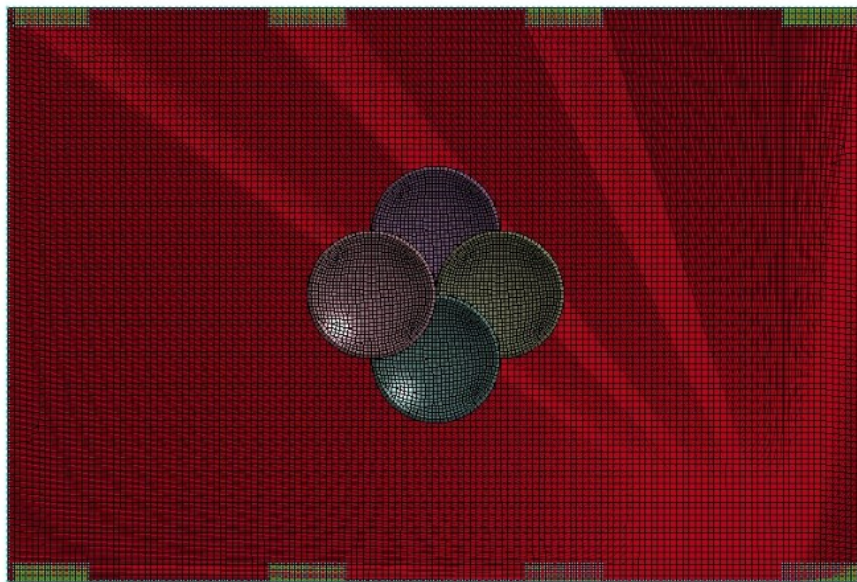


Figure 3-46. Load case #2: Impact pattern

Load scenario two introduces a repeating pattern of adjacent impacts. The pattern begins with a centralized strike centered vertically and horizontally between the two central stiffeners. The indenters are then applied orthogonally in a clockwise pattern at distances of one-half radius outwards from the initial contact site. The pattern may be visualized as

a clockface in which the first of any series of strikes occurs at the center of the clockface followed by subsequent impacts at the 12 o'clock, 3 o'clock, 6 o'clock, and 9 o'clock positions. The indenter pattern is laid out in Figure 3-45, and the specific pattern of impact is portrayed in Figure 3-46. A total of 50 impacts are applied to the panel in each instance (excepting when less than 50 strikes may be required to induce rupture in the panel). The total strike energy of each impact ranges from ~0.469 kJ to ~44 kJ, corresponding to an associated relative velocity of 0.546 m/s to 5.295 m/s, depending on the simulated impact angle.

3.11.8.3 Load scenario 3

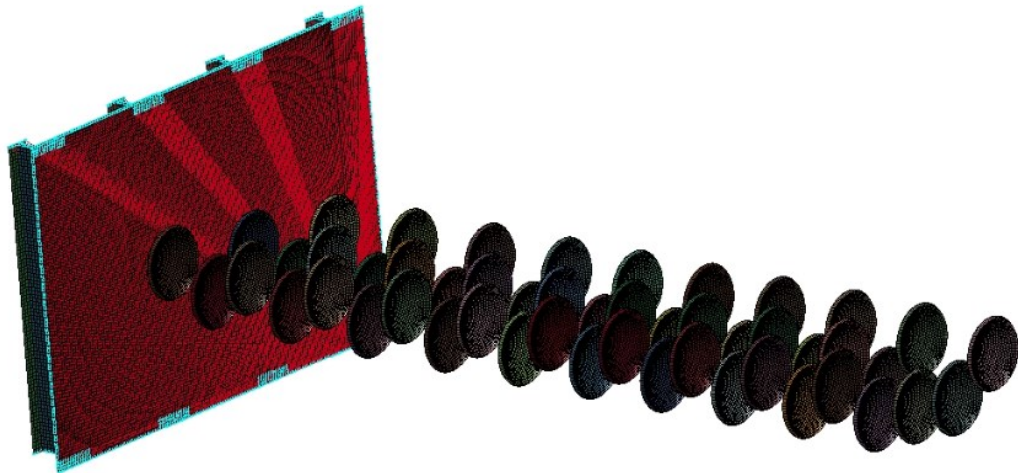


Figure 3-47. Load case #3: Expanded centralized damage area

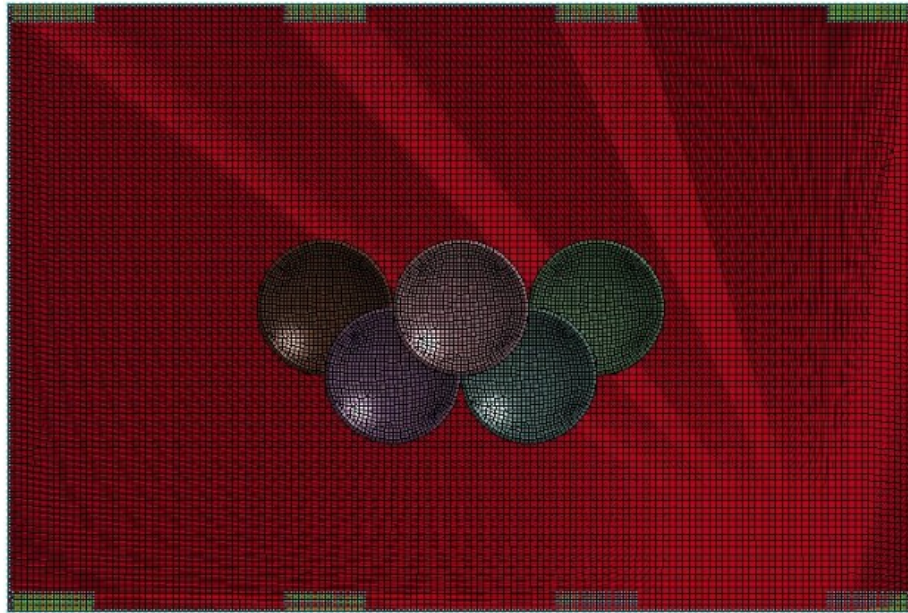


Figure 3-48. Load case #3: Impact pattern

The third load scenario institutes an expanded damage area centralized across the mid-span of the plate between the two center stiffeners. The pattern begins with a strike centered vertically and horizontally on one stiffener. It creeps laterally across the face of the grillage by applying impacts at distances of one-half radius laterally, and one-half radius above or below the previous impact as necessary to expand the damage within the mid-span of the plate. The indenter layout is presented in Figure 3-47, while the strike pattern may be visualized as a repeating pattern forming a characteristic ‘W’ shape, as evidenced in Figure 3-48. A total of 50 impacts are applied to the panel in each instance (excepting when less than 50 strikes may be required to induce rupture in the panel). The total strike energy of each impact ranges from ~ 0.469 kJ to ~ 44 kJ, corresponding to an associated relative velocity of 0.546 m/s to 5.295 m/s, depending on the simulated impact angle.

3.11.8.4 Load scenario 4

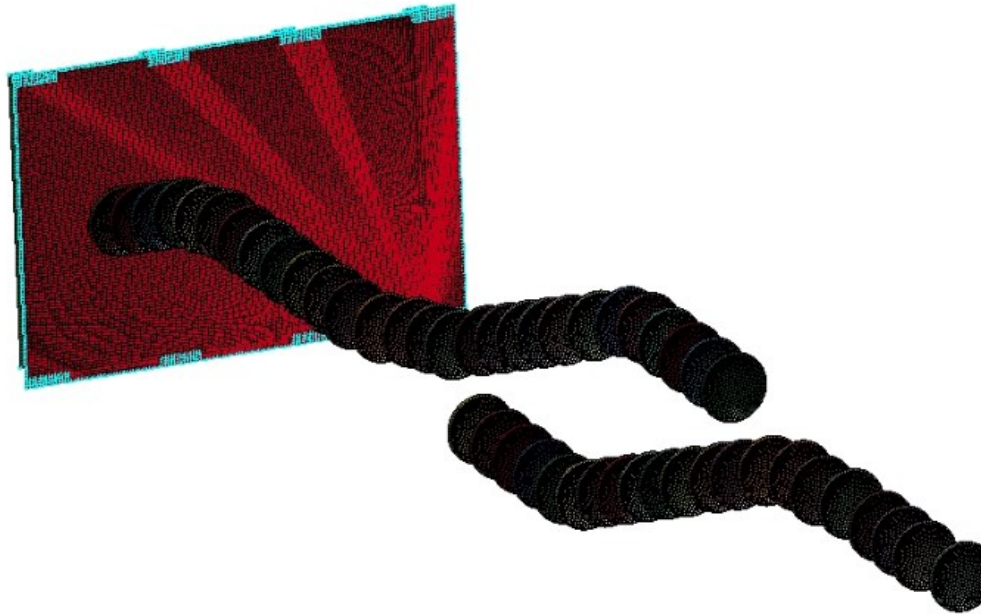


Figure 3-49. Load case #4: Wave pattern

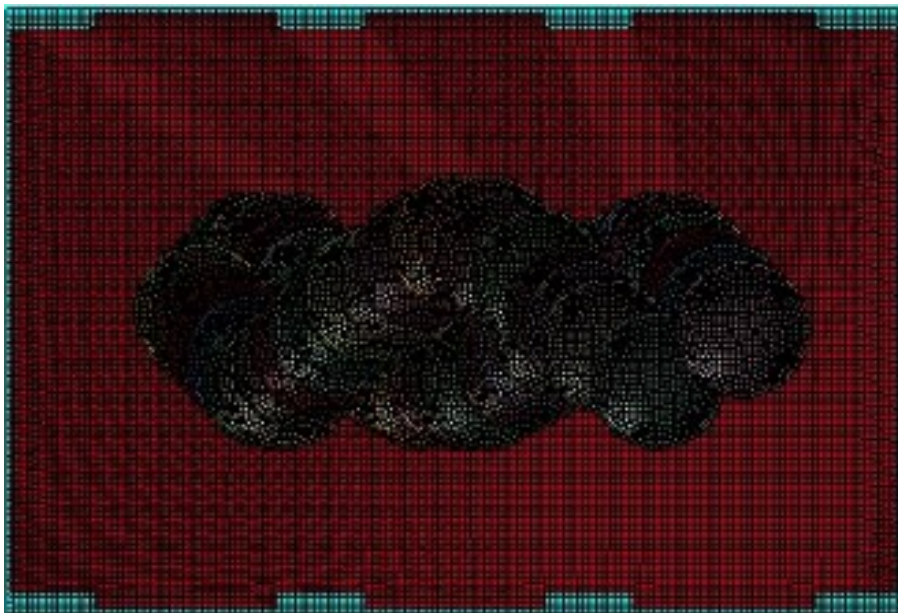


Figure 3-50. Load case #4: Impact pattern

Load scenario four develops a sinusoidal-like wave pattern originating beyond the extents of the inner stiffeners and progressing laterally to its opposing mirrored coordinate before the pattern inverts. The indenter layout and resultant impact pattern are illustrated in Figure 3-49 and Figure 3-50, respectively. A total of 50 impacts are applied to the panel in each instance (excepting when less than 50 strikes may be required to induce rupture in the panel). The total strike energy of each impact ranges from ~0.469 kJ to ~44 kJ, corresponding to an associated relative velocity of 0.546 m/s to 5.295 m/s, depending on the simulated impact angle.

3.11.8.5 Load scenario 5

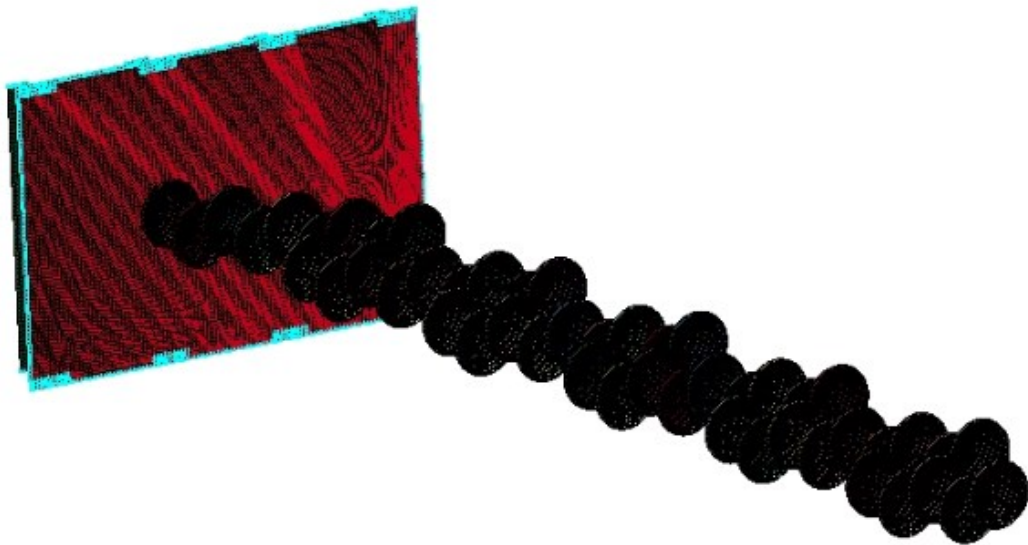


Figure 3-51. Load case #5: Expanded damage area--variation #1

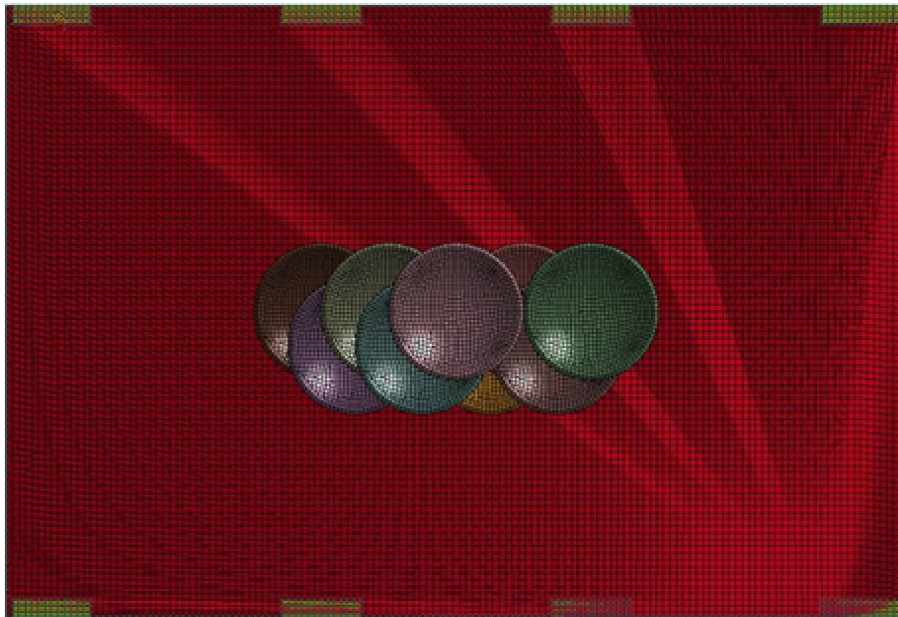


Figure 3-52. Load case #5: Impact pattern

The fifth load scenario is a variation on the expanded damage area introduced in load scenario three. However, while load scenario three focused on introducing a strike at the periphery of the previous impact sites, load scenario five presents the indenters to the impact site in such a manner as to ensure that each indenter strikes within the projection of the impact crater which would be developed by the previous indentation. The indenter layout and resultant impact pattern are displayed in Figure 3-51 and Figure 3-52, respectively. A total of 50 impacts are applied to the panel in each instance (excepting when less than 50 strikes may be required to induce rupture in the panel). The total strike energy of each impact ranges from ~0.469 kJ to ~44 kJ, corresponding to an associated relative velocity of 0.546 m/s to 5.295 m/s, depending on the simulated impact angle.

3.11.8.6 Load scenario summary

The five load cases applied throughout the numerical analysis, and their respective impact patterns, are summarized in Figure 3-53.


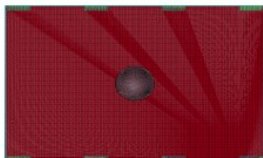





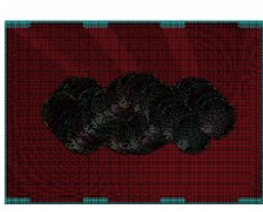
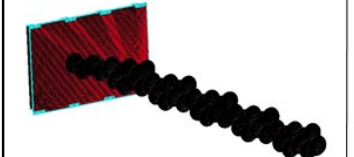

Load Scenario	Load Case Isometric View	Load Case Impact Pattern	Load Case Descriptor
1			Co-incident Indenter Strike
2			Rotational Clock-pattern Strike
3			Expanded Centralized Damage Area
4			Wave Pattern
5			Expanded Damage Area—Variation #1

Figure 3-53. Load case impact pattern summary

3.11.9 Material model

A material model is an effort to mathematically describe and predict the response of real materials to various loading conditions. Completing the numerical model includes identifying and formulating a material model and its necessary inputs to realistically define the physical behavior of the material in a manner consistent with the real world. In this research, two material models were selected from a library of validated models in the LS DYNA catalog. Then, parameters were selected based on input from more experienced advisers, empirical data from uniaxial tensile tests of real-world steel material, and a cyclic trial-and-error process to refine a formulation. The material formulations used in this numerical model include MAT_024_PIECEWISE_LINEAR_PLASTICITY (Mat_024) and MAT_020_RIGID (Mat_020). Mat_024 was used to model the grillage structure, and Mat_020 was used to model the smooth, rigid indenter used in the experiment outlined in section 3.7, and subsequently used in the numerical experimentation reported in Chapter 4.

3.11.9.1 Indenter material (MAT_020)

Mat_020 is an expedient and resource-efficient method of creating a rigid body part. In FE simulation, rigid elements are omitted from element solving, decreasing the computational cost of simulations (Hallquist, 2006). However, inputs for material density, Young's modulus, Poisson's ratio, and the inertial constraints are required to generate the rigid model while accounting for inertia and contact algorithm considerations. Additionally, a set of mass nodes were assigned to the indenter to increase the total indenter mass until it was equal to the indenter pendulum arm mass of the laboratory experiments.

3.11.9.2 Plate material (MAT_024)

Mat_024 permits a strain-rate dependent, user-defined stress-strain relationship. With this material model, the elastic and plastic portions of the response can be defined independently. A multi-linear description of the plastic region can be produced to describe the post-elastic behavior of the material by defining a curve of post-yield points. In this model, the curve used eight reference points. The multi-linear capability permits a user to model a more detailed curve than the bilinear model, while still leveraging the simple modeling and resource efficiency of linear segments. Strain-rate dependent behavior can be included in this model through the incorporation of Cowper-Symonds strain-rate parameters to scale the yield stress (Hallquist, 2006).

A great deal of experimentation was completed with the Mat_024 model to elicit a realistic response. Chief among these considerations was: the inclusion (or not) of a Cowper-Symonds strain-rate component, the treatment of post-UTS stress-strain behavior, and the identification of a failure strain. Experimental data reported by Paik et al. (2017), and the discussion provided by Storheim and Amdahl (2017), suggest values for Cowper-Symonds parameters for mild steel. However, Shimada et al. (2012) conclude that there is insufficient evidence whether strain-rate effects must be included in the dynamic cyclic loading of structural steel. After much experimentation, strain rate parameters were neglected because the empirical data consistently showed better alignment with material models that omitted strain-rate effects.

In the material formulation, only points of the engineering stress-strain curve up to the ultimate stress were considered. Given that the UTS represents a rapid transition into

material thinning behaviors (e.g., specimen necking), continued stress after the UTS has been reached will lead to the eventual plastic collapse of the structure. If necking in the material model were accurately reflected, it would manifest as significantly higher stresses at the same strain values, post-UTS. Thus, for the intent of this examination, the material can be arbitrarily considered to have reached a maximum necessary stress value at the magnitude of the UTS. Any continued development of stress at this stress or higher will lead to continued plastic strain until the fracture strain is reached. This condition is reflected in the material model by modeling all post-UTS behavior as perfectly plastic.

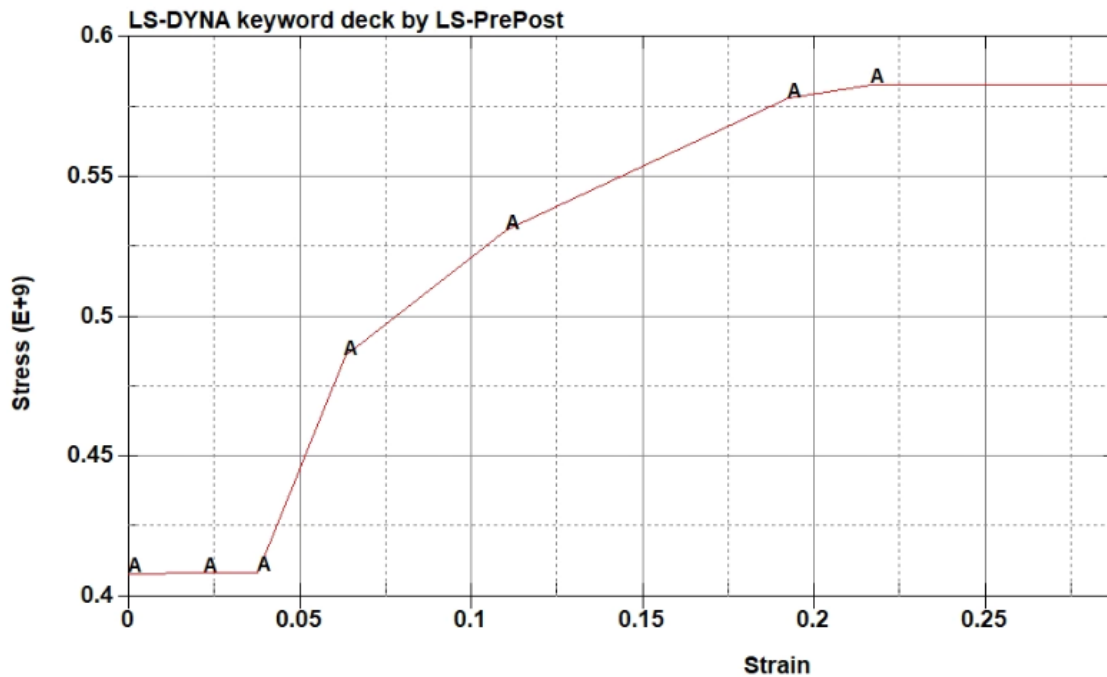


Figure 3-54. Plasticity curve for a MAT_024 multi-linear plasticity model of a mild steel sample

Table 3-10. Material model parameters for grillage structure

Density (kg/m ³)	Young's Modulus (Pa)	Poisson's Ratio (-)	Yield Stress (Pa)	Failure Strain (mm/mm)
ρ	E	ν	σ_0	ϵ_f
7850	2.07E+11	0.3	4.08e+08	0.27

The failure strain of the material model was set based on the fracture strain observed in uniaxial tensile tests. Material failure theorists and FEA analysts alike may take umbrage with where to establish a material's failure strain based on the failure mode experienced by the material. However, in this research, the precision of the failure value is secondary to observing and characterizing the macroscopic behavior of the structure under repeated impact. Consequently, the value observed in the material test was sufficient as a visual marker in the simulation to denote the accumulation of a given degree of plastic strain (0.27 mm/mm). The material model is illustrated graphically in Figure 3-54 and its parameters summarized in Table 3-10.

3.11.10 Utilizing uniaxial tensile test data for numerical simulation

Paik (2007) outlines three common methods used in FEM to employ uniaxial tensile test results. This research utilizes the 'traditional method' to transform the experimental engineering stress-strain data into a true stress-strain curve, where true stress is calculated according to equation (34), and true strain can be found using equation (35). While this method does not account for softening behavior post-UTS, the perfect plasticity assumption discussed in section 3.11.9.2 minimizes the issue with the method.

$$\sigma_{True} \approx \sigma_{Eng}(1 + \varepsilon_{Eng}) \quad [34]$$

$$\varepsilon_{True} \approx \ln(1 + \varepsilon_{Eng}) \quad [35]$$

3.11.11 Boundary conditions

The model's reactions are constrained in the numerical space to reflect the contact between the indenter and grillage and the grillage reaction within the pendulum arm test frame from the experimental set-up. In the experimental set-up, the grillage is supported in

a test frame by an all-welded perimeter of the steel support plate, which is bolted into the heavy tubular frame of the pendulum arms. The frame was intentionally designed to be as robust as possible, thereby ‘fixing’ the plate within the frame. The test frame was not expected to deform plastically during the impact trials. Moreover, the anticipated deformation of the grillage was expected to be so significant that any elasticity in the test frame would be negligible by comparison. In this way, the displacements of the panel periphery during the physical experiments attempted to restrict translations (displacements) and rotations in all degrees of freedom.

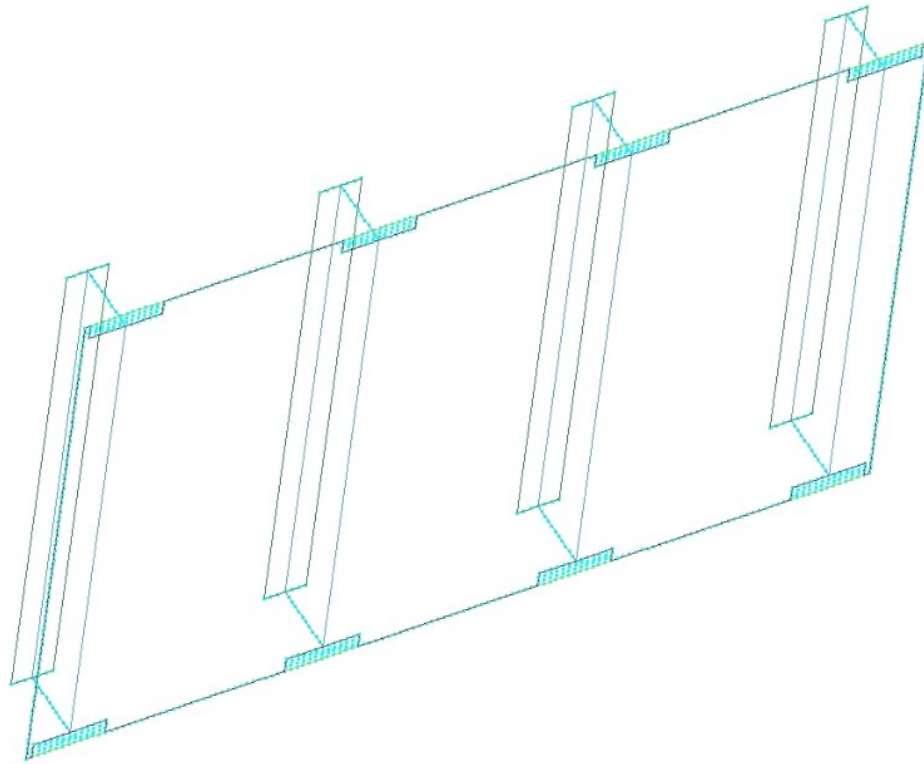


Figure 3-55. Constrained nodal rigid bodies (cyan markers) used to model the grillage boundary conditions

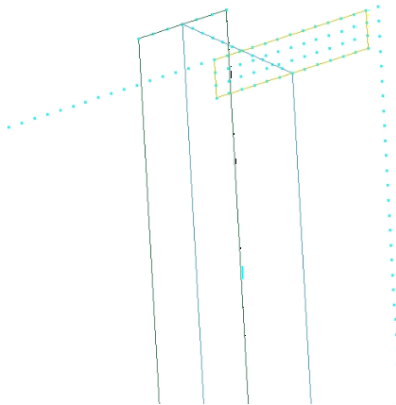


Figure 3-56. An enlarged view of the nodal rigid body markers (cyan) to model grillage boundary conditions



Figure 3-57. Experimental boundary condition placement

In the numerical model, at the extents of the panel, a `CONSTRAINED_NODAL_RIGID_BODY_SPC` condition was applied to a node-set, fixing the boundaries in translation around the plate and stiffener edges as depicted in Figure 3-55. A magnified view of the condition is provided in Figure 3-56, depicting the

exact application of this constraining set-up. The rotational degrees of freedom were left unconstrained, thereby imposing a condition in which the simulated plate edges were unable to translate. However, elements around the periphery could develop a moment that interacted with the remainder of the plate domain, consistent with the experimental boundary shown in Figure 3-57. These boundary conditions mimic the real-space constraints that would be imposed by the pendulum test frame in which the plate is fastened (and backed) by a significantly stiffer frame around its edges. Thus, as the stiff test frame prevents plate-edge displacement, it permits moment development against the restraining elements comprised of the frame bolts.

The indenter is assigned an initial velocity along a horizontal path using the INITIAL_VELOCITY_GENERATION card, and its motion is restricted to translation in the x-direction (lateral) to the face of the plate component. While not a strictly true reflection of the precise motion of the indenter when compared to the arced motion of a pendulum, this rectilinear motion restraint is a model simplification that showed good agreement for the relatively small region of impact compared to the more complex curvilinear motion. While the model attempts to replicate experimental conditions, it is acknowledged that the numerical boundary conditions are infinitely stiff compared to those that might be experienced in the real-space collision. Contact with the geometry will be required to model a collision successfully.

3.11.12 Contact

The model uses an automatic surface-to-surface contact definition to allow interaction between the indenter and grillage models. The definition was applied to a

master part set comprised of all deformable parts in the model space and a slave part consisting of the rigid indenter. The penalty method has two significant advantages for use in this model. First, the exact conservation of momentum is maintained without implementing specific impact and release conditions. Second, LS Dyna's standard contact algorithm requires no special treatment of the intersecting surfaces provided the interacting structures are defined by similar material (Hallquist, 2006). Further explanation of penalty-based contact is treated comprehensively by Hallquist (2006).

3.11.13 Damping

During numerical model development, low-frequency structural modes were observed. Following recommended practices provided by Hallquist, (2006), mass damping was applied using DAMPING_PART_MASS to damp the lowest frequency mode of the grillage structure observed after an undamped impact. After each discrete impact of a multiple impact sequence, the fundamental frequency was estimated from an undamped transient analysis. Subsequently, the model was re-solved with an appropriate mass damping coefficient invoked on that portion of the impact scenario. The recommended typical damping value of 10% of the critical mass damping coefficient was calculated according to equation (36).

$$c = \frac{0.4\pi}{T} \quad [36]$$

A comparison with a purely undamped model showed a typical discrepancy with the deflection of the damped model on the order of 3% or less. The finding is unsurprising given the innate stiffness of the design of the grillage structure. However, the introduction of damping parameters necessitated the addition of such significant simulation time

between impacts in the simulation that it rendered the simulations unwieldy to perform and analyze. Thus, given the broad performance similarities between the purely undamped model and the damped model, damping was omitted from further analysis. The elastic vibratory response of plate structures exhibit far more sensitivity to damping in unstiffened configurations, with the role of damping significantly reduced as the structure assumes a stiffer natural configuration (Zhu et al., 2018).

3.11.14 Time steps for explicit simulations

3.11.14.1 Courant-Friedrichs-Lewy condition

Explicit codes such as LS DYNA have an algorithmic stability limit that governs the maximum stable time step which can be employed in the integration of data within the FE solver's computations. For explicit analyses, the largest stable time step is governed by the Courant-Friedrichs-Lewy condition, often termed the characteristic length. For small deformations in individual elements, the time step is controlled by the speed of wave propagation through the material. For explicitly integrated analyses, the numerical stress wave must propagate less than one element width per time step for stability to be maintained (Quinton, personal communication, 2020). Thus, for this analysis the time step is automatically determined as an underlying function of the FE software as the minimum stable time step in the smallest deformable finite element in the mesh. The Courant-Friedrichs-Lewy condition consequently requires the numerical time step to be a fraction of the actual theoretical time step (Hallquist, 2006).

3.11.14.2 Time step stability

Intuitively, the condition leads to a number of important conclusions. Chief among these is that an analysis with an appropriately-sized time step will be a stable solution set. If the solution is unstable, as would happen with a time step that is too large, the solution would continue with unbounded increasing displacements, creating a response that is unstable and inaccurate. Conversely, time steps which are excessively small will, at best, create a solution that is so prohibitively expensive computationally that the solve time is unreasonable, or at worst, lead to a FE simulation that fails to terminate. While the relationship between time step size and solution stability is relevant to explicit analyses, it is also important to recognize that while an accurate solution must be associated with a stable solution, a stable solution is not necessarily accurate (Quinton, personal communication, 2020). A properly executed solution will demonstrate both stability and accuracy.

3.11.15 Numerical model validation

The numerical model discussed above was validated against the results of the grillage experiments introduced in section 3.7. The model was considered validated when the deflection versus impact number of the experimental and numerical curves showed acceptable agreement.

3.11.15.1 Load

In the numerical model, the load is applied to the indenter by setting the velocity of the indenter at an equivalent velocity to the closing (or relative) velocity attained by the two pendulum arms at impact when they are both released simultaneously from an angle

of 50° from the vertical axis as per Figure 3-12. The overall indenter motion is assigned only a velocity component with no contributory or deleterious acceleration effect before the impact of the indenter part with the grillage structure. The numerical model differs from the experimental set-up in that the numerical model features a stationary grillage structure impacted by an indenter moving at an equivalent velocity as opposed to two individual bodies closing at discrete velocities. This approach was a modeling simplification made to increase the efficiency of the model when conducting multiple consecutive impacts, and its derivation has been previously provided and discussed in section 3.11.8. The equivalent closing speed representing an experimental impact from a pendulum angle of 50° can be determined by energy methods, and the relationship between single carriage equivalent speed and two carriage closing speeds has been previously presented in Table 3-1.

3.11.15.2 Results

A sensitivity study was conducted with a second model that mirrored the experimental test conditions. Upon review of the energy parameters, force, stress, strain, and deflection resultants when compared across the two models, the author—in consultation with more senior experts—was satisfied that the equivalent velocity model produced nominally similar results to the dual-velocity body model, supporting the calculations proposed by Quinton (personal communication, 2020) and building a novel application of the extant pendulum energy theory touched upon by Gagnon et al., (2015). The results of the numerical model deflection were compared across four impacts recorded in the experimental model. The results are displayed as a deflection versus impact number curve in Figure 3-58. It is apparent by inspection of the figure that the numerical model

underestimates the initial deflection, and progressively overestimates the deflection in later impacts. This discrepancy, and the subsequent reversal of deflection behaviors during progressive impacts is not unexpected given the idealized continuity of numerical material versus the material voids, locked-in construction stresses, or other material defects in the laboratory material.

Table 3-11. Numerical model deflection resulting from a range of material models

Impact #	Accumulated Experimental Deflection (cm)	Relative change (%)	8-segment Multi-linear	Relative change (%)	8-segment Multi-linear (Cowper Symonds) C=40.4 P=5	Relative change (%)	8-segment Multi- linear (Cowper Symonds) C=3200 P=5	Relative change (%)	8-segment Multi-linear Differing (Indenter Speed Adjusted)	Relative change (%)
1	9.01	-	8.58	-	6.45	-	7.56	-	8.58	-
2	2.76	30.63263041	2.82	32.86713287	2	31.0077519	2.44	32.27513228	2.82	32.86713
3	1.09	39.49275362	2.2	78.0141844	1.44	72	1.9	77.86885246	1.3	46.09929
4	1.012	92.8440367	1.9	86.36363636	1.21	84.0277778	1.5	78.94736842	1.3	100
Total Deflection	13.872	-	15.5	-	11.1	-	13.4	-	14	-

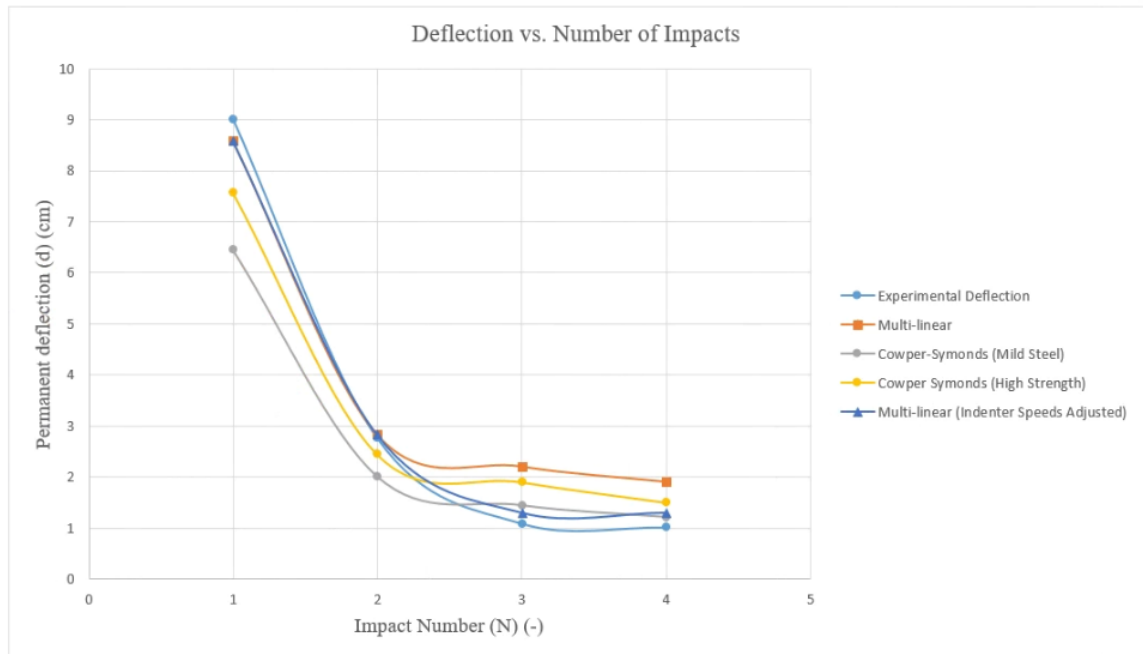


Figure 3-58. Deflection versus number of impacts for a rigid, smooth, spherical indenter at 50° pendulum arm angles

The relative percentage deflection increase between each individual hit was identified and tabulated in Table 3-11 to examine the validity of the material's behavioral trend. The process of modifying the numerical model to improve the agreement is cyclic, sometimes at-best an informed trial-and-error premise to find material parameters that adequately describe a real-world reaction fraught with potential idiosyncrasies and unknowns. Figure 3-58 displays the fit of a number of the best efforts to fit the material behavior. It is important to note that each impact is a discrete event. Thus, for each impact, the observed permanent deflection of the grillage structure is plotted for the five material formulations corresponding to each impact number.

The individual graphs are smoothed using the standard curve smoothing algorithm contained within Microsoft's *Excel 2016* software. The curves have been smoothed to provide readers with an easily digestible visual indication of the relative severity of hardening behavior observable across the five formulations for comparison with the experimentally observed deflection. The interpolated curvature between discrete impacts is not an accurate basis model for investigators to draw conclusions about deflection magnitudes between impacts any more so than might be achieved by a straight-line straight-marker plot. The key takeaway from the plot is the correlating behavior that may be observed when the same smoothing algorithm is applied to a material formulation's simulated results and the experimental laboratory data. The plot permits an analyst to observe the similarity in behavior between the experimental deflection and multi-linear, varied-speed indenter through visual inspection.

Initial attempts to fit a material model showed inferior agreement across more than two impacts. Myriad variations were input and considered to achieve a better alignment as impact number increased. The adopted solution came not from a change in the material model, but a change in the loading conditions upon reflection of the experimental test set-up. The initial load in the experiment is an impact from which it is assumed that both pendulum arms are released simultaneously from a 50° angle and impact horizontally at the bottom-most portion of the pendulum arc length. In other words, both pendulum arms have attained maximum velocity at the point of impact. However, after the initial impact, the panel undergoes a deformation. Thus, in subsequent impacts, the two pendulums must swing further along their respective arcs, causing each pendulum to lose a portion of their

maximum speed. This implies that in each follow-on impact, the impact velocity is not that assigned to the originally proposed 50° but is reduced slightly with each indentation. Assuming that the pendulums are swinging on a circular arc, the energy loss associated with the increased arc swing on each indentation was identified, and the new equivalent speed was determined for the numerical model. Assigning the new speeds to each respective impact, the agreement with experimental results improved dramatically. However, there was still a significant discrepancy with the third and fourth impact that could not be explained by the material model.

Upon re-inspection of the photographs and data of each impact, it was noted that the direction of impact had drifted horizontally after the second impact. The cause and influence of this error were promptly and conclusively identified but will not be amplified here. A detailed discussion is provided in Chapter 5. The existence of the secondary impact site can be observed in the highlighted section of Figure 3-19. The photograph clearly shows a secondary impact edge identifying where the perimeter of the indenter made contact with the panel in the third and fourth impact. The drift of the indenter during the two impacts was estimated by overlaying the indenter and identifying the impact center. In the numerical space, the impact velocity of indenter three and indenter four was then decomposed into forward and sideways components and incrementally altered until the impact location mirrored that observed in experimentation.

Assessment of the deflection pattern produced the multi-linear (indenter speeds adjusted) curve in Figure 3-58, which adequately models the experimental deflection observed. Side-by-side profile comparison of the experimental FARO scans and the

simulated deflection pattern is shown in Figure 3-59. The outstanding discrepancy between the final numerical and experimental curves can likely largely be explained by two contributing elements: 1) the numerical indenter may not adequately model the sliding/rotational behaviors of the indenter as moments develop intra-impact. The behavior may likely be exacerbated as the contact-surface becomes increasingly non-Hertzian (highly non-planar) in orientation; and, 2) during experimentation, the test frame was assumed sufficiently robust such that only small-scale elastic effects and no permanent inelastic deformation was expected. Upon conclusion of the third and fourth impacts, there was notable and significant deformation in the pendulum frame. Following removal of the grillage from the pendulum frame, the deformation was determined to be elastic. Regardless, the presence of significant elastic deformation in the test frame would have been associated with a reduced energy transfer into the grillage, presenting as a lower deflection in impacts three and four when compared with the significantly stiffer numerical boundaries.

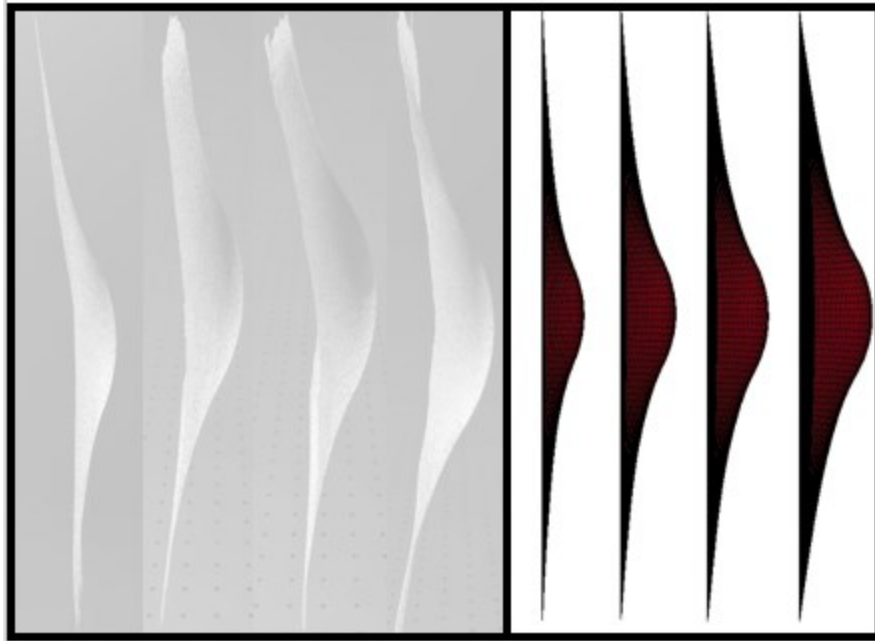


Figure 3-59. Profile comparison of the experimental FARO scans versus the simulated deflection pattern

Chapter 4 EXPERIMENTAL AND NUMERICAL FINDINGS

Chapter 4 presents the findings observed through the investigation of the reaction of a transversely-stiffened grillage structure to a variety of accumulated damage scenarios. The scenarios were selected to provide a general characterization of panel behavior by interrogating various aspects of the response. Thus, the scenarios are designed to represent impact patterns that might be seen from various expected shipboard evolutions resulting in a collision state. For example, the load scenarios baseline the behavior by examining: coincident strikes; progress to examine strikes radiating outward from a central position (e.g., repeated sway into a stationary object such as an anchor buoy); strikes progressively located on the perimeter of an expanding damaged area (e.g., between-stiffener strikes from incidental contacts over a voyage duration); impacts occurring over a generally dispersed sinusoidal wave pattern (e.g., slightly above, below, and at a central horizontal strike line); and, impacts originating at one inner stiffener location and progressively proceeding horizontally across the face of the plate (e.g., a growler bumping across the hull plate as the hull proceeds along a course through the water). The impact patterns are exploratory and not precisely mapped with observed object displacement within an actual marine scenario. The investigation was conducted using the numerical model explicated in Chapter 3.

The results of each simulation set are presented in the form of effective plastic strain versus the number of cycle plots. This format is widely used in the literature (Huang et al., 2000; Xu & Yue, 2006; Zhu et al., 2018) as a display method for comparison across impact

types or materials. The effective plastic strain is a single value representation of any plastic strain increment along the yield surface of an element during the impact cycle.

4.1 Experimental observations

4.1.1 Experimental stress-strain data

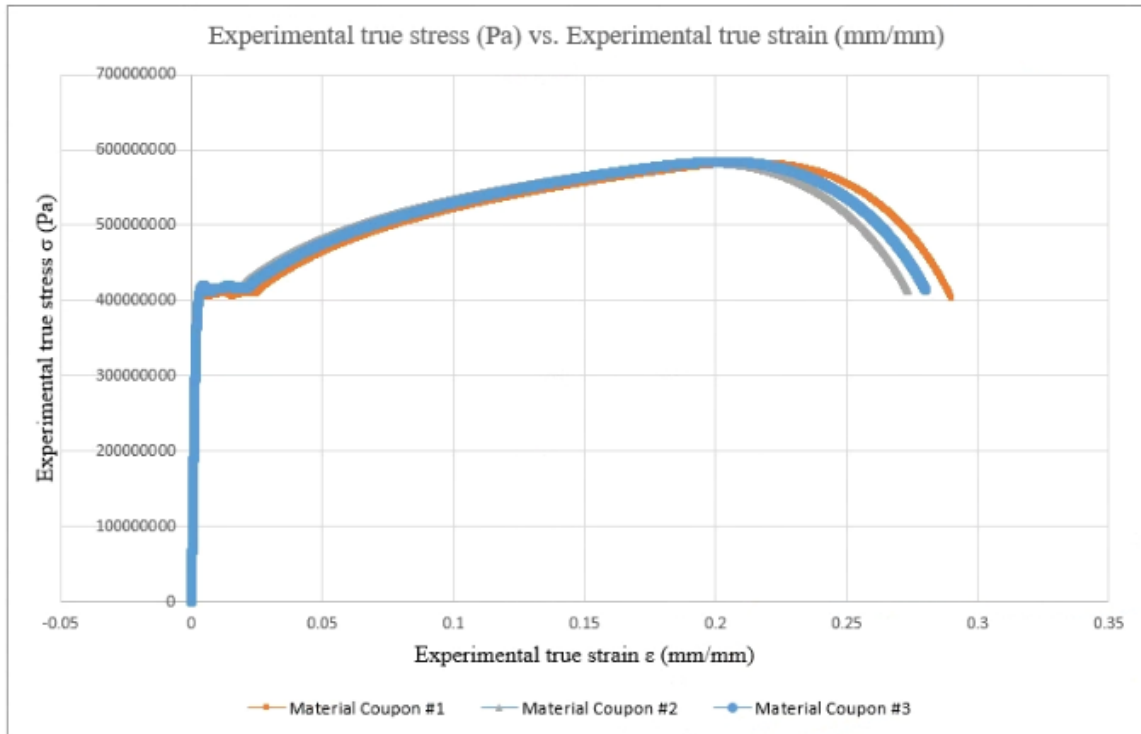


Figure 4-1. True stress-strain data for experimental panel specimen

Table 4-1. Material summary for true stress and true strain data derived from uniaxial tensile test

Specimen	Engineering Yield Stress (MPa)	Engineering Ultimate Tensile Stress (MPa)	Engineering Failure Strain (mm/mm)
1	420	583	0.27
2	431	582	0.27
3	431	584	0.29
Average	427	583	0.277

The engineering stress-strain data discussed in section 3.10, was adjusted using equation (34) and equation (35) to produce true-stress strain reflecting the laboratory material. The superimposed data is collected and presented in Figure 4-1. A tabulated summary of the true material properties as transformed from engineering values is given in Table 4-1.

4.1.2 Strain accumulation

A complex variety of behaviors were observed among the various test cases. The demonstrated behaviors vary not only with the applied impact energy but with the load history/method of load application as well. Given that the material response is non-linear stress-strain behavior, the method of load application affects the observed outcomes (Paul et al., 2015).

4.1.3 Load case 1

4.1.3.1 Accumulated plastic strain of models

The first load case considered investigated a coincident repeating impact centralized vertically and horizontally between transverse stiffeners, as illustrated in Figure 3-43. A total of 50 impacts were applied to the panel in each instance (excepting when less than 50 strikes were required to induce rupture in the panel). Examination of Figure 4-2. reveals that impact scenarios between 5° and 20° (indenter speeds of 0.546 m/s to 2.176 m/s) survived 50 indenter strikes without the specified failure strain occurring. Conversely, impacts occurring from 25° to 50° (indenter speeds of 2.712 m/s to 5.295 m/s) resulted in rupture of the grillage in progressively fewer impacts with each increased energy application. Figure 4-3 illustrates the accumulated damage pattern that occurs for varying

degrees of impact after either 50 indentations or the indentation immediately preceding the panel progressing to the specified failure strain. Likewise, Figure 4-4 shows the corresponding panel-side evolution of plastic damage.

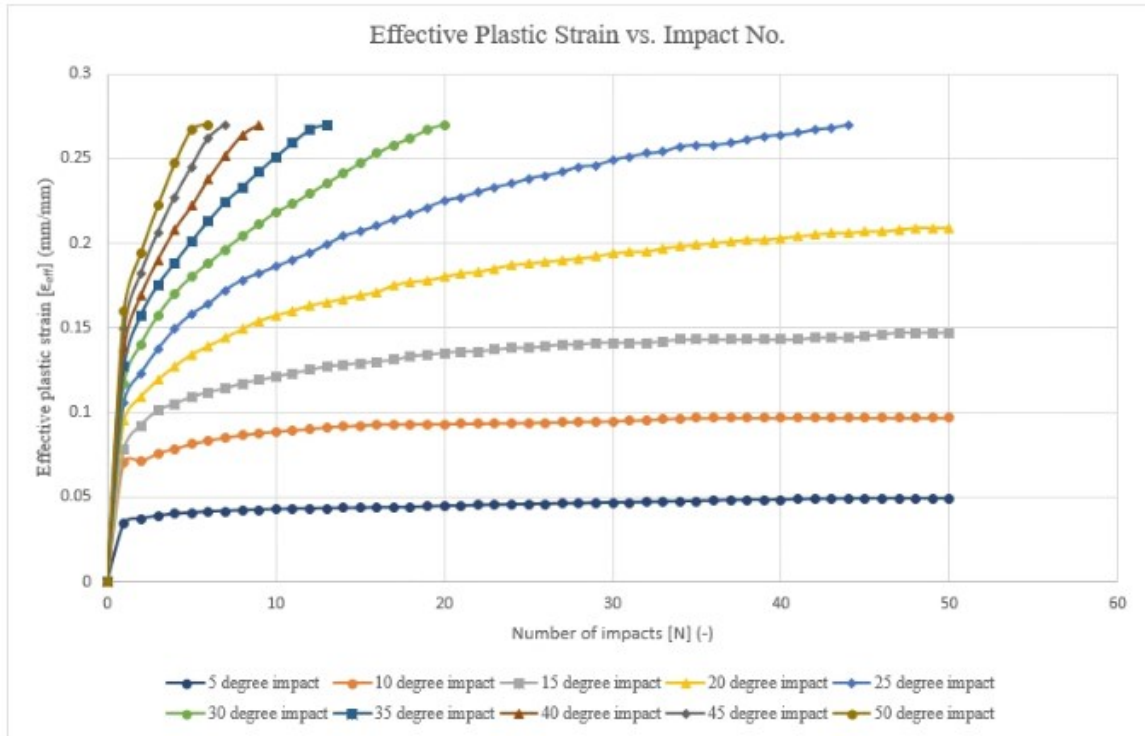


Figure 4-2. Load case #1: Effective plastic strain versus impact number

4.1.3.2 Deformation shapes

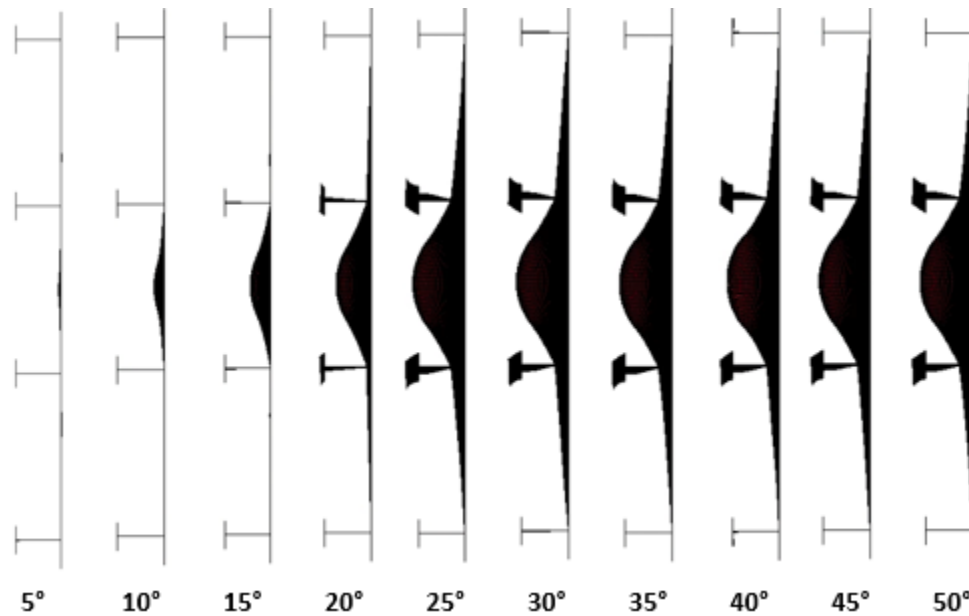


Figure 4-3. Load case #1: Accumulated damage pattern (following 50 impacts or at failure strain attainment if occurring before 50 impacts)

The inspection of Figure 4-3 reveals that an increased application of energy results in a marked progression of the impact pattern after 50 strikes. An unexpected observation is a behavior at an energy level associated with 25°. At a subsequent energy stage, a decrease in the overall depth of the indentation can be seen while simultaneously an increased development of deformation is seen in the inner stiffener configuration. Moreover, the first visible signs of plasticity in the outer stiffener sets are visible.

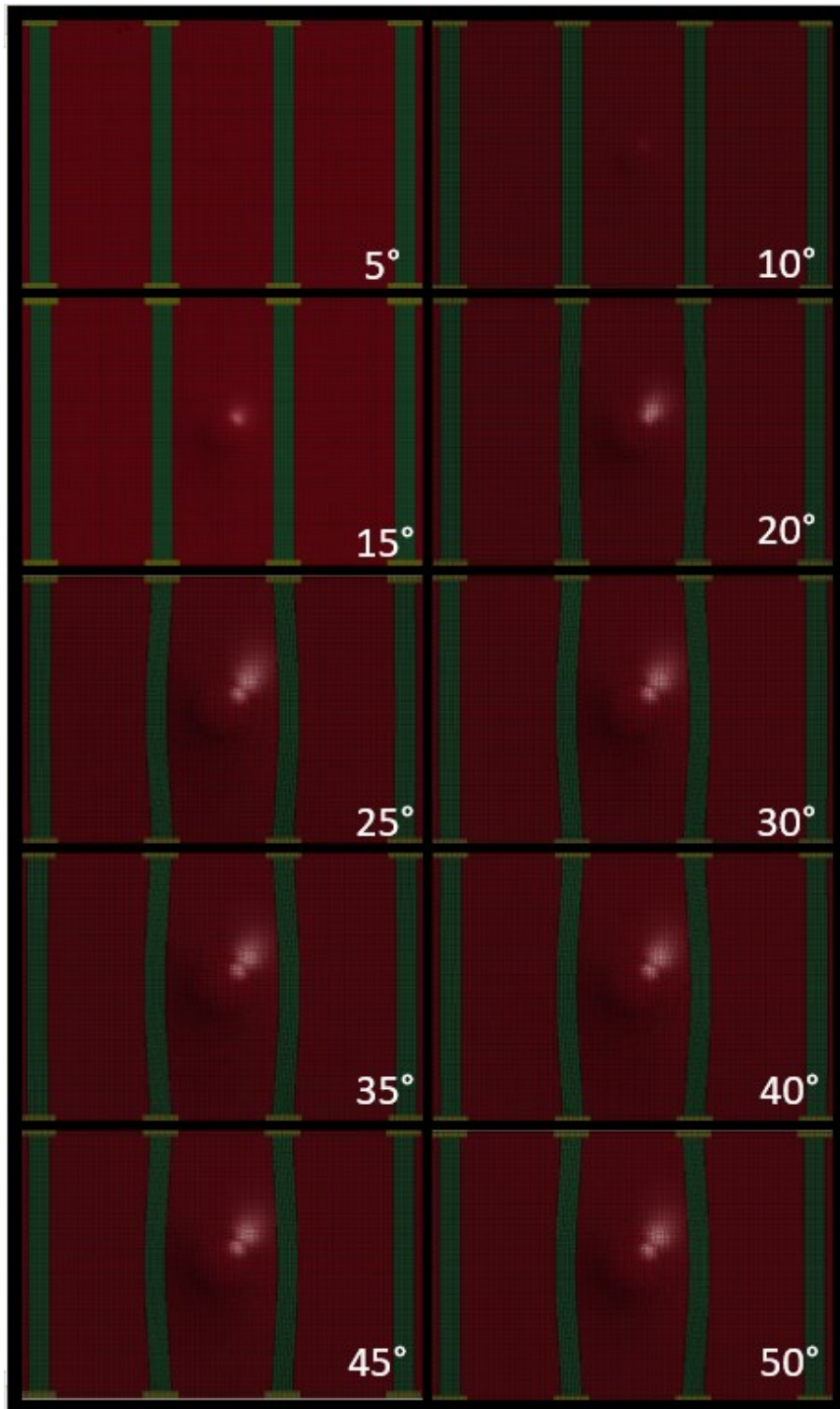


Figure 4-4. Load case #1: Accumulated damage pattern (following 50 impacts or at failure strain attainment if occurring before 50 impacts) --stiffener view

As the energy level increases beyond 30°, a transition in the visibly observable behavior occurs. While the lateral depth of the impact site no longer demonstrates dramatic progression, the accumulation of damage now presents as increased stiffener deformation at a reduced number of cycles as shown in Figure 4-4. In other words, significant damage accumulates across a broader section of the structure without a necessary progression in damage at the center of impact. The consistent pattern of the progression of damage across multiple energy levels makes the coincident strike pattern a useful baseline case for cross-comparison against impact variations.

4.1.4 Load case 2

4.1.4.1 Accumulated plastic strain of models

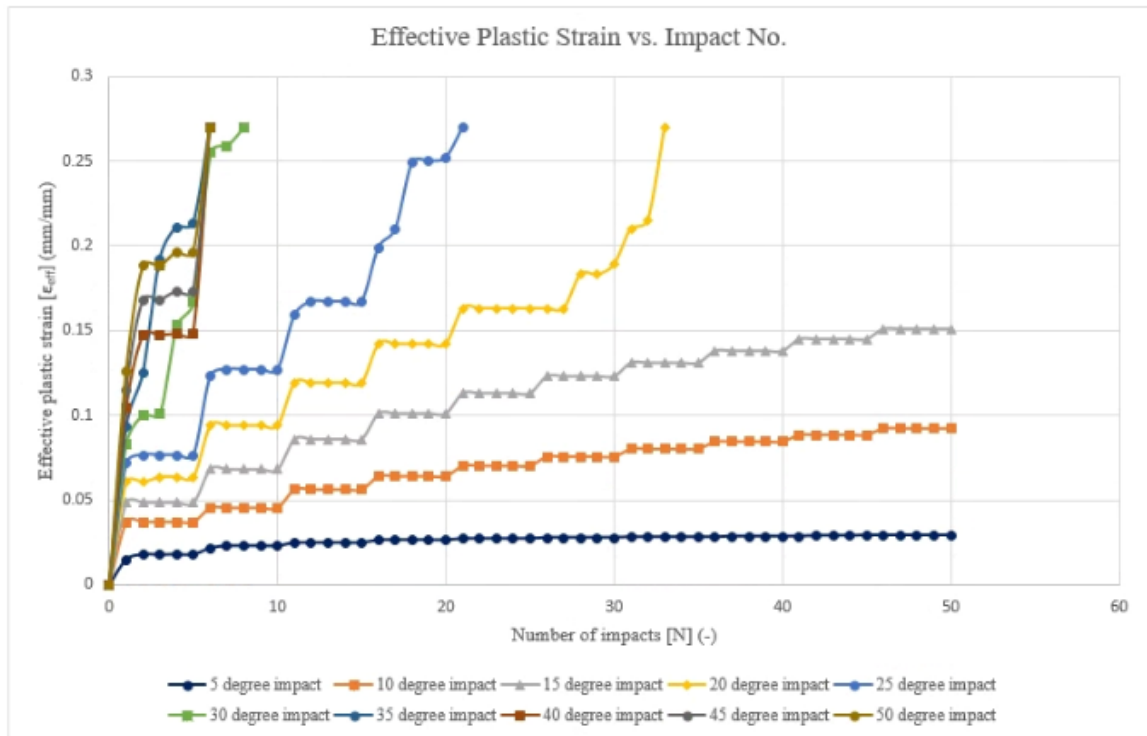


Figure 4-5. Load case #2: Effective plastic strain versus impact number

The second load case considered a series of strikes radiating outward from a central position. The first strike occurs in the horizontal and vertical center of the plate, equally spaced between the transverse stiffeners. The strike pattern then makes contact in a circular pattern with the impact center corresponding to the perimeter of the original impact site (i.e., the contacts are translated one-half indenter diameter) with each indenter oriented to one of the four cardinal points of a 360° coordinate plane.

The impact pattern is shown in Figure 3-45. A total of 50 impacts were applied to the panel in each instance (excepting when less than 50 strikes were required to induce rupture in the panel). Examination of Figure 4-5 reveals that impact scenarios between 5° and 15° (indenter speeds of 0.546 m/s to 1.635 m/s) survived 50 indenter strikes without the specified failure strain occurring.

Conversely, impacts occurring from 20° to 50° (indenter speeds of 2.176 m/s to 5.295 m/s) resulted in rupture of the grillage in progressively fewer impacts with each increased energy application. Figure 4-6 illustrates the accumulated damage pattern that occurs for varying degrees of impact after either 50 indentations or the indentation immediately preceding the panel progressing to the specified failure strain. Figure 4-7 shows the corresponding panel-side evolution of plastic damage.

4.1.4.2 Deformation shapes

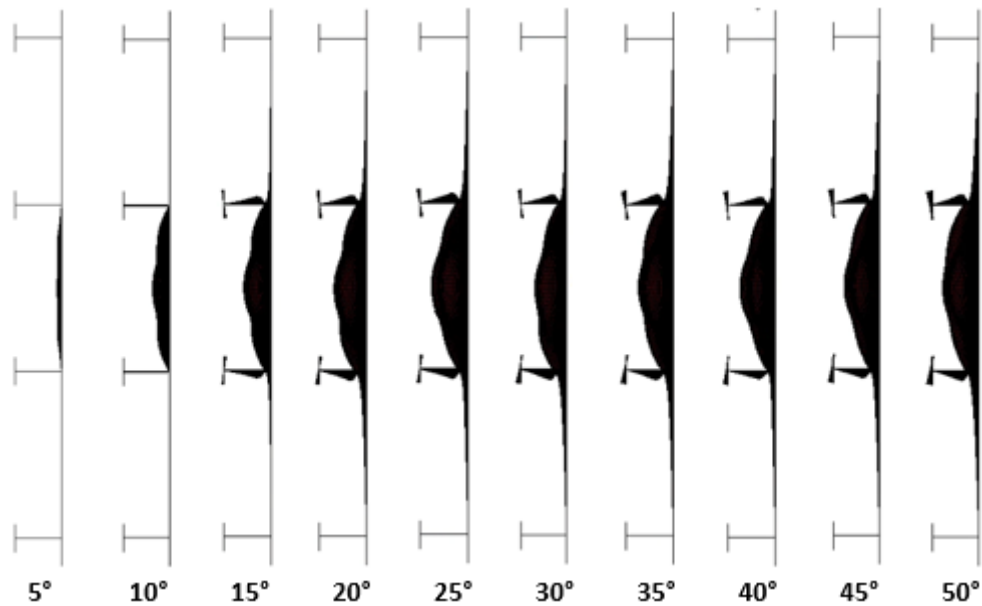


Figure 4-6. Load case #2: Accumulated damage pattern (following 50 impacts or at failure strain attainment if occurring before 50 impacts)

The inspection of Figure 4-6 reveals that an increased application of energy results in a marked progression of the impact pattern after 50 strikes. The deformation pattern transforms at an energy level associated with 30°. Subsequent higher energy applications do not provide a significant lateral expansion of indentation crater depth.

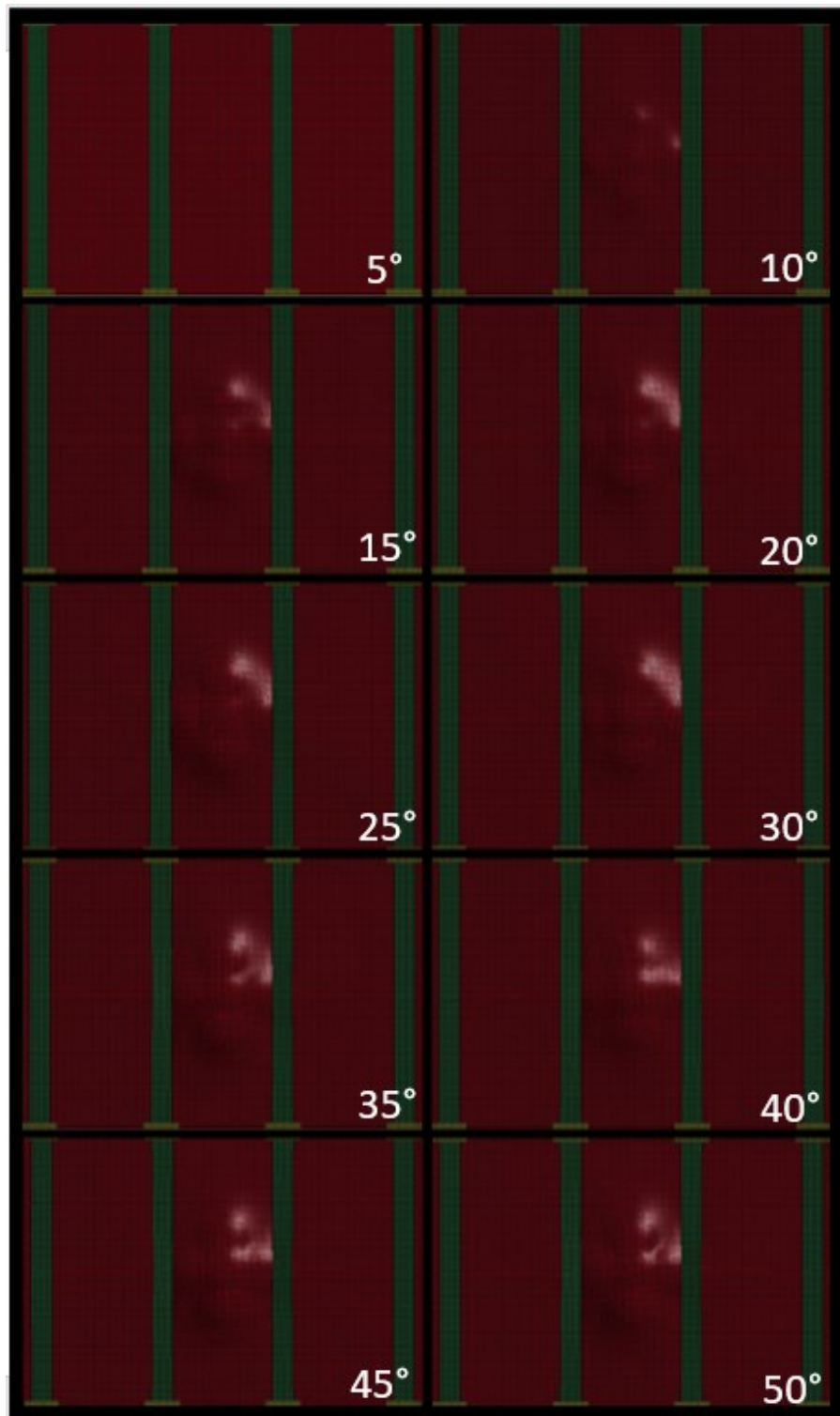


Figure 4-7. Load case #2: Accumulated damage pattern (following 50 impacts or at failure strain attainment if occurring before 50 impacts) --stiffener view

The trend in behavior is apparent by inspection of Figure 4-7. Through comparison with the corresponding image in Figure 4-6, it can be noted that a generalized indentation pattern supersedes the appearance of discrete indentations. Subsequent impacts flatten the periphery of individual impacts, or the asperities of the impact crater, until the overall damage case resembles an expansion of the impact site denoted in load case 1 (Figure 4-4).

As the energy level increases beyond 30°, a transition in the visibly observable behavior occurs. While the lateral depth of the impact site no longer demonstrates dramatic progression, the accumulation of damage now presents as increased stiffener deformation at a reduced number of cycles, as shown in Figure 4-6. A notable difference in the accumulation history is observable in Figure 4-7. Examination of the stiffener deflection pattern reveals that the accumulation of damage to the stiffeners is focused through the stiffener web. In other words, significant damage accumulates in the stiffener web without the visual presence of an associated significant bending/bowing through the longitudinal axis of the stiffener configuration.

4.1.5 Load case 3

4.1.5.1 Accumulated plastic strain of models

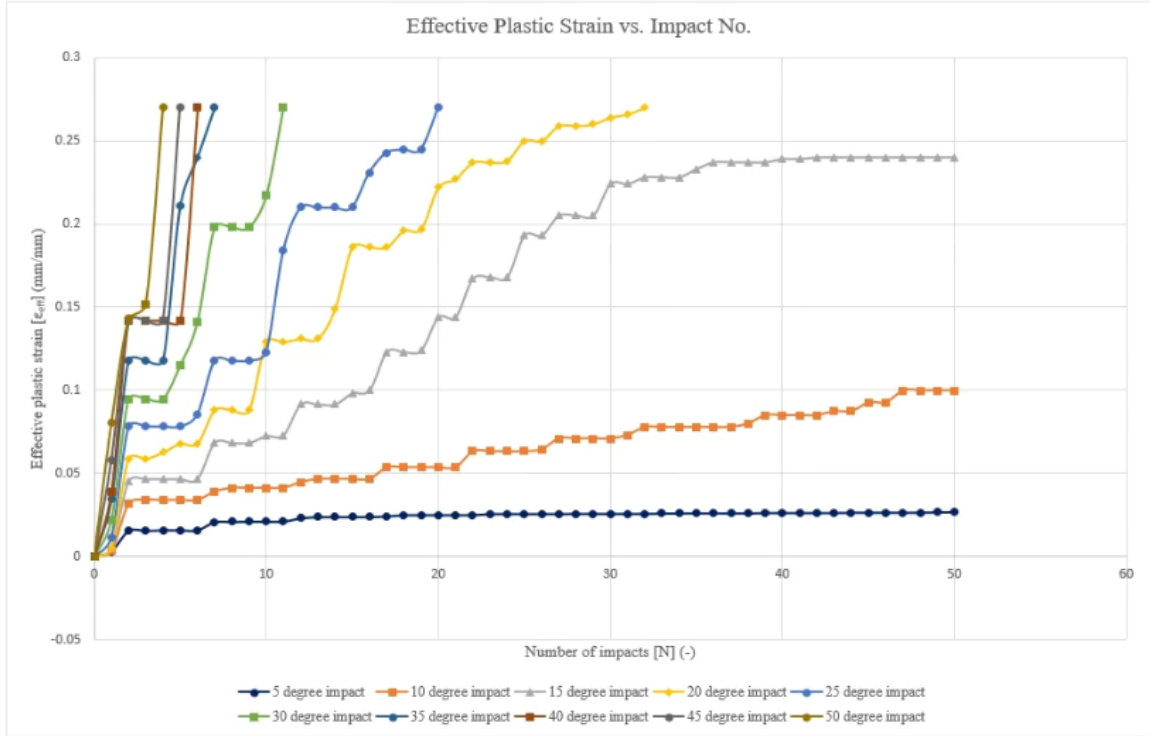


Figure 4-8. Load case #3: Effective plastic strain versus impact number

The third load case marks the first instance in which a series of strikes directly impacts a stiffener. The first strike occurs in the horizontal and vertical center of the left-inner transverse stiffener, and the impact pattern proceeds across the lateral face of the panel pattern making contact in indenter half-diameter increments above, below, and across the face of the grillage. The terminal point is the opposing inner transverse stiffener, after which the pattern repeats. A total of 50 impacts were applied to the panel in each instance (excepting when less than 50 strikes were required to induce rupture in the panel).

The examination of Figure 4-8 demonstrates the failure pattern for the third load case. Repeated strike velocities between 5° and 15° (indenter speeds of 0.546 m/s to 1.635

m/s) survived 50 indenter strikes without the specified failure strain occurring. Meanwhile, impacts occurring from 20° to 50° (indenter speeds of 2.176 m/s to 5.295 m/s) resulted in grillage rupture in progressively fewer impacts with each increased energy application.

4.1.5.2 Deformation shapes

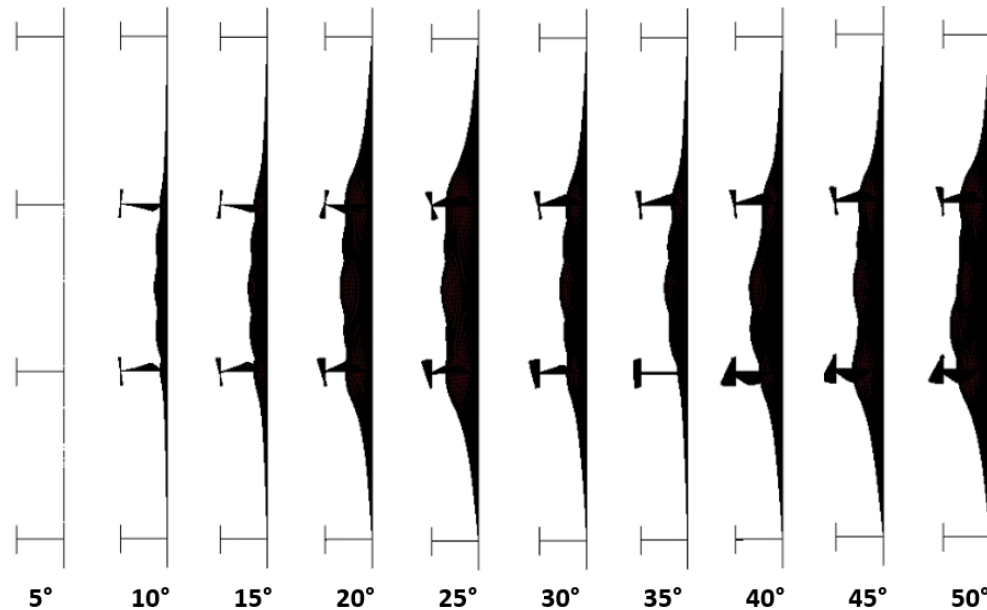


Figure 4-9. Load case #3: Accumulated damage pattern (following 50 impacts or at failure strain attainment if occurring before 50 impacts)

Figure 4-9 displays a wide range of deformation patterns prior to attaining the requisite failure strain. This load case demonstrates a complex relationship between material translation and plastic accumulation. In some instances, significant deflection of the grillage components is possible before accumulated strain is sufficient to incur a component failure. At the same time, in other instances, the initial energy application occurs in a location and with sufficient magnitude to create a condition of rupture with minimal associated gross deflection of components.

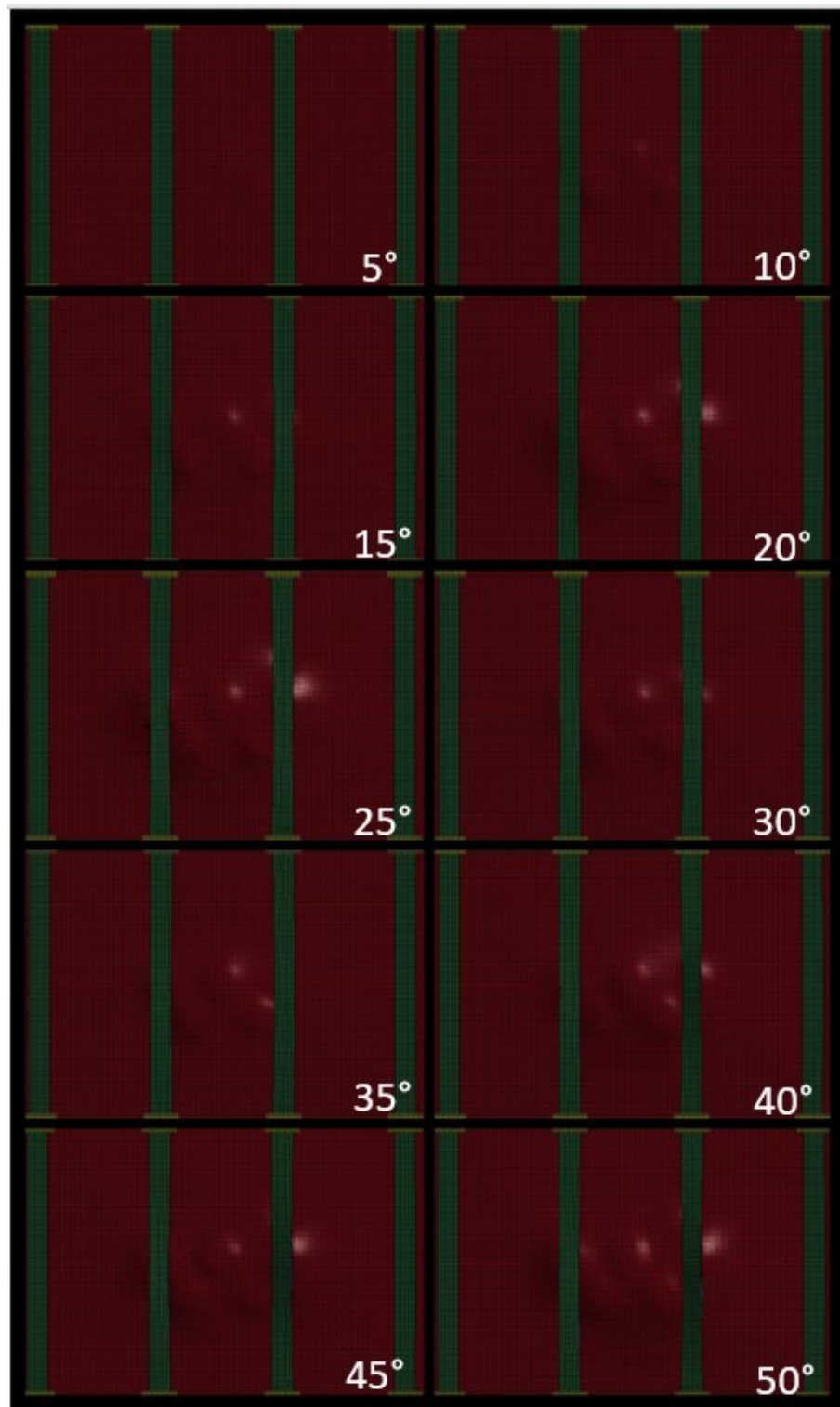


Figure 4-10. Load case #3: Accumulated damage pattern (following 50 impacts or at failure strain attainment if occurring before 50 impacts) --stiffener view

Reviewing the impact development history in Figure 4-10, the lack of transverse bending in the stiffeners makes it immediately evident that the evolution of the accumulated plasticity is not primarily governed by plate bending behavior. Instead, a concentration of energy at the stiffeners induces immediate tripping and buckling behaviors in the stiffener webs with an associated energy application as low as that induced by the 10° impact (1.092 m/s or 1.872 kJ applied energy). Furthermore, the accumulation pattern graphed in Figure 4-8 depicts that low-energy impacts primarily experienced strain growths when damage was incurred on the stiffener. Conversely, at higher energy applications, the maximum strain magnitude developed was mostly irrespective of impact location.

4.1.6 Load case 4

4.1.6.1 Accumulated plastic strain of models

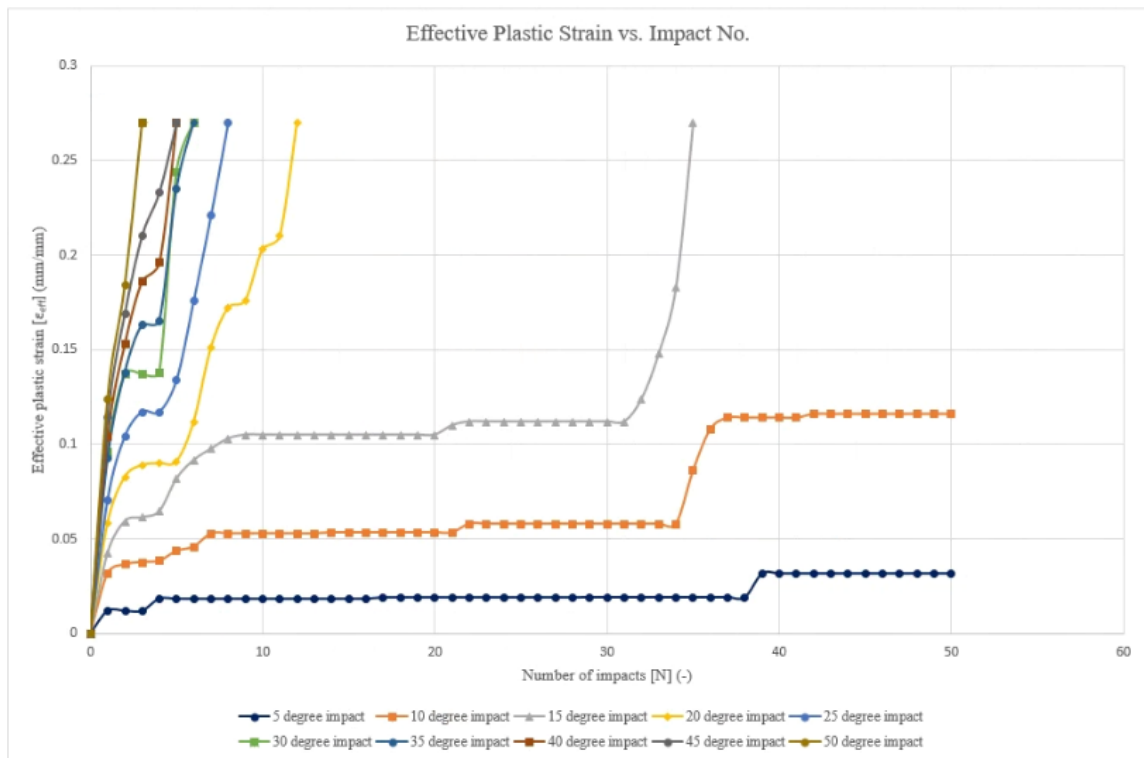


Figure 4-11. Load case #4: Effective plastic strain versus impact number

Load case four presents a series of indenters over a generally dispersed sinusoidal wave pattern originating at one inner transverse stiffener, proceeding across the face of the panel to a second inner stiffener. The impact pattern order is then applied in inversely terminating at the starting stiffener. The impact pattern is depicted in Figure 3-49. A total of 50 impacts were applied to the panel in each instance (excepting when less than 50 strikes were required to induce rupture in the panel). Examination of Figure 4-11 reveals that impact scenarios between 5° and 10° (indenter speeds of 0.546 m/s to 1.092 m/s) survived 50 indenter strikes without the specified failure strain occurring.

Conversely, impacts occurring from 15° to 50° (indenter speeds of 1.635 m/s to 5.295 m/s) resulted in rupture of the grillage in progressively fewer impacts with each increased energy application. Figure 4-12 illustrates the accumulated damage pattern that occurs for varying degrees of impact after either 50 indentations or the indentation immediately preceding the panel progressing to the specified failure strain. In contrast, Figure 4-13 shows the corresponding panel-side evolution of plastic damage. In some higher energy instances, the number of impacts to rupture are equal, while the strain evolution leading up to the rupture cycle show different results.

4.1.6.2 Deformation shapes

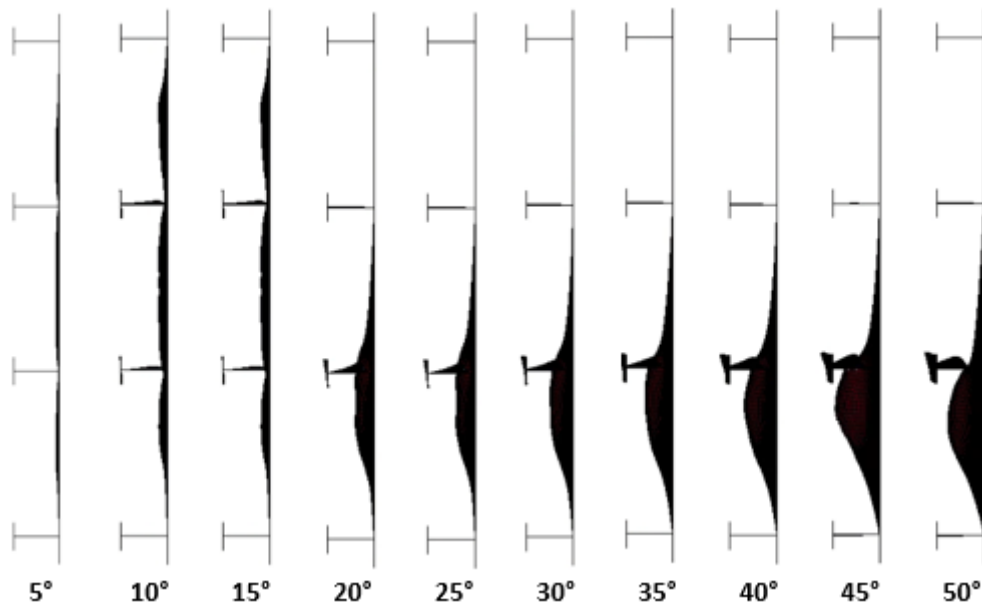


Figure 4-12. Load case #4: Accumulated damage pattern (following 50 impacts or at failure strain attainment if occurring before 50 impacts)

The deformation shape in load case four is notable due to the nature of its progression. At lower energy states, strain accumulation exhibits a shakedown-like response through the first set of impacts (the primary wave). The deformation shape assumed is a series of small but distinct indentation centers developed in all three bays of the panel with very mild overall lateral deflection of the panel, as seen in Figure 4-12. However, at low energy states (associated with impact angles of 15° or less), the introduction of the second wave of impacts is immediately discernible in Figure 4-11 as a rapid increase in plastic strain.

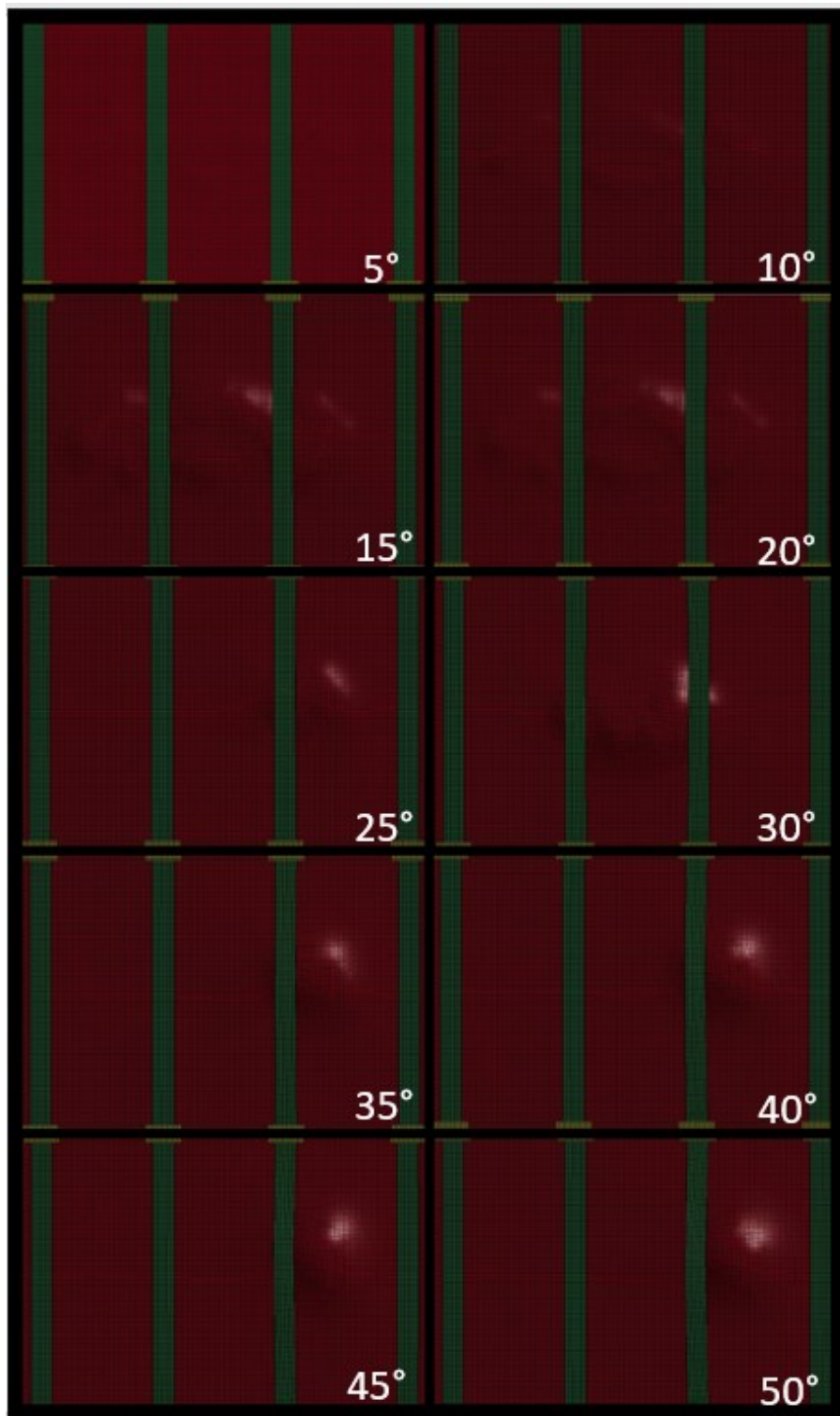


Figure 4-13. Load case #4: Accumulated damage pattern (following 50 impacts or at failure strain attainment if occurring before 50 impacts) --stiffener view

With further increases in the magnitude of applied impact energy, the multi-bay deflection pattern ceases to develop as the number of impacts to rupture is too few to allow an impact into the third bay. Instead, the impact magnitude is adequate to generate significant plasticity in the stiffener as a result of impacts to the panel, which are anywhere in the immediate vicinity of the stiffener. The development of buckling behavior in the stiffener similarly expresses itself at higher energies. A significant strain increment occurs with the initial impact, followed by a plateauing behavior as the impact site translates laterally. Upon impact in the vicinity of, or on the stiffener (Figure 4-13), the structure's ability to resist deformation is compromised. Consequently, rapid strain growth is experienced growing unchecked with subsequent impacts until rupture occurs.

4.1.7 Load case 5

4.1.7.1 Accumulated plastic strain of models

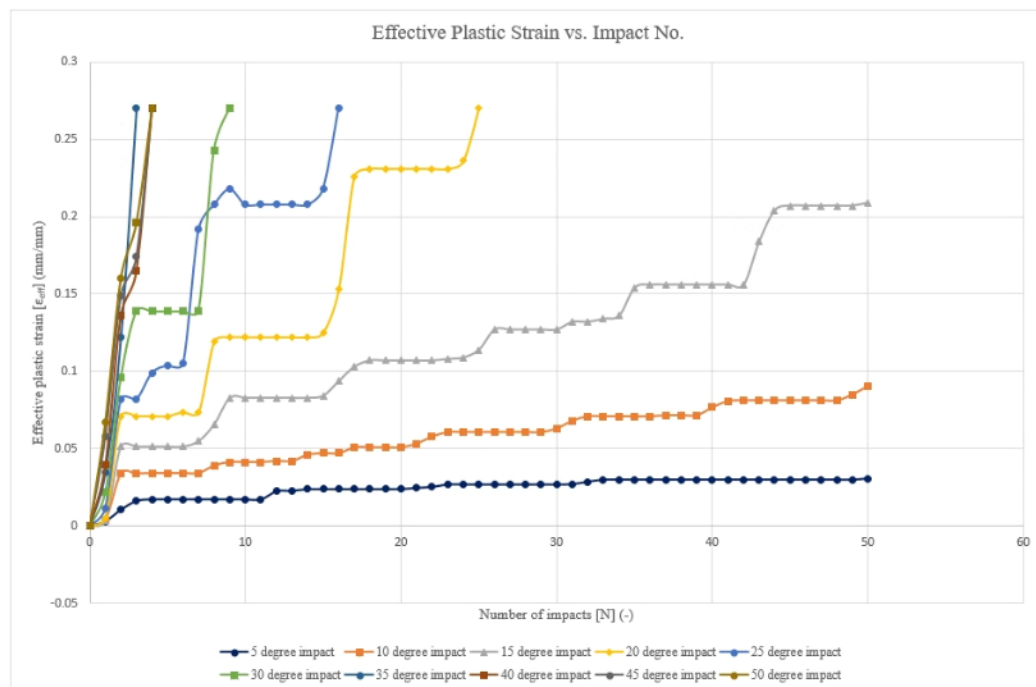


Figure 4-14. Load case #5: Effective plastic strain versus impact number

Load case five bears a similarity to load case 3 in that a series of impacts are introduced originating at one inner transverse stiffener, proceeding across the face of the panel to a second inner stiffener. The first strike occurs in the horizontal and vertical center of the left inner transverse stiffener, and the impact pattern proceeds across the lateral face of the panel pattern. Unlike load case 3, load case five introduces impacts within the impact crater of each previous strike, thereby introducing a different case to the load history. The impact pattern is depicted in Figure 3-52. A total of 50 impacts were applied to the panel in each instance (excepting when less than 50 strikes were required to induce rupture in the panel).

Examination of Figure 4-14 reveals that impact scenarios between 5° and 15° (indenter speeds of 0.546 m/s to 1.635 m/s) survived 50 indenter strikes without the specified failure strain occurring. Conversely, impacts occurring from 20° to 50° (indenter speeds of 2.176 m/s to 5.295 m/s) resulted in rupture of the grillage in progressively fewer impacts with each increased energy application. Figure 4-15 illustrates the accumulated damage pattern that occurs for varying degrees of impact after either 50 indentations or the indentation immediately preceding the panel progressing to the specified failure strain. Figure 4-16 shows the corresponding panel-side evolution of plastic damage.

4.1.7.2 Deformation shapes

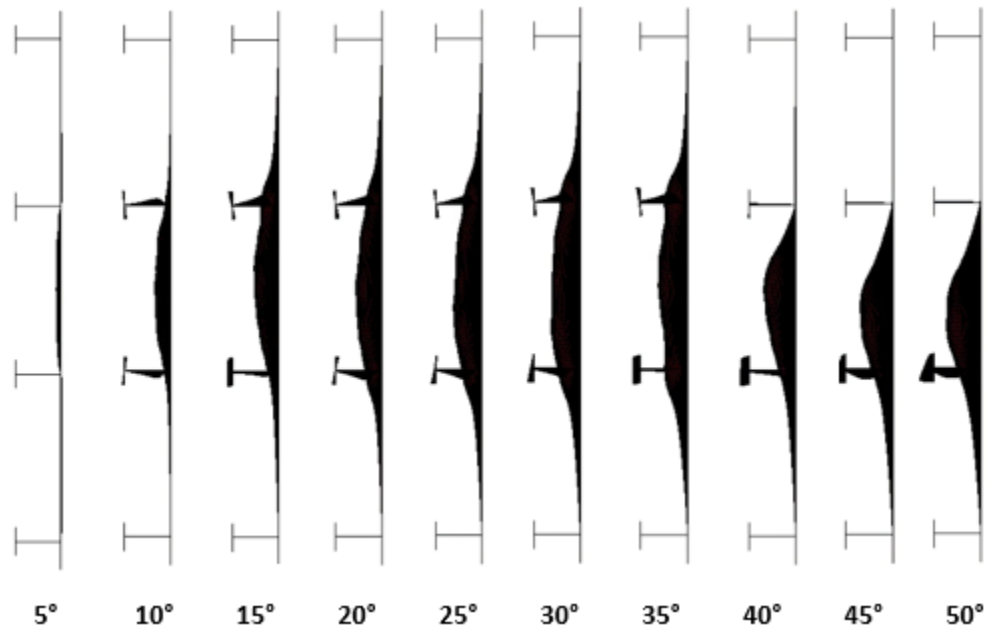


Figure 4-15. Load case #5: Accumulated damage pattern (following 50 impacts or at failure strain attainment if occurring before 50 impacts)

Figure 4-15 displays a range of deformation patterns associated with multiple progressive accumulation patterns. Generalizing the trend in behavior, with each sub-case of increasing energy, a progressively broader and deeper indentation site develops. The overall damage site is characteristically similar to the evolution of damage exhibited in load case three. For context, it is essential to note that the significant distinguishing aspect of the two load cases is that load case three introduces subsequent impacts towards prior impacts' peripheries, while load case five instantiates the impacts more centrally within each impact crater. The nature of impact is particularly notable for sub-cases with energy levels associated with greater than 20° impact angle. The inspection of Figure 4-14 in these ranges depicts a pronounced stepped response. From the data, it is noted that a primary

impact leads to a strain increment and is then commonly characteristically followed by several non-growth impacts as the impact pattern is applied laterally away from the first strike site.

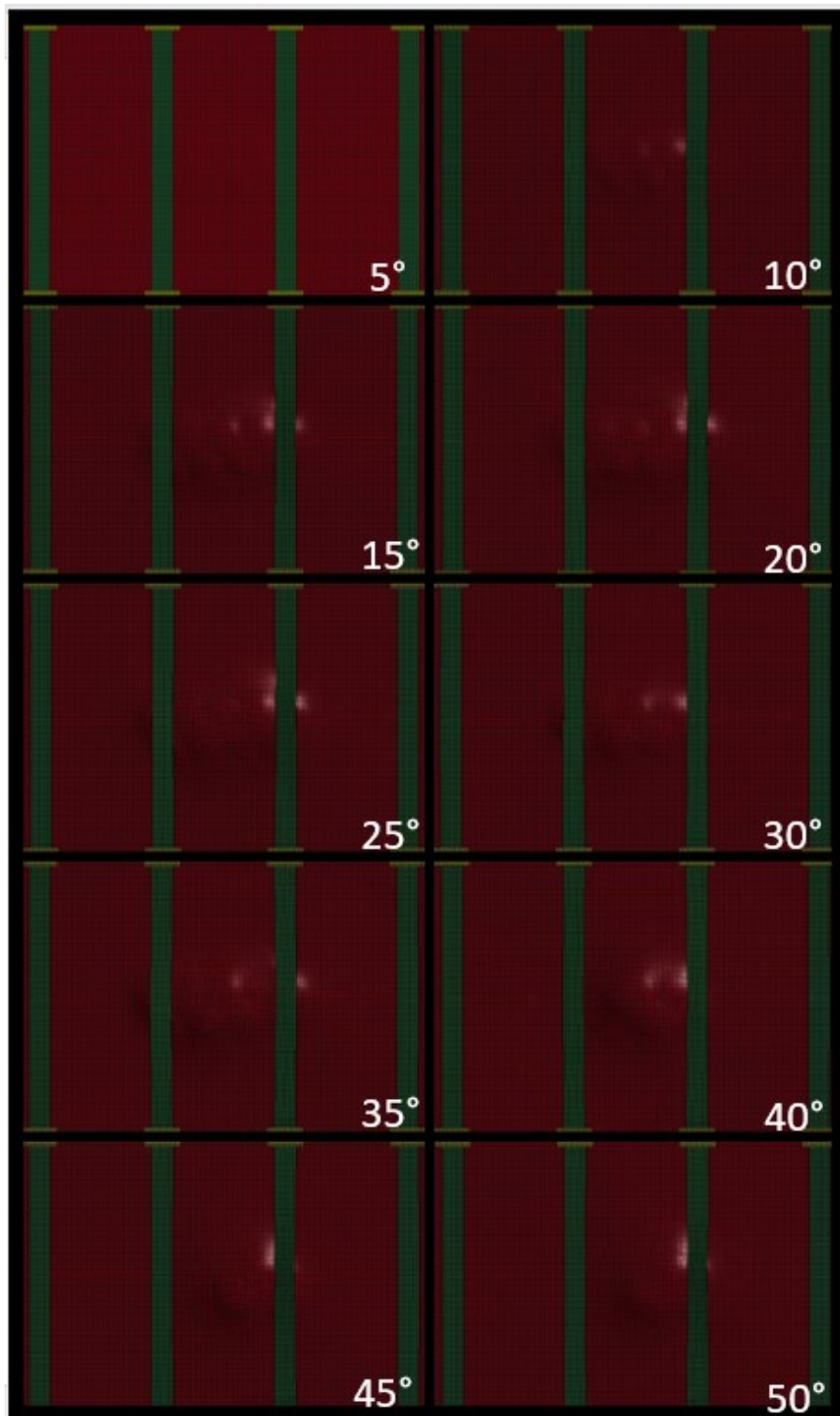


Figure 4-16. Load case #5: Accumulated damage pattern (following 50 impacts or at failure strain attainment if occurring before 50 impacts) --stiffener view

Although the maximum plastic strain does not grow during this series of impacts, the continued deflection of the structure is visible by way of the developed impact pattern displayed in Figure 4-15. After a series of non-growth strikes, an application of the indenter to the field in the vicinity of the initial strike point of a given series induces an additional strain increment. As the energy magnitude increases by sub-case, the number of non-growth impacts between strain increments decreases, providing evidence that both the pattern of energy application and the magnitude of the applied load influence the nature of the structure's governing response. The impact end-states displayed in Figure 4-16 reveal a lack of transverse bending (a bowing shape along the longitudinal axis of the stiffener) while the overall structure continues to develop incremental plasticity. The finding is consistent with observed behavior in the variant load case three and amplifies that the buckling capacity of the stiffener is a significant contributor to the development of ratchet or shakedown mechanisms in the grillage.

Chapter 5 DISCUSSION AND ANALYSIS

Chapter 5 describes an interpretation of the results presented previously in Chapter 4 aimed at identifying plasticity behaviors that occur and how these behaviors develop under an increased application of energy and vary with impact pattern.

5.1 Individual load case analysis

5.1.1 Load case 1

Examination of the plastic strain accumulation by load cycle suggests elastic shakedown behavior when the grillage is subjected to impacts in the range of 5° - 20° (0.546 m/s to 2.176 m/s or 1.87 kJ to 29.74 kJ). Similarly, ratcheting leading to progressive incremental collapse was apparent in scenarios using energy ranges consistent with 25° pendulum impact angles and higher. Below 15° , plasticity behavior was primarily localized to the impact crater. However, above impact angles of 20° , plastic damage begins to accumulate in the stiffeners, presenting visually as bowing in the transverse-axis of the stiffener. Plastic damage to the stiffeners consistently degrades the capability of the grillage to sustain subsequent impacts. For instance, above 25° , buckling and stiffener tripping appear in the structure, and further introductions of load lead to increased unmitigated plasticity in the structure until rupture occurs.

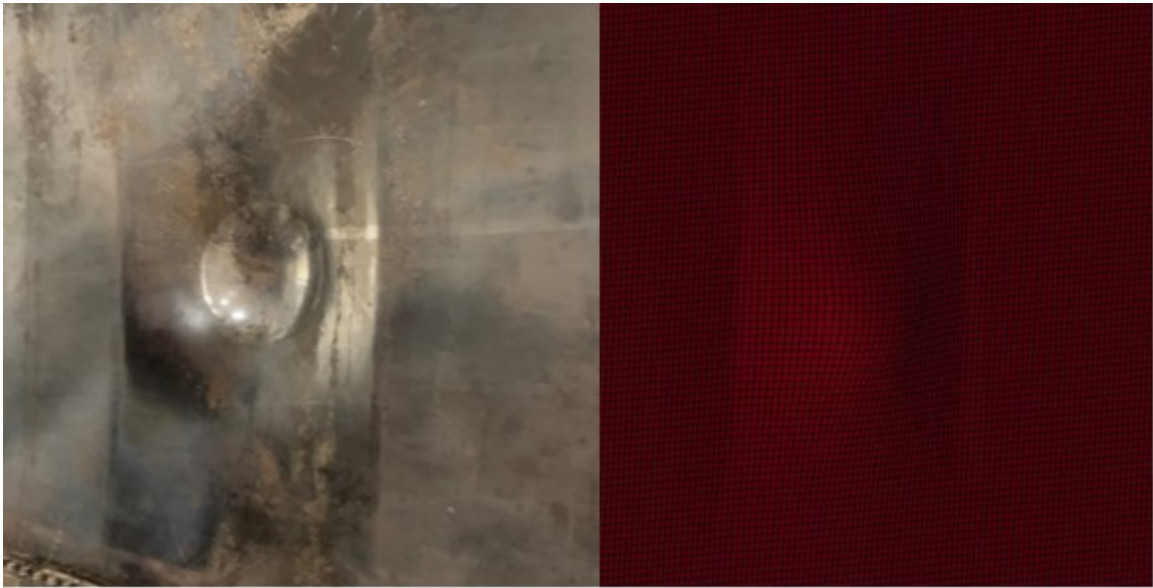


Figure 5-1. Numerical versus experimental indentation pattern after five impacts

Analysis of the indentation pattern shows progressive accumulation with each individual impact. As the impact crater grows, the material response shows the panel pulling/stretching at the inner transverse segments. The pattern after five indentations is shown as compared with that of the equivalent experimental impact in Figure 5-1. The simulated versus experimental deformation patterns show good agreement.

5.1.2 Load case 2

The second load case displays shakedown behavior quickly into its impact pattern at low energies. By examination, the widening impact area results in an accumulation of failure strain beginning at much lower energy levels than the baseline scenario (load case 1). In other words, it takes less energy input over fewer hits to create a failing condition than in the baseline scenario. At higher energies, this relationship is even more pronounced,

with the number of impacts required to induce failure strain nearly one-half that required by the baseline scenario.

The observed response was the opposite of the expected behavior. It was anticipated that widening the impact area would effectively result in an increased number of impacts at higher energies before reaching failure strain. An alternative way of looking at this is that it was assumed that repeated impacts in a single location would produce the most extreme deformation given the concentration of force over a particular area. However, the simulation results in a widened impact area creating a condition that exposes the stiffeners to higher stress earlier in the overall evolution of multiple impacts. The result is consistent with observations reported by Hertz (1882), emphasizing that with increased load, the ratio of impact crater width to depth is proportional in such a way that the width grows faster than the depth. Thus, at higher loads, the periphery of the impact site (namely the regions associated with the inner stiffeners) is involved in the impact mechanics sooner than at lower loads despite only a moderate increase in impact depth. As the stiffeners experience plastic deformation and begin to bow, and then experience web buckling, the membrane capacity of the overall grillage is reduced. Locally, the stiffener appears to act as a boundary for the panel's central bay. With that boundary compromised, subsequent impacts produce more significant deformation despite their location within an already highly deformed zone.

The behavior of the inner stiffeners is a critical observation supporting the premise of the assumptions and hypothesis behind this research. While the inspection of Figure 4-6 presents the structure as developing significant buckling behaviors in the stiffeners, Figure

4-7 exhibits virtually no transverse bending in the stiffeners. The two conditions represent a notable observation, reinforcing that current methods for the structural assessment of damage (e.g., visual hull inspection) require more stringently defined limits for multi-plane deflection behavior to account for accumulation of damage. For instance, an inspection of a grillage after a strike with the energy associated with the 20° impact angle would reveal a significant indentation to the center bay, with no significant deflection of the nearby stiffeners. However, from the numerical simulation of the conditions, it is apparent that the structure's capacity to resist a subsequent strike of higher energy is substantially reduced. Such a strike may potentially cause instantaneous buckling of stiffener webs, setting the stage for ratcheting behavior. Thus, it is insufficient to consider impacts as discrete occurrences. There is abundant evidence to suggest that the aggregate condition of the load history of the structure is fundamental to the prediction of its future performance against impact. Even structural components that appear uncompromised may have a stress history that leaves them susceptible to accumulated damage effects.

5.1.3 Load case 3

Load case three presents one of the most unique and influential cases examined. The inspection of the effective plastic strain plot shown in Figure 4-8 is of high interest when paired with the observations of Figure 4-9 and Figure 4-10. The plastic strain plot reveals a generalized performance displaying shakedown behavior quickly into its impact pattern at low energies (5° and 10°). However, a review of the mid-range energy levels demonstrates a transition behavior whereby the strain accumulates with each series of cycles. That is, a strain increment is associated with impacts on the initially struck stiffener.

By examination, the expanded contact area results in an accumulation of failure strain beginning at much lower energy levels than the baseline scenario (load case 1). The performance trends bear a similarity to other impact patterns concerning the energy levels needed to induce particular behaviors and the associated gradient of the strain development for different energies.

Unique to scenario three is the stark appearance of a complex relationship between impact energy and impact location. For example, considering the shapes and degrees of deformation presented in Figure 4-9, it is apparent that both sub-cases result in the attainment of the specified strain to rupture. However, the 50° sub-case requires only four impacts to achieve the necessary plastic strain, while the 35° case requires eight impacts. In either case, the structure fails, but the discrepancy in load history is of critical importance. The high-energy case by visual inspection alone depicts a significantly expanded damage area and explicit tripping behavior in the stiffeners.

Conversely, the 35° impact scenario shows a much smaller overall deformation of the panel. Regardless, the incidence of extra impacts is sufficient to build the overall plastic strain to a level necessary to create a rupture condition. At energy levels bracketed by these two extremes, an increasing deflection behavior is observable with an associated reduction in the number of impacts to failure. The stark visual contrast once again underscores the importance of developing quantifiable metrics for rapid assessment of hull damage due to repeated load exposure. In this load case, while multiple strikes accumulate a large damage area, the damage may be superficial and not lead to the plastic collapse of the structure. Alternatively, high-energy strikes may create conditions precipitating an environment for

a collapse while initially appearing less consequential. In this instance, merely doubling an already relatively low number of impacts is adequate to incur the same gross end-result for a grillage structure—an accumulated plastic strain exceeding the strain capacity of a component within the structure.

5.1.4 Load case 4

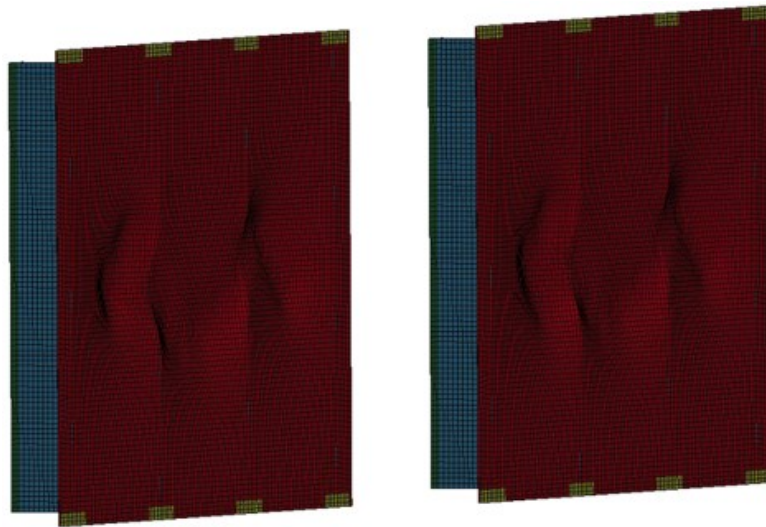


Figure 5-2. Grillage deformation leading to a pseudo-shakedown state (left); plasticity growth immediately following a pseudo-shakedown incident (right)

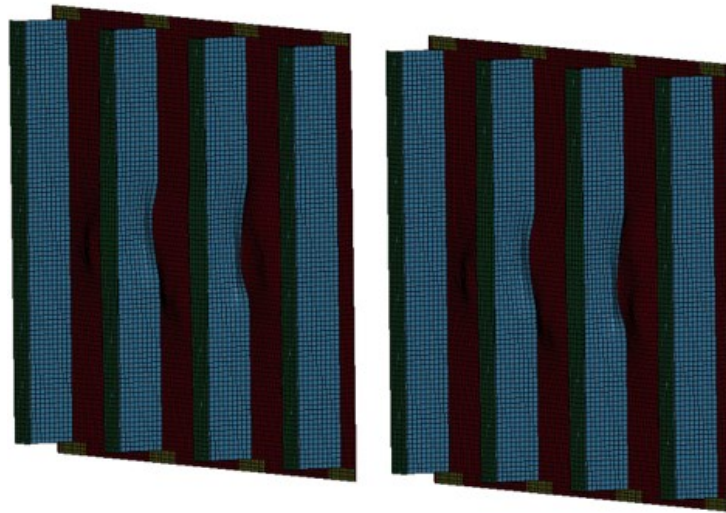


Figure 5-3. Increased stiffener plasticity following a pseudo-shakedown state

Load case four presents a continued degradation in the panel's ability to resist accumulated plasticity. This fact is evidenced by the load case's demonstration of incremental plastic collapse in eight of the ten energy scenarios applied to this load case. In load case four, an unusual pattern of behavior is revealed. After an initial deformation, an immediate "pseudo-shakedown" is apparent as the indenter travels laterally across the face of the grillage—the lateral translation of the force vector results in the grillage ceasing to respond plastically. However, with each additional impact, the overall stress continues to accumulate in the various grillage parts. When the stress accumulation is sufficient, the result manifests as an instantaneous growth in the effective plastic strain. Upon closer inspection, it is evident in all ten impact scenarios that this strain growth is precipitated by an overall reduction in the load capacity of the panel resulting from continued plasticity in a transverse stiffener, as shown in Figure 5-2 and Figure 5-3.

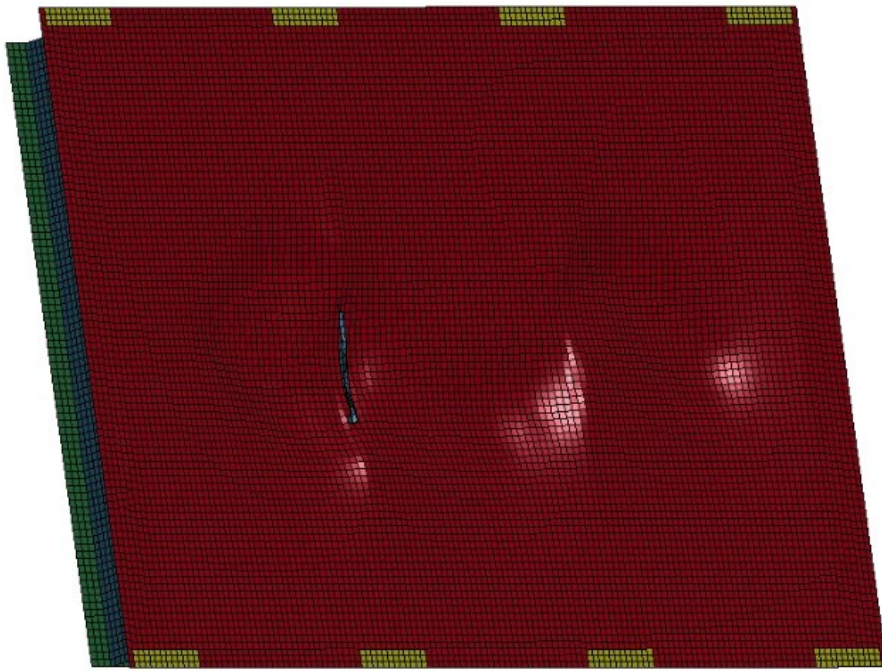


Figure 5-4. Load case #4 rupture located at the plate-stiffener connection

What marks the impact behavior as notable is that once the integrity of the stiffener begins to be compromised, continued applications of load at any location along the plate transmits in such a way as to enable continued plastic strain growth in the weakened bay of the structure (left bay). Subsequently, the overall reduction in capacity allows rupture to occur at the plate-stiffener connection, as shown in Figure 5-4. The exhibited behavior supports the claim that discrete impact sites can have significant follow-on effects for the integrity of a ship structure in other locations of the structure.

In all likelihood, the behavior observed in load case four is conservative. The reality is that in actual fabricated structure, the connection details already present a weak point of interstitial voids, heat-distortion effects, welding, and fatigue cracks, and are thus primed for concentrated stress effects. The idealized continuum of the mesh, while allowing for a

more consistent distribution of energy into the components of the grillage structure, likely presents a stiffer structure than that presented by its real-world analog. Structures with cracks and weak points deform more, creating a condition where less energy is available for plastic deformation of otherwise undamaged material. The result is that these defects may potentially increase the robustness of a structure concerning impact. Regardless, there is evidence of an inter-related compounding effect of multiple impacts. Thus, it is insufficient to view impacts as discrete instances of loading that are otherwise separate from the previous load history. Any follow-on impact on a ship structure must somehow account for the potential effects of the load history on the structure. What remains unclear is the size of the domain over which this load history is applicable.

5.1.5 Load case 5

There is a distinct pseudo-shakedown phenomenon at the six lowest energy scenarios in load case five. The overall behavior during the first two states displays minor plastic strain accumulation that trends asymptotically. In the 15° impact scenario, the pseudo-shakedown is pronounced and presents graphically as a regular series of stair-like behaviors, quite literally a ratcheting or progression of accumulated strain. After an initial impact, there are a number of non-growth inducing load applications. When the load pattern repeats, the application of load to the initial indentation site creates a strain increment. This behavior is highly interesting because it is not ratcheting in the sense of the adopted definition of strain accumulation with each cycle. It is, however, an apparent ratchet-like phenomenon in that the strain grows with each application of the loading pattern. It is unclear in this situation whether the behavior results from the load history. In

other words, does the strain increment occur as a result of stiffener damage in the initial location?

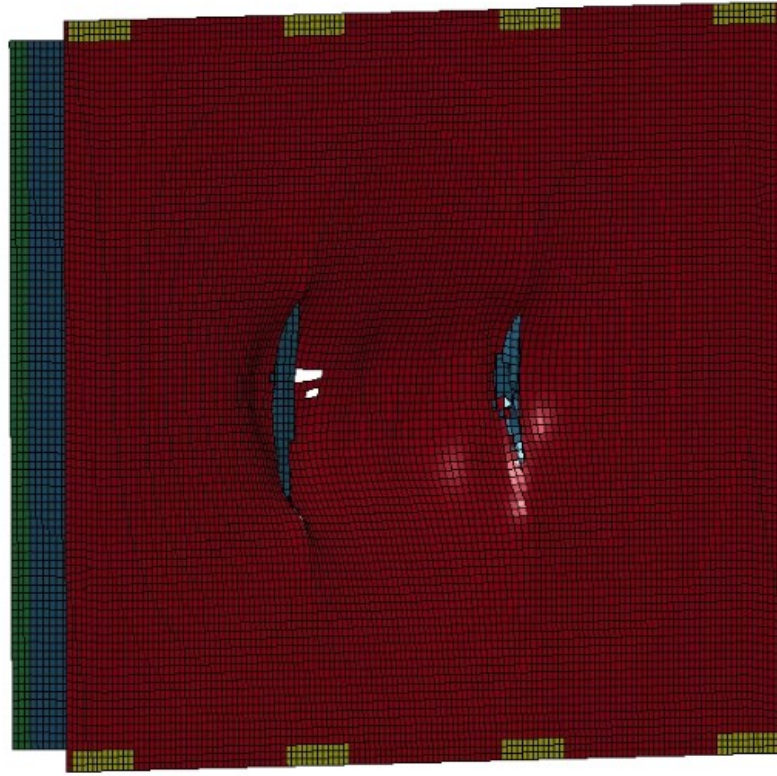


Figure 5-5. Load case #5 rupture located at both plate-stiffener connections

Failure initially occurs in load case five at the intersections of both inner stiffeners with the plate, as shown in Figure 5-5. As the failure progresses, rupture develops along the mid-line of the plate. Unlike other load scenarios presented, the rupture expands horizontally across the plate towards the stiffeners as opposed to vertically, as seen in load cases where initial rupture in the plate field was not precipitated by failure at the stiffener-plate intersection.

At increasingly higher load applications, there is little evidence of shakedown behaviors. Rather, the applied load is so significant that within the first few impacts, a failure of the stiffeners consistent with Paik's definition of a Mode III failure occurs (Paik, 2018). The deformation and subsequent failure reduce the load capacity of the grillage and rupture is induced in the plate field.

In many ways, load case five represents one of the most applicable investigations undertaken in this research. The overall indentation pattern bears a resemblance to an object or objects repeatedly striking into a progressive cavity along the length of a ship as the vessel progresses through the water. Many realistic naval scenarios align with this. For example, a ship progressing through a small ice field in the Arctic or Grand Banks, or encountering a series of wood debris hazards in the Georgia Strait. Consequently, in many ways, load case five presents an exciting application of where accidental limit states may be of value. The proximity of the indenters in load case five creates a scenario in which the indentation crater is essentially pounded out along the length of the panel. The results at high impact energies underscore the importance of recognizing that when the initial strike causes plasticity, despite the strain hardening in the immediate vicinity of the impact, there is substantially increased risk that any subsequent strike within a specific material domain is capable of inducing accumulated plasticity effects.

5.2 Similarities across load cases (performance trends)

Across all five load cases, numerous performance trends can be intimated. The first of these trends is the performance regions. In general, each load case demonstrates three primary categories of behavior that distinguish themselves by energy input. These regions

of behavior might be termed a primary shakedown region, a secondary pseudo-shakedown transition region, and a tertiary ratcheting region. In the primary region, repeated impact behavior results in plastic strain accumulation that trends asymptotically after a relatively few cycles of load application. In the secondary region, the structural behavior may manifest as a series of cycles of plastic strain followed by a number of elastic responses before an additional plastic strain increment occurs. This behavior may increase or decrease the magnitude of the plastic strain increment and may or may not result in plastic collapse depending on the number of cycles under consideration and the nature of the applied load. The tertiary region results in incremental plastic accumulation resulting in a failure mechanism within only a few cycles of load application. The strain growth is present to some degree in each cycle. If the energy inputs are qualitatively bracketed into low-, medium-, and high-energy groups, low-energy groups can be associated with primary region behavior; similarly, mid-energy groups are associated with secondary region behavior; and, high-energy groups may be associated with tertiary behavior.

A comparison of load cases in which the plate is the initial strike focus, versus load cases exploring stiffener response reveals that initial impact with stiffeners universally reduces the capacity of the structure to dissipate subsequent impact energy. This is somewhat counter-intuitive. Conventional wisdom suggests that the strongest point of a structure should be capable of sustaining the highest loads and therefore act as the point of a structure most appropriate to resist impact loading. While this may be true from a static load perspective or individual load application, its relevance appears to be somewhat limited to failure consideration of a single component. In other words, the plate-grillage

configuration is a strong-link structure. While the stiffener represents a significant structural component providing strength to the structure, when the structure is considered in its entirety, it is revealed that degrading the capacity of the stiffeners creates a significant weakness in the overall structure's capacity to bear load.

A more traditional view of strain-hardening behavior posits that a structure quickly shakes down to linear-elastic behavior when exposed to plasticity. The shakedown is attributed to the increased elastic capacity obtained by the structure in the expansion/translation of its yield surface. However, the five load cases presented suggest that this model only fits well for small-strain effects where the primary constituent in the stress response is in the elastic range, and the residual stress after unloading the structure is small. When large plasticity effects dominate the structural behavior, the residual stress after unloading the structure appears to provide a mechanism to more easily achieve the level of stress in subsequent loadings necessary to continue accumulating plastic strain.

5.3 Experimental uncertainties

Errors will permeate experimentation regardless of the care exerted in the conduct of the experiment. While some of these errors are random, others are due to gross errors resulting from the trials and tribulations of the first-conduct of an experiment or apparatus. The uncertainties associated with this investigation primarily constitute uncertainties resulting from the conduct of the physical experiment used for model validation, and uncertainties in the numerical model methodology. Several of the known or suspected uncertainties are expanded below.

In general, the uncertainties identified fall within two broad categories, aleatoric, or random uncertainty, comprising unknowns that differ with each run of the same experiment, and epistemic, or systematic uncertainties that are composed of factors which an experimentalist could possibly know but ignore or fail to capture in practice. Within these classifications, a number of uncertainties present themselves throughout this research including, parameter uncertainty, parametric variability, structural uncertainty or model discrepancy, algorithmic uncertainty, and experimental observation uncertainties. To better encapsulate the structure of the most prevalent concerns within the research, these issues are segmented into physical experimental uncertainties and numerical experimental uncertainties.

5.3.1 Physical experimental uncertainties

A number of contributing socio-political issues influenced the conduct of the physical experiment during its proposed timeline. The consequence was that some experimental data originally sought for collection was unavailable, and the experimental window was shortened. Chief among these contributing influences was the onset of the worldwide pandemic created by the novel COVID-19 virus. Closures of experimental facilities precluded the entirety of the test window originally programmed for February-August 2020. The result was that the experimental validation data was limited to only four test impacts. The initially intended test program called for impacts to be conducted until one of the specified termination criteria outlined in Chapter 3 was achieved. Moreover, the shortening of the experimental window prevented experimental observations over multiple

test specimens, which would have provided cross-validating data to help understand and assess the magnitude of physical uncertainties.

5.3.1.1 Instrumentation

The pendulum apparatus used in the experiment is configured to incorporate three piezo-electric load cells mounted on the backing plate behind the indenter. The load cells were not able to complete their calibration prior to the initial experiments that yielded the data used for numerical model composition. Subsequently, impact force data was not available against which to cross-validate the numerical contact force. Moreover, as this was a proof-of-concept experimental test, many other sensor types, including strain gauges and ultra-high-frame-rate video capture, were not calibrated and installed when the tests were carried out. This would have acted as a highly preferred way of validating the performance of the numerical model through the ability to capture real-time strain data, as well as the rebound velocities of the indenter and panel pendulums. Without this information, it is difficult to make a true assessment of the experimental energy inputs, and many assumptions (such as impact velocity of the indenter) were made via good, but rudimentary, geometric and trigonometric simplifications. In place of the sensor data, the only means of validation was the recorded panel deformation which was used to validate against observed numerical model deformation. Instrumentation error, including panel deformation measurements are epistemic errors which could have been quantified by repeating the measurements multiple times employing the same equipment settings.

5.3.1.2 Boundary conditions

Every effort was made to produce rigid, clamped/fixed boundary conditions in the physical structure to simplify numerical modeling and attempt to reflect the true physical experimental environment as closely as possible. However, there is no true means of ever creating a physical boundary that is as stiff as that present in the numerical environment. It was assumed that the bolts and backing bar used in the plate mounting arrangement was strong enough to prevent pull-in of the plate edges and stiffener ends in the experiment. While this assumption may or may not have been accurate, a more significant issue is the problem of boundary elasticity. The initial construction of the pendulum frame was assumed sufficiently robust so as not to experience large magnitudes of elastic or plastic deflection when high-energy impacts were applied to the panel. After testing, an inspection of the test frame showed elasticity consistent with significant axial compression of the panel. Thus, as the panel was repeatedly stressed, the compressive action of the panel pulled-in on the test frame, creating both translation and rotation of the “stiff” boundary.

The degree of deformation could not be estimated at the time of testing and thus could not be reliably accounted for in the numerical model. The existence of this fact may explain some of the discrepancies between the numerical observations and experimental observations observed in later impacts in the validation model. However, through experimental observation of the variability of experimental measurements, an estimate of the contribution of this uncertainty might have been quantifiable to some degree through observation of the boundary effects occurring across multiple test panels.

5.3.1.3 Pendulum apparatus degradation

After the third validation impact, an observable drift of the impact crater was viewable in the test panel, as previously discussed. However, it was not until an inspection of the pendulum test apparatus after impact four that catastrophic failure of the pillow-block bearing housings supporting the pendulum arms on both the indenter and panel-side pendulum arms was discovered. The causal chain creating this failure stemmed from a pre-existing rigid braking system designed initially for testing involving much smaller rebound energies. As a result, a lack of an energy absorption mechanism in the braking system permitted failure at the most brittle component of the brake system (the cast iron bearing housings), allowing the energy to dissipate through motion against gravity. However, experimentally it raises an interesting uncertainty. A pronounced bowing was observable in one stiffener before the other. The asymmetric bowing condition raises the question as to whether a material failure in the stiffener permitted preferential impact towards it? Or, did the bearing caps break, permitting the indenter to develop a rotational out-of-plane motion, causing the indenter to drift horizontally and allowing a moment to develop during impact with the panel?

In the numerical validation, the stiffeners are considered a material continuum that responds equally to load without a predisposition for failure in one stiffener versus the other. Thus, the numerical model adopts the second scenario. In this regard, the simulation models impact three and impact four as a two-direction translating hit with the total indenter speed the resultant composition of two components, a forward and sideways motion. The nature of the physical experimental error is highly aleatoric. It would be

difficult to quantify its contribution to the experimental error given the randomness of the failure, and the inherent randomness of excitation and vibratory or rotational motions experienced by the indenter as a result of its travel path in a less-secure bearing housing.

5.3.1.4 Omission of contributory energy sinks

At the time of experimentation, no capacity existed to assess the magnitude of sliding friction in the experimental set-up. Subsequently, friction was omitted in further analysis to avoid introducing spurious unverifiable factors into the evaluation of grillage behavior. Additional energy sinks such as heat generation and noise effects resulting from the indenter impacts were not considered. However, physical observations post-impact such as the galling observable on the indenter and the observation of significant warmth emanating from the panel when touched by experimenters is indicative that the two aspects may not be trivial in refining the energy balance of an impact compared to its numerical partner.

The omission of energy sinks is a common epistemic uncertainty in which minor observation errors could be measured and incorporated into models and analyses, but are often neglected because the measurements are difficult to capture in the context of the experiment or because their omission simplifies subsequent modeling. The energy sinks identified herein could be a set of quantifiable uncertainties, but given the test set-up at the time the test program was run, were unable to be captured for inclusion at the time.

5.3.1.5 Pendulum impact speed

Original applications of the double pendulum apparatus concerned themselves with single impact events (Gagnon et al., 2015). Experimentation involving multiple

indentations initially failed to account for lost energy in follow-on impacts due to pendulum speed reduction. The pendulum is configured to allow the contact surfaces to strike as each pendulum ideally reaches the bottom of its motion (assuming equal pendulum lengths, weights, and release times) while maintaining a horizontal impact. However, after the initial impact, deformation in the panel effectively increases the horizontal length of the path that the two arm sets must travel in subsequent impacts. The two pendulums must swing past the bottom of their arcs to overcome this gap, at which point they begin losing speed as kinetic energy is transferred back into gravitational potential energy while the pendulum gains height along its arc.

The described effect is present for each impact following an impact in which deformation has occurred. The effect, however minute, is that in each follow-on impact, the indenter is impacting at a slightly decreased velocity, losing energy exponentially at a rate squared to that velocity loss. The consequence is a need for precise measurement of impact velocity to correlate against impact damage. The investigation discussed in this thesis uses a gross approximation of that speed derived from energy conservation methods and trigonometry. The uncertainty is certainly quantifiable and incorporation of improved physical measurement using high-speed video capture and correlation devices could lead to superior applications in a refined numerical model.

5.3.1.6 Stress-strain test

The material parameters determined experimentally may not be most appropriately suited for subsequent incorporation in a numerical model. While the test method followed an acceptable protocol outlined by ISO Standards (2018), the test is well-validated for

monotonic loading. However, numerous sources (Dowling, 2007; Hübel, 1996; Jones, 2014) suggest that a laboratory test that characterizes cyclic stress-strain behavior during low-cycle testing by producing a stress-strain curve obtained by overlaying the tips of superimposed hysteresis curves from a cyclic loading procedure may produce a more appropriate curve for any low-cycle repeating event. While this variation of material parameter estimation is not yet widely applied in repeated impact events, its potential for aiding in the explanation of multiple impact behavior merits further consideration. The uncertainty contribution of such a variation could be calculated against the more common test variant provided a sufficient number of coupons were tested in each mode.

5.3.2 Numerical experimental uncertainties

Numerical uncertainties in this investigation were primarily constrained to modeling choices. In particular, choices made concerning the inclusion of friction and damping, as well as the underlying mathematics of the material model, create a degree of uncertainty in the analysis. In this fashion, the numerical uncertainties are largely that of parameter uncertainties in which exact values for FEA material properties could not be known and controlled in physical experiments. Similarly, parametric variability such as variations in the composition of physical experimental test panels create a discrepancy with the continuous material mesh of the model. Furthermore, algorithmic uncertainties inherently lead to numerical errors and approximations in a double-precision finite element solver.

While some of these errors such as friction, damping, and strain-rate sensitivity might be quantified by incorporating specific and unique test data targeted to derive

estimates for these values appropriate for the experimental context, many other numerical uncertainties are unquantifiable. In fact, as expressed by many of the leading voices of ratcheting research, the importance of wide-spread and varied numerical simulation of ratcheting effects employing a range of conditions is to expand the landscape for researchers. This expansion and the experimentation that undergirds it is a direct effort to identify where the numerical uncertainties have the most significance as it relates to an accurate description of the physical world.

5.3.2.1 Friction

Without an empirical value of friction from experimental tests, friction was omitted from the numerical model. It was felt that the introduction of a friction value would introduce unidentifiable uncertainty in the model versus a known uncertainty. Thus, revisions of the model can assess against the introduction of reported friction values for acceptable fit, permitting a quantification of the uncertainty now that a frictionless baseline performance has been identified and investigated.

5.3.2.2 Damping

The repeated impact numerical load cases were simulated without damping effects. Initial tests to the sensitivity of the grillage structure were conducted to assess the effect of elastic vibrations. Mass proportional damping was used at the lowest natural frequency of the model and updated after each impact to use as the initial condition for a subsequent impact. The computational cost and model production time was so intensive relative to the effect on residual deformation, stress, and strain patterns of the undamped structure that it was determined sufficient to assess characteristic behavior without the introduction of

damping. A more refined model might conduct a resonance analysis of the actual experimental panel in the post-impact condition, and apply these fundamental frequencies to a numerical model to derive increased accuracy in the results. However, the natural stiffness of the structure is so great that the gross behavior of the impact does not fundamentally change due to inclusion or neglect of damping.

5.3.2.3 Geometric model

The geometric model used for numerical analysis neglects the effect of welds at the stiffener-panel intersections. Zhu et al. (2018) attempted to model welds with elements of increased thickness, while Liu and Quek (2013) advise that it is easy to introduce fallacies into a numerical model without specialized knowledge of weld behavior. Meanwhile, Paik et al. (2003) informs readers that welds can represent a key failure point in grillage structures. However, the model investigates the behavior as if the panel and stiffeners are one continuum, cognizant that this likely decreases the stiffness of the model in comparison to the weldments present in the actual structure. Welds are generally full-penetration welds, and thus the stiffener-plate join is solid steel contributing a significant addition of material which FEA modeling ignores.

5.3.2.4 Strain rate sensitivity

Numerical sensitivity tests in numerical material model selection revealed that inclusion of strain-rate parameters produced consistently poor results compared to experimental testing. Jones et al. (1970) as cited by Zhu et al. (2018) finds that the influence of material strain rate sensitivity may be reduced in biaxial and multiaxial loading states versus experimentally observed values in uniaxial testing. To prevent spurious correlations

from being formed in the analysis of the numerical model performance, strain rate effects were omitted. However, it is widely reported in the literature (Paik et al., 2003) that mild ship-building steels do, in fact, show sensitivity to strain rate in sub-ballistic impact experimentation. A valid strain-rate parameter from experimental testing of material coupons of the test panel would be a valid means of quantifying any uncertainty in this assessment resulting from strain-rate effects.

5.3.2.5 Hardening model selection

Many mathematical descriptions that address ratcheting effects employ an NLKH rule to define the development of the yield surface (Abdel-Karim, 2009; Chaboche, 1989; Chen et al., 2005). However, initial investigations of structural behavior often begin with a simplified inelastic analysis to characterize and generalize observed behaviors qualitatively before attempting to deconstruct complex loadings and structures analytically (Bree, 1967; Hübel, 1996). In this instance, electing to employ an isotropic hardening model may exaggerate plastic accumulation by preventing the development of back-stress, and the subsequent development of reverse plasticity, during the unloading half of a cycle.

It was initially posited that the stress developed during the load cycle combined with the structural stiffness of the grillage would be so significant that reversed plasticity would be negligible at best. The model, as employed, has value as a baseline against which to evaluate a future NLKH model for the influence of back-stress on plasticity development. Such an evaluation, conducted across numerous models would be a necessary first step in quantifying the uncertainty contributed by the selection of a given hardening model.

5.3.2.6 Simplification of the model to a one-way, rectilinear impact

The experimental test apparatus features two pendulums swinging on opposing paths, intersecting at the bottom-most portion of their paths. By their very nature, the paths traced are arcs. In the numerical space, the portion of the motion that is of interest is the moment immediately preceding, through to the moment immediately following, impact. The model was simplified by treating the motion as rectilinear throughout the space. High-fidelity modeling of the dual pendulum apparatus' motion was conducted separately from the direct research of this investigation by Quinton (personal communication, 2020). Quinton finds that a rectilinear speed/contact path assumption is valid for the dual pendulum collision. However, it is worth noting that experimentation involving repeated collisions may create an uncertainty associated with the added travel path created by deformation, as explicated in section 5.3.1.5.

A second simplification of the model was made by limiting the number of moving components in the model. While the experimental test apparatus featured both an indenter-side and panel-side pendulum meeting in a collision, the numerical model employed a stationary panel, rigidly constrained in several degrees of freedom, and a mobile indenter with an increased mass component equivalent to the total system mass in the experimental apparatus and an equivalent closing velocity. The simplification was instituted to facilitate the use of multiple impacts in a single test run. Employing the simplification in this manner ensured the collision energy was kept equal between the experimental and numerical models.

A series of confirmation runs were conducted using various impacts of various energy magnitudes in the one-way model and a model that was identical concerning part composition and identification, but featuring appropriate mass and speeds assigned to both the indenter and panel-side structures. Plots of force-displacement, plasticity growth, and individual directional translation of elements were comparable. Consultation with more experienced modelers further supported the adoption of this simplification. However, the results were checked against single impacts. Thus, the degree of any compounded discrepancy that would result from applying the simplification in a repeated impact context, is unknown. The uncertainty could be quantified and assessed in the same manner as that described for the single impact rectilinear model.

Chapter 6 CONCLUSION

Chapter 6 presents a summary of the major findings of the research outlined in this discussion and re-visits the original hypothesis governing the direction of research in the context of providing a ruling on posited behavior. Moreover, the chapter details several questions that arose during, or as a result of, the research and warrant further study.

6.1 Summary of Findings

The load cases presented in Chapter 5 indicate that plastic strain accumulates over a number of cycles. Plasticity may cease its accumulation in as little as the first half-cycle, or it may progress with either increasing or decreasing magnitude unchecked until the plastic accumulation (plastic strain) reaches that required to induce failure. Many accumulated plastic damage phenomena occur in a uniaxially-stiffened grillage depending on the load amplitude and loading location. The phenomena observed include elastic shakedown, pseudo-shakedown, and ratcheting leading to progressive plastic collapse. Lower-energy loads were associated with elastic shakedown and an asymptotic accumulation of plastic strain. Alternatively, mid-energy loads may result in a pseudo-shakedown behavior that may, or may not, result in attaining failure strain within an ultra-low cycle frequency range depending on the impact pattern presented to the grillage. At all energy levels examined, initial plastic damage directed through the stiffener contributes to a significant weakening of the energy absorption capacity of the surrounding structure.

The assumed shape of deformation in both the directly impacted and surrounding structure performs counter-intuitively. While it was initially posited that repeated impacts to a coincident location would result in the worst-damage case, experimental observations

suggest that progressive damage radiating in any pattern from an initial strike location produce a weakened structural state. This weakened state is likely due to a progressive introduction of damage to partially damaged and partial virgin (undamaged) material in the structure. As a result of the progressive damage, the capacity of the structure to withstand additional impact is compromised, resulting in increased plastic accumulation. A uniaxially-stiffened warship grillage is capable of withstanding accumulated damage due to a load. However, a caveat to this conclusion is that at higher energy level impacts, this plastic accumulation proceeds cyclically until failure. Depending on the indentation pattern, the mode of failure may be stiffener buckling, gross yielding in the plate field, or a combination of both.

6.2 Conclusions

The investigation herein proposed the use of a simplified impact experiment based on an isotropic, multi-linear hardening model. The experiment intended to characterize the dynamic response of a uniaxially-stiffened warship grillage in a fully clamped condition, subjected to repeated impacts from a smooth, spherical indenter over a broad range of locations. The numerical model was developed using the commercial software package LS-DYNA and validated against physical experiments using a dual pendulum apparatus. Observation of the permanent deflection of the test specimen showed good agreement with the numerical simulations performed for the same loading scenario.

The application of a variety of themed load cases, all variations on the initial scenario, allowed the exploration of the problem space, revealing evidence of the presence of a number of hypothesized possible behaviors in the overall structure. There appeared to

be several salient parameters that influence the structure's behavior. The most significant relationship appears between the applied energy and the impact location. The investigation suggests that when considering accumulated plastic damage effects, preliminarily introducing damage to reinforced areas of the structure creates conditions favorable to promote the onset of accumulated plasticity. However, the interface between these two parameters is as-yet unclear. Similarly, while strain hardening behavior exhibited by a material influence the accuracy of numerical predictions, accounting for ancillary contributory effects such as strain rate, friction and damping remain unexplored. What is clear is that for fidelity in numerical simulation, material effects such as strain rate parameters and material defects are secondary mechanisms in comparison with ascertaining measures of the applied load magnitude and location.

6.3 Acceptance or refutation of hypothesis

In conclusion, it was determined that when a region of interest within a notionally similar ship structure is exposed to repeated, cyclic impacts, the structure will exhibit a shakedown response over a range of low-energy (small strain) scenarios. However, there is sufficient evidence to suggest that the cyclic behavior of high-energy impacts will lead to the progressive, incremental plastic collapse of a structure. Thus, consideration of ship damage, ship fatigue, or ship life cycle scenarios that fail to incorporate the previous loading history of the material may substantially overpredict the performance of the structure.

6.4 Implications for research

The results obtained in this study appear to support observations of pseudo-shakedown phenomena and shakedown behaviors observed and reported by Zhu et al. (2018) as well as Zhu and Faulkner (1996). Consequently, the numerical simulations produced by this research can, and do, provide deformation profiles for the permanent deflection of a uniaxially-stiffened grillage subjected to multiple impacts. Moreover, the findings indicate that a simplified numerical model can, and should, be used to assess the response of accumulated damage scenarios for ship structures. The results of the study provide useful information for design considerations in the developmental stages of the design for a plate-stiffener structural configuration.

The generic indenter and indentation plan applied in this study has implications for myriad scenarios involving repeated impacts including, but not limited to: dropped object (cargo loading scenarios), allision and collision states, and repeated impacts from ice or other debris fields. Plate-stiffener configurations have a fundamental difference in their response under repeated impacts from comparatively large magnitudes of kinetic energy than these same configurations do under low kinetic energy exposure. Moreover, the response of repeated load applications shows variation compared with that observed in static or single-impact application loads. Design guidance must be developed and updated to reflect the discrepancy in damage accumulation under repeated load states to reflect better the realities of ships' and offshore structures' lifecycles.

6.5 Limitations

The observed behavior was noted for a relatively limited application of isotropic hardening conditions built on a uniaxial, monotonically-derived material model and validated across comparatively few full-scale impacts. Thus, the expansion of the model to cycle applications in the range from 10^0 through 10^2 remains as-yet not validated. While provisions were made for force and high-speed digital image correlation film capture, the inability throughout the test break-in period to reliably capture the force data and indenter carriage rebound velocities coupled with the interrupted experimental plan limits the accuracy of estimations of elastic strain energy absorbed by deformed structures. Thus, the simulations discussed are primarily confined to the observance and expression of displacement profiles and qualitative post-yield plasticity behaviors. It has been previously suggested (Paik et al., 2009; Zhu et al., 2018) that the shape of the deformation mode provides a definite first step in the development of theoretical solutions describing grillage behavior. However, given the mode's significant influence on a solution's accuracy, many parameters of interest remain to be captured so that a robust theoretical or analytical description of the damage accumulation can be accurately formulated.

The experimentation has been restricted to a comparatively small section of a ship structure in an artificial boundary. Applications of the conclusions of this research may not scale to a larger, less-stiff plate field such as that of a ship's hull. Finally, the conclusions proposed are devoid of consideration of any interrelationships between a grillage and other secondary and tertiary structure, as well as, structural details such as weldments, or the contributory influences of other latent secondary loads or induced stresses in the structures

and components. Thus, while the inferences and suppositions made from the experimental findings provide many valid considerations for inclusion in preliminary design work, it would be inappropriate to speculate on detailed design guidance, and rule-based codification cannot be extrapolated from the findings in their current state.

6.6 Recommendations and future work

Regardless of the voluminous work already ascribed to researchers in the field of accumulated plasticity, the field remains largely in its infancy. Several essential questions are outstanding to improve an understanding of ratcheting, and ratchet-like behaviors and their implications for the design of engineering components and engineering structures. The work conducted through the presented research requires validation through a full suite of full-scale experimental tests. Buttressing this analysis might begin with material testing using both an ASTM cyclic testing procedure as well as a bi-axial application to generate material stress-strain curves that could conceivably better reflect material behavior over multiple cycles. Armed with revised material data, and a complement of experimental impact data, the numerical model should be revisited. Several plasticity models might be implemented, such as an elastoplastic and a revised multi-linear model, as well as an RO and NLKH models such as Chaboche, Armstrong-Fredericks, or Ohno-Wang variants.

A detailed comparison of the theoretical prediction capacity of these numerical models would elucidate the benefits and weaknesses of applying these models in the context of accumulated damage. The result would be practical guidance for the NLFEA of structures subjected to repeated dynamic loads. This investigation could effectively be

structured in a form similar to that undertaken by Ringsberg et al. (2018) with a direct focus on repeated impact behaviors.

Given that ratcheting is a cyclic plastic deformation behavior, an exciting application highly appropriate for sea-based structures would examine a constant mean stress and comparable stress amplitude applied in assorted loading paths to examine the effect on a large-scale piece of ship structure. For example, applying a constant primary stress such as that of hydrostatic buoyancy on a tank side, combined with dynamic cyclic stress such as simulation of repeated ice impacts along the hull. This analysis could be expanded to account for opposing stress components such as external hydrostatic loads from buoyancy and simultaneous internal loads such as hydrostatic loads from ballast or cargo while subjected to a repeating load. Furthermore, the landscape of these behaviors should be mapped to identify the boundaries or transitions between behaviors. In other words, is it possible to observe a confluence of stress components, each of which is by itself insufficient to lead to a particular plasticity behavior, but when applied concurrently permits a structure to transition from shakedown to ratcheting, or ratcheting to instantaneous plastic collapse?

An additional experimental vein within immediate reach of the already undertaken research concerns the relationship between specimen and/or component level ratcheting response among mixed media. There has been relatively little experimentation on the evolution of how stress/strain is partitioned among phases of a multiphase material (Paul, 2019). However, a novel and highly appropriate investigation given the state of naval construction outlined in section 1.1, would be an examination of how a previously

damaged, aged, or otherwise strain-affected material responds to repeated loading when the damaged structure has been repaired and now has both new and aged constituents. This would be analogous to a ship hull having experienced damage or receiving material inserts during a mid-life re-fit and then being subjected to repeated damage scenarios.

References

- Abdel-Karim, M. (2009). Modified kinematic hardening rules for simulations of ratchetting. *International Journal of Plasticity*, 25(8), 1560–1587.
<https://doi.org/10.1016/j.ijplas.2008.10.004>
- Alam, M. S., Daley, C., Colbourne, B., Hermanski, G., Gagnon, B., Bruneau, S., Clarke, G., & Quinton, B. (2012). Double pendulum dynamic impact test set-up for ice-grillage collision. *International Conference and Exhibition on Performance of Ships and Structures in Ice 2012, ICETECH 2012*.
- Alsos, H. S., & Amdahl, J. (2007). On the resistance of tanker bottom structures during stranding. *Marine Structures*. <https://doi.org/10.1016/j.marstruc.2007.06.001>
- ASM International. (2020). <http://www.asminternational.org>
- ASTM Standards. (2012). Standard test method for strain-controlled fatigue testing, E606/E606M - 12. *American Society for Testing and Materials*.
https://doi.org/10.1520/E0606_E0606M-12
- Barkey, M. (2018). *AEM 637: Theory of elasticity*.
https://www.youtube.com/watch?v=Zu_LGsixe_M&list=PLaDWa6xI4zefNlm7HrmpVen5g6A-4AgbB
- Bree, J. (1967). Elastic-plastic behaviour of thin tubes subjected to internal pressure and intermittent high-heat fluxes with application to fast-nuclear-reactor fuel elements. *Journal of Strain Analysis*. <https://doi.org/10.1243/03093247v023226>
- Chaboche, J. L. (1989). Constitutive equations for cyclic plasticity and cyclic

- viscoplasticity. *International Journal of Plasticity*, 5(3), 247–302.
[https://doi.org/10.1016/0749-6419\(89\)90015-6](https://doi.org/10.1016/0749-6419(89)90015-6)
- Chaboche, J. L. (2008). A review of some plasticity and viscoplasticity constitutive theories. *International Journal of Plasticity*, 24(10), 1642–1693.
<https://doi.org/10.1016/j.ijplas.2008.03.009>
- Chen, W. F., & Han, D. J. (1988). Plasticity for structural engineers. In *Plasticity for Structural Engineers*. J. Ross Publishing. <https://doi.org/10.1007/978-1-4612-3864-5>
- Chen, X., Jiao, R., & Kim, K. S. (2005). On the Ohno-Wang kinematic hardening rules for multiaxial ratcheting modeling of medium carbon steel. *International Journal of Plasticity*, 21(1), 161–184. <https://doi.org/10.1016/j.ijplas.2004.05.005>
- Cho, S. R., Truong, D. D., & Shin, H. K. (2014). Repeated lateral impacts on steel beams at room and sub-zero temperatures. *International Journal of Impact Engineering*, 72, 75–84. <https://doi.org/10.1016/j.ijimpeng.2014.05.010>
- Coffin, L. F. (2009). The deformation and fracture of a ductile metal under superimposed cyclic and monotonic strain. In *Achievement of High Fatigue Resistance in Metals and Alloys*. <https://doi.org/10.1520/stp26840s>
- Daley, C. G., & Hermanski, G. (2009). Ship frame research program-a experimental study of ship frames and grillages subjected to patch loads. *Washington, DC, USA: US Ship Structures Committee, SSC-457*.
- Dong, Q., Yang, P., & Xu, G. (2019). Low cycle fatigue and ratcheting failure behavior of AH32 steel under uniaxial cyclic loading. *International Journal of Naval*

- Architecture and Ocean Engineering*, 11(2), 671–678.
<https://doi.org/10.1016/j.ijnaoe.2018.09.003>
- Dowling, N. E. (2007). *Mechanical behavior of materials: Engineering methods for deformation, fracture and fatigue* (3rd ed.). Pearson.
<https://doi.org/10.5860/choice.46-6830>
- Drucker, D. C., & Prager, W. (1952). Soil mechanics and plastic analysis or limit design. *Quarterly of Applied Mathematics*. <https://doi.org/10.1090/qam/48291>
- Frederick, C. O., & Armstrong, P. J. (2007). A mathematical representation of the multiaxial Bauschinger effect. *Materials at High Temperatures*, 24(1), 1–26.
<https://doi.org/10.3184/096034007X207589>
- Fujita, Y., Nomoto, T., & Yuge, K. (1984). Behavior of deformation of structural members under compressive and tensile loads (1st report) on the buckling of a column subjected to repeated loading. *Japanese Society of Naval Architecture and Ocean Engineering*, 156, 346–354.
https://doi.org/10.2534/jjasnaoe1968.1985.158_385
- Fukumoto, Y., & Kusama, H. (1985a). Cyclic bending tests of plate elements under cyclic uniaxial loading. *Journal of Structural Engineering*, 111, 1051–1067.
[https://doi.org/10.1061/\(ASCE\)0733-9445\(1985\)111:5\(1051\)](https://doi.org/10.1061/(ASCE)0733-9445(1985)111:5(1051))
- Fukumoto, Y., & Kusama, H. (1985b). Cyclic bending tests of thin-walled box beams. *International Journal of Earthquake Engineering*, 2(1), 141–151.
https://www.jstage.jst.go.jp/article/jscej1984/1985/356/1985_356_141/_pdf
- Gagnon, R., Daley, C., & Colbourne, B. (2015). A large double-pendulum device to

- study load, pressure distribution and structure damage during ice impact tests in the lab. *Proceedings of the International Conference on Port and Ocean Engineering under Arctic Conditions, POAC*.
- Goldsmith, W., & Frasier, J. T. (1961). Impact: The theory and physical behavior of colliding solids. *Journal of Applied Mechanics*. <https://doi.org/10.1115/1.3641808>
- Hallquist, J. (2006). LS-DYNA® theory manual. In *Livermore Software Technology Corporation*.
- Hayward, W. (2004). Impact testing. *Advanced Materials and Processes*.
<https://doi.org/10.1533/9780857091024.203>
- Hertz, H. R. (1882). Über die Berührung fester elastischer Körper und über die Harte. *Verhandlung Des Vereins Zur Beforderung Des Gewerbefleißes, Berlin*, 92, 156–171.
- Hibbeler, R. C. (2001). Mechanics of materials. In *Pearson Prentice Hall* (8th ed.). Pearson Prentice Hall. <https://doi.org/10.1017/CBO9781107415324.004>
- Hu, Y., & Chen, B. (1995). A first-order second-moment approach to systems fatigue reliability of offshore structures. *Journal of Offshore Mechanics and Arctic Engineering*, 117(2), 105–112. <https://doi.org/10.1115/1.2827060>
- Hu, Y. R., & Chen, B. Z. (1996). *Fatigue reliability analysis of ship and offshore structures*. The People's Communication Press.
- Huang, Z. Q. (1999). Some problems in the study of ship strength. *Wuhan Ship Building*, 3, 1–5.
- Huang, Z. Q., Chen, Q. S., & Zhang, W. T. (2000). Pseudo-shakedown in the collision

- mechanics of ships. *International Journal of Impact Engineering*, 24(1), 19–31.
[https://doi.org/10.1016/S0734-743X\(99\)00041-X](https://doi.org/10.1016/S0734-743X(99)00041-X)
- Hübel, H. (1996). Basic conditions for material and structural ratcheting. *Nuclear Engineering and Design*. [https://doi.org/10.1016/0029-5493\(95\)01136-6](https://doi.org/10.1016/0029-5493(95)01136-6)
- Johnson, K. L. (1982). One Hundred Years of Hertz Contact. *Proceedings of the Institution of Mechanical Engineers*, 196(1), 3363–3378.
https://doi.org/10.1243/pime_proc_1982_196_039_02
- Johnson, K. L. (1989). *Contact mechanics*. Cambridge University Press.
<https://doi.org/10.1201/b17110-2>
- Jones, N. (2006). Some recent developments in the dynamic inelastic behaviour of structures. *Ships and Offshore Structures*, 1(1), 37–44.
<https://doi.org/10.1533/saos.2005.0007>
- Jones, Norman. (2014). Pseudo-shakedown phenomenon for the mass impact loading of plating. *International Journal of Impact Engineering*, 4(65), 33–39.
<https://doi.org/10.1016/j.ijimpeng.2013.10.009>
- Lee, Y. L., & Barkey, M. E. (2012). Fundamentals of cyclic plasticity theories. In *Metal Fatigue Analysis Handbook*. <https://doi.org/10.1016/B978-0-12-385204-5.00007-0>
- Liu, G. R., & Quek, S. S. (2013). The finite element method: A practical course. In *The Finite Element Method: A Practical Course: Second Edition* (2nd ed.). Butterworth-Heinemann. <https://doi.org/10.1016/C2012-0-00779-X>
- Lubliner, J., & Moran, B. (1992). Plasticity theory. *Journal of Applied Mechanics*.
<https://doi.org/10.1115/1.2899459>

- Mansour, A., Yang, J. M., & Thayamballi, A. (1990). Experimental investigation of ship hull ultimate strength. *Transactions - Society of Naval Architects and Marine Engineers*.
- Murray, J. M. (1965). *Notes on the longitudinal strength of tankers*.
- Paik, Jeom K. (2007). Practical techniques for finite element modeling to simulate structural crashworthiness in ship collisions and grounding (Part I: Theory). *Ships and Offshore Structures*, 2(1), 81–85. <https://doi.org/10.1533/saos.2006.0148>
- Paik, Jeom Kee. (2018). Ultimate limit state analysis and design of plated structures. In *Ultimate Limit State Analysis and Design of Plated Structures* (2nd ed.). Wiley. <https://doi.org/10.1002/9781119367758>
- Paik, Jeom Kee, Kim, K. J., Lee, J. H., Jung, B. G., & Kim, S. J. (2017). Test database of the mechanical properties of mild, high-tensile and stainless steel and aluminium alloy associated with cold temperatures and strain rates. *Ships and Offshore Structures*, 12(sup1), S230–S256. <https://doi.org/10.1080/17445302.2016.1262729>
- Paik, Jeom Kee, Thayamballi, A. K., Paik, J. K., & Thayamballi, A. K. (2009). Ultimate limit-state design. In *Ship-Shaped Offshore Installations*. <https://doi.org/10.1017/cbo9780511546082.008>
- Paik, Jeom Kee, Wang, G., Kim, B. J., & Thayamballi, A. K. (2003). Ultimate limit state design of ship hulls. *Transactions - Society of Naval Architects and Marine Engineers*.
- Park, D. K., Kim, D. K., Seo, J. K., Kim, B. J., Ha, Y. C., & Paik, J. K. (2015). Operability of non-ice class aged ships in the Arctic Ocean-part II: Accidental limit

- state approach. *Ocean Engineering*, 102(1), 206–215.
<https://doi.org/10.1016/j.oceaneng.2015.04.038>
- Paul, S. K. (2019). A critical review of experimental aspects in ratcheting fatigue: Microstructure to specimen to component. In *Journal of Materials Research and Technology*. <https://doi.org/10.1016/j.jmrt.2019.06.014>
- Paul, S. K., Stanford, N., Taylor, A., & Hilditch, T. (2015). The effect of low cycle fatigue, ratcheting and mean stress relaxation on stress-strain response and microstructural development in a dual phase steel. *International Journal of Fatigue*. <https://doi.org/10.1016/j.ijfatigue.2015.06.003>
- Plummer, C. J. G. (2014). Testing of polymeric materials. In *Comprehensive Materials Processing*. <https://doi.org/10.1016/B978-0-08-096532-1.00103-5>
- Polocoşer, T., Kasal, B., & Li, X. (2017). Design of experiment and pitfalls of low-velocity pendulum impact testing. *Journal of Dynamic Behavior of Materials*, 3, 436–460. <https://doi.org/10.1007/s40870-017-0123-5>
- Quinton, B. (2015). *Experimental and numerical investigation of moving loads on hull structures*. Memorial University of Newfoundland.
- Quinton, B. W. T. (2008). *Progressive damage to a ship's structure due to ice loading*. Memorial University of Newfoundland.
- Quinton, B. W. T., Daley, C. G., Gagnon, R. E., & Colbourne, D. B. (2017). Guidelines for the nonlinear finite element analysis of hull response to moving loads on ships and offshore structures. *Ships and Offshore Structures*.
<https://doi.org/10.1080/17445302.2016.1261391>

- Ramberg, W., & Osgood, W. R. (1943). Description of stress-strain curves by three parameters. *National Advisory Committee For Aeronautics*.
- Ringsberg, J. W., Amdahl, J., Chen, B. Q., Cho, S.-R., Ehlers, S., Hu, Z., Kubiczek, J. M., K rgesaar, M., Liu, B., Marinatos, J. N., Niklas, K., Parunov, J., Quinton, B. W. T., Rudan, S., Samuelides, M., Soares, C. G., Tabri, K., Villavicencio, R., Yamada, Y., ... Zhang, S. (2018). *MARSTRUCT benchmark study on nonlinear FE simulation of an experiment of an indenter impact with a ship side-shell structure*. <https://doi.org/10.1016/j.marstruc.2018.01.010>
- Shimada, Y., Kim, J., & Yamada, S. (2012). Effects of Strain-rate on the Hysteretic behavior of Structural Steels. *15th World Conference on Earthquake Engineering*. [https://doi.org/10.1061/\(ASCE\)ST.1943-541X.0002486](https://doi.org/10.1061/(ASCE)ST.1943-541X.0002486)
- Storheim, M., & Amdahl, J. (2017). On the sensitivity to work hardening and strain-rate effects in nonlinear FEM analysis of ship collisions. *Ships and Offshore Structures*, 12(1), 100–115. <https://doi.org/10.1080/17445302.2015.1115181>
- Sun, Y., & Zhang, J. B. (2015). Experimental study on shakedown behavior of DH36 steel used for semisubmersible. *Chuan Bo Li Xue/Journal of Ship Mechanics*, 19(7), 827–833. <https://doi.org/10.3969/j.issn.1007-7294.2015.07.008>
- The Canadian Press. (2015, November). End combat mission in Iraq and Syria, Trudeau orders defence minister. *Toronto Star*.
- Truong, D. D., Jung, H. J., Shin, H. K., & Cho, S. R. (2018). Response of low-temperature steel beams subjected to single and repeated lateral impacts. *International Journal of Naval Architecture and Ocean Engineering*, 10(6), 670–

682. <https://doi.org/10.1016/j.ijnaoe.2017.10.002>

Truong, D. D., Shin, H. K., & Cho, S. R. (2016). Dynamic response of steel grillages under repeated mass impacts at low temperature. *PRADS 2016 - Proceedings of the 13th International Symposium on PRactical Design of Ships and Other Floating Structures*.

Truong, D. D., Shin, H. K., & Cho, S. R. (2018). Repeated lateral impacts on steel grillage structures at room and sub-zero temperatures. *International Journal of Impact Engineering*, 113, 40–53. <https://doi.org/10.1016/j.ijimpeng.2017.11.007>

Wu, S. R., & Gu, L. (2012). Introduction to the explicit finite element method for nonlinear transient dynamics. In *Introduction to the Explicit Finite Element Method for Nonlinear Transient Dynamics*. Wiley. <https://doi.org/10.1002/9781118382011>

Xu, B. X., & Yue, Z. F. (2006). Study of the ratcheting by the indentation fatigue method with a flat cylindrical indenter: Part I. Experimental study. *Journal of Materials Research*, 21(7), 1793–1797. <https://doi.org/10.1557/jmr.2006.0222>

Xu, B. X., & Yue, Z. F. (2007). Study of ratcheting by the indentation fatigue method with a flat cylindrical indenter. Part II. Finite element simulation. *Journal of Materials Research*, 22(1), 186–192. <https://doi.org/10.1557/jmr.2007.0019>

Zhu, L. (1990). *Dynamic inelastic behavior of ship plates in collision*. Wuhan University of Technology.

Zhu, L., & Faulkner, D. (1996). Damage estimate for plating of ships and platforms under repeated impacts. *Marine Structures*, 9(7), 697–720. [https://doi.org/10.1016/0951-8339\(95\)00018-6](https://doi.org/10.1016/0951-8339(95)00018-6)

Zhu, L., Shi, S., & Jones, N. (2018). Dynamic response of stiffened plates under repeated impacts. *International Journal of Impact Engineering*.


<https://doi.org/10.1016/j.ijimpeng.2018.03.006>

Zhu, L., Shi, S., & Yu, T. X. (2015). A new ice load-response model for structural design of ice classed ships. *Proceedings of the International Offshore and Polar Engineering Conference*.

Appendix A – Material test report

Material test report from ArcelorMittal concerning structural steel plate used in laboratory experimentation.

8/31/2018 Test Reports - Test Report View


ArcelorMittal

Test Report Display [Return to Search Results](#)

[Printer Friendly Version](#)

ArcelorMittal Dofasco O.P.
P.O. Box 2460
Hamilton, Ontario
L8N 3J5

TEST REPORT
RAPPORT D'ESSAI

ATTENTION: [NAME]
Fax: [FAX]
Date: 07/12/2018

Page 1 of 1

Purchase Order/Bon de Commande
18_06505_43JULY
Bill of Lading/Connaissance
780482

Customer/Client
158882 PCS 388893881

Sales Order/Bon de Commande
Packing Slip/Bordereau de Charge

Vendor/Vendeur

Sold To/Vendu A
COLLEX INC.
350 RUE JEAN COUTU
VARENNES, QC.
J3X 0E1

Ship To/Expédier A
COLLEX - VARENNES
350 RUE JEAN COUTU, SUITE 000R #1
VARENNES, QC.
J3X 0E1
CORNER DE L'ENERGIE/JEAN COUTU

Spec/Norm et Spec
D07 G40.21 44K/50W FOR CONV TO PLATE (01/11)
STANDARD THICKNESS TOLERANCE
STITCH 0.04 MAX
MODIFIED SPECIFICATION
TEST REPORTS REQUIRED

Material Description/Description du Material
PLATE IN COIL FOR CONVERSION
STRUCTURAL STEEL
COILS
MILL EDGE PLAIN DRY
3010 MIN .3130 X 60 X COIL
WEIGHT: 43590 LBS
Test Methods/Methods d'Essai
ASTM A370, E1819, E815

HEAT	C	Mn	P	S	Si	Cu	Ni	Cr	Sn	Mo	Al	Ca	N	B	O
283297 .07	.65	.007	.002	.03	.02	.01	.04	.001	.005	.034	.037	.046	.002	.001	.0008 .0044 .0001

MECHANICAL PROPERTIES/PROPRIETES MECANQUES

TEST UNITS #51 GAUGE LENGTH 2 INCH

SERIAL NUMBER LIST # 01R YIELD STRENGTH ULTIMATE STRENGTH ELONG

NOMBRE DE SERIE PARCEAU RESISTANCE A LA RESISTANCE A LA ALLONG

T11063/00 4380668 T 61 74 29.3 (*)

(*) Method of elongation calculation: at fracture. / Methode de calcul de l'allongement: au point de fracture.

<https://ec.dofasco.ca/MaterialTestReports/TestReport.asp>

1/2

0200 98824